1974

Measurement of positive and negative pion total cross-sections on helium-3, beryllium-9, and carbon-12 over the 3/2, 3/2 resonance region

Charles Bailey Spence Jr.
College of William & Mary - Arts & Sciences

Measurement of $\pi^{\pm}$ Total Cross Sections on ^{3}He, ^{9}Be, and ^{12}C over the 3/2, 3/2 Resonance Region

---

A Dissertation

Presented to

The Faculty of the Department of Physics

The College of William and Mary in Virginia

In Partial Fulfillment

Of the Requirement for the Degree of

Doctor of Philosophy

---

by

Charles Bailey Spence, Jr.

July 1974

APPROVAL SHEET

This dissertation is submitted in partial fulfillment of

the requirements for the degree of

Doctor of Philosophy

Charles Bailey Spencer Jr.
Author

Approved, July 1974

John R. Kane
John R. Kane

Herbert O. Funsten
Herbert O. Funsten

Rolf G. Winter
Rolf G. Winter

Ying-Yeung Yam
Ying-Yeung Yam

Robert A. Orwoll
Robert A. Orwoll
Department of Chemistry

MEASUREMENT OF $\pi^{\pm}$ TOTAL CROSS SECTIONS ON ^{3}HE, ^{9}BE, AND ^{12}C OVER THE 3/2, 3/2 RESONANCE REGION

TABLE OF CONTENTS

ABSTRACT

A transmission experiment has been performed in which total cross sections for π^+ and π^- on ^{3}He, ^{9}Be and ^{12}C were obtained for several energies between 100 MeV and 250 MeV. The ^{3}He and ^{9}Be cross sections have been used in the evaluation of the Kim and Primakoff sum rule for nuclear beta decay. The evaluation of the sum rule is further extended to ^{7}Li cross sections obtained by Allardyce et al.

A second application of the ^{3}He data is made to determine a value for the effective π-nucleus coupling constant, r_{eff}. This is generated from a dispersion relation calculation, and is found to be r_{eff} (^{3}He) = 0.071 $\pm$ 0.012, which compares to a value of 0.081 $\pm$ 0.002 for the nucleon.

Finally the ^{3}He data is compared to the results of a Glauber-like total cross section calculation by Gurvitz.

I. INTRODUCTION

Nuclear total cross sections for positive and negative pions on ^{3}He and ^{9}Be were measured at several energies over the 3/2-3/2 resonance. The cross sections were measured by an attenuation technique using plastic scintillation counters. Pion-nuclear total cross sections for ^{12}C were also measured using the same experimental set-up, to provide an over-all calibration of the experimental procedure and data analysis routines. This was accomplished by comparing our carbon results with existing carbon cross sections.

The initial purpose of this work was to test a sum rule developed by Kim and Primakoff[1-5] for nuclear beta decay,

$$N_i \rightarrow N_f + e^- + \bar{\nu}_e .$$

In this theory weak interactions are treated as though the nuclei were "elementary particles" (E-P). Thus, the weak interactions of nuclei are treated without explicitly considering nuclei to be composed of nucleons. This E-P treatment has been invoked together with the Adler-Weisberger (A-W) procedure[6, 7] to obtain a sum rule relating the axial-vector coupling constant for nuclear beta decay, $F_A(0; N_i \rightarrow N_f)$ to an integral over pion energy of pion-final nucleus total cross sections, $I(-M_\pi^2; \pi^\pm N_f)$.[3, 5] The basis for this sum rule depends upon the validity of 1) the equal-time current commutation (ETC) relations for the hadron weak currents[8] and 2) the partially conserved axial-vector current (PCAC) hypothesis.[9, 10] Kim and Primakoff[3, 5] have

shown that the ratio $I(-M_\pi^2; \pi^+ N_f)/I(-M_\pi^2; \pi^+ p)$ is equal to the difference in the number of protons and neutrons in N_f, i.e. $[Z_f-(A_f-Z_f)]$, multiplied by a factor which becomes unity when virtual meson effects are neglected. It is the purpose of this work to provide an initial experimental test of this sum rule.

In addition to the sum rule in nuclear beta decay, an attempt is made to determine from our ^{3}He data an effective pion-nuclear coupling constant using forward dispersion relations in the manner of Ericson and Locher.[11] The evaluation of the coupling constant involves a similar integral over pion energy of the difference between the positive and negative cross sections.

A Glauber type multiple scattering cross section model for $\pi^\pm$ ^{3}He scattering as calculated by Gurvitz[12] will also be presented. A comparison between the experimental measurement of $\pi^\pm$ ^{3}He total cross sections and the multiple scattering model of Gurvitz's is made.

The theoretical background for the sum rule in nuclear beta decay, the effective pion nuclear coupling constant, and multiple scattering cross sections will be presented in Chapter II. The experimental procedure and description of the ^{3}He cryogenic target will be discussed in Chapter III, while the data analysis techniques will be discussed in Chapter IV. The results of the evaluation of the sum rule and effective coupling constants will be presented in Chapter V. The comparison of the multiple scattering model and our measured ^{3}He cross sections will also be given in Chapter V.

II. THEORY

A. Sum Rule in Nuclear Beta Decay

1. Elementary Particle Treatment

In the customary theory of beta decay of complex nuclei,

$$N_i \rightarrow N_f + e^- + \bar{\nu}_e \ ,$$

the weak-interaction Hamiltonian is written as a collection of terms for mutually isolated physical nucleons. Each term in the Hamiltonian refers to the hadron weak current for beta decay of a physical isolated nucleon within the nucleus. The initial and final nuclear states $|N_i\rangle$ and $|N_f\rangle$ depend on the position, spin, and isospin of each nucleon. The calculated matrix elements in this impulse approximation are, in general, sensitive to the wave function used. Kim and Primakoff[1] point out several serious discrepancies between the theoretical values using an impulse approximation and experimental ft values. They point out that these discrepancies appear too large to be attributed to a failure of an impulse approximation (i.e. due to neglecting pion-exchange effects), but rather probably arise from inadequate wave functions.

In the "elementary particles" treatment developed by Kim and Primakoff the difficulties of obtaining good wave functions are avoided by treating the nuclei N_i and N_f participating in the beta decay as "elementary particles". The weak-current matrix elements between the

initial and final nuclear states are expressed in terms of form factors characteristic of the nuclear transition $N_i \longrightarrow N_f$ as a whole rather than the usual sum of $n \longrightarrow p$ transitions. The hypothesis of the conserved vector hadron weak current (CVC) and the hypothesis of the partially conserved axial-vector hadron weak current (PCAC) can be applied to determine the effective vector and axial-vector coupling constants, $F_V(0; N_i \to N_f)$ and $F_A(0; N_i \to N_f)$. These coupling constants are characteristic of the $N_i \longrightarrow N_f$ beta decay transition and their numerical values reflect the complexity of the nuclear structure. For comparison with the basic equations of the "E-P" treatment to be presented, it is advantageous to first describe the transition matrix for the beta decay of the nucleon and the usual impulse approximation theory for nuclear beta decay.

a. Beta Decay of the Neutron

From the accepted current-current theory of the lepton-hadron strangeness-preserving weak interactions, the transition matrix element for neutron beta decay, $n \longrightarrow p + e^- + \bar{\nu}_e$ can be written as

$$\langle \bar{\nu}_e e^- p | J(0) | n \rangle = \frac{G}{\sqrt{2}} \left[\bar{u}_e \gamma_\alpha (1+\gamma_5) u_{\bar{\nu}_e} \right] \left[\langle p | j^V_\alpha(0) | n \rangle + \langle p | j^A_\alpha(0) | n \rangle \right], \quad (1)$$

where the matrix element of the vector and axial-vector currents are given by

$$\langle p | j^V_\alpha(0) | n \rangle = \left\{ \bar{u}_p \tau_+ \left[\gamma_\alpha F_V(q^2; n \to p) - \frac{\sigma_{\alpha\beta} q_\beta}{2M_p} F_M(q^2; n \to p) \right] u_n \right\}, \quad (2)$$

and

$$\langle p|j_\mu^+(0)|n\rangle = \left\{ \bar{u}_p \tau_+ \left[\gamma_\mu \gamma_5 F_A(q^2; n\to p) + \frac{i q_\mu \gamma_5 (M_p + M_n)}{m_\pi^2} F_P(q^2; n\to p) \right] u_n \right\}. \quad (3)$$

The F_i's (i = V, M, A, and P) are the neutron-proton weak form factors called polar-vector, weak-magnetism, axial-vector, and induced pseudoscalar respectively. The constant G is the weak coupling constant determined from μ decay

$$G = 1.01 \times 10^{-5} / M_p^2 .$$

The parameter q represents the four-vector momentum transfer

$$q = -(p_e + p_\nu) = (p_p - p_n).$$

The hypotheses of CVC and PCAC can now be used to relate the neutron-proton form factors (F_V, F_A, F_M, and F_p) to known physical quantities. The CVC hypothesis,[13] which identifies the vector hadron weak currents as components of a divergence-free isovector current, relates the polar-vector and weak magnetism form factors for n⟶p to the Dirac, $F_1(q^2)$ and Pauli, $F_2(q^2)$ electromagnetic form factors for n and p:

$$F_V(q^2; n\to p) = F_1^p(q^2) - F_1^n(q^2)$$

$$F_M(q^2; n\to p) = \frac{1}{2M_n}\left[\mu_p F_2^p(q^2) - \mu_n F_2^n(q^2) \right], \quad (4)$$

where μ_p and μ_n are the proton and neutron anomalous magnetic moments (in units of $e^2/2M_p$). Evaluation of these form factors at $q^2 = 0$ yields

$$F_V(0; n \to p) = Z_p - Z_n = 1$$
$$F_A(0; n \to p) = \mu_p - \mu_n = 3.70 \quad . \tag{5}$$

The PCAC hypothesis,[9, 10] can be written as the divergence of the strangeness-preserving axial-vector current

$$\partial_\lambda J^A_\lambda(0) = M_\pi^2 F_A(p_\pi^2 = -M_\pi^2;\ \pi \to \text{VAC.})\, \Phi_{\pi^-} \quad , \tag{6}$$

where

$$F_A(p_\pi^2 = -M_\pi^2;\ \pi \to \text{VAC.}) \equiv a_\pi \tag{7}$$

is the pion $\longrightarrow$ vacuum axial vector weak form factor and has the value[14]

$$a_\pi = 0.95 \pm 0.01$$

determined from the observed $\pi^+ \longrightarrow \mu^+ + \nu_\mu$ decay rate. The symbol Φ_{π^-} is the pion field which creates π^-, and is governed by the field equation

$$(\Box^2 - M_\pi^2)\Phi_\pi = -J_\pi \quad , \tag{8}$$

where J_π is the pion-source current. The matrix element of the divergence of the axial-vector current (eq. 6) between the nucleon states

can be written as (left hand side)

$$\langle p|\partial_\lambda j^A_\lambda(0)|n\rangle = -iq_\lambda\langle p|j^A_\lambda(0)|n\rangle = (M_p+M_n)\left[F_A(q^2;n\to p)+\frac{q^2}{M_\pi^2}F_P(q^2;n\to p)\right](\bar{u}_p\tau_+\gamma_5 u_n). \tag{9}$$

The right hand side of the matrix element can be written as (using eq. 8)

$$M_\pi^2 a_\pi\langle p|\phi_\pi|n\rangle = M_\pi^2 a_\pi\left\langle p\left|\frac{-J_\pi}{(\Box^2-M_\pi^2)}\right|n\right\rangle = M_\pi^2 a_\pi\left(\frac{1}{q^2+M_\pi^2}\right)f(q^2;[\pi np])(\bar{u}_p\tau_+\gamma_5 u_n), \tag{10}$$

where $f(q^2;[\pi np])$ is the proton-neutron vertex function. This expression reduces to

$$(M_p+M_n)\left[F_A(q^2;n\to p)+\frac{q^2}{M_\pi^2}F_P(q^2;n\to p)\right] = M_\pi^2 a_\pi\left(\frac{f(q^2;[\pi np])}{q^2+M_\pi^2}\right). \tag{11}$$

Two approximations result from this expression. They are

i) $q^2\to 0$ $\quad F_A(0;n\to p)\cong a_\pi\frac{f(0;[\pi np])}{M_n+M_p}$ Goldberger-Trieman (G-T) relation (12)

ii) $q^2+M_\pi^2\to 0$ $\quad F_P(q^2;n\to p)\cong\frac{a_\pi M_\pi^2}{(M_n+M_p)}\frac{f(-M_\pi^2;[\pi np])}{q^2+M_\pi^2}$. One-Pion Exchange (O.P.E.) dominance (13)

The parameter $f(-M_\pi^2;[\pi N p])$ is the pion-neutron-proton coupling constant (on-shell) and can be determined on the basis of a dispersion relation analysis of π - p elastic scattering to be[15]

$$\frac{f(-M_\pi^2;[\pi N p])}{4\pi} = 0.081 \pm 0.002 \ .$$

b. Beta Decay of the Nucleus: Impulse Approximation

Next we turn to the customary impulse approximation of nuclear beta decay, $N_i \longrightarrow N_f + e^- + \bar{\nu}_e$. Here the nucleus is treated as a collection of isolated nucleons. The transition matrix element for this process is written similar to eq. (1) as

$$\langle e^- \bar{\nu}_e N_f | J_\mu(0) | N_i \rangle = \frac{G}{\sqrt{2}} \left[\bar{u}_e \gamma_\mu (1+\gamma_5) u_{\bar{\nu}_e} \right] \left[\langle N_f | J_\mu^V(0) | N_i \rangle + \langle N_f | J_\mu^A(0) | N_i \rangle \right], \quad (14)$$

where the hadron weak current

$$J_\mu^V = \sum_{a=1}^{A} \tau_+^a \left[\gamma_\mu^a F_V(q^2; n \to p) - \frac{\sigma_{\alpha\beta} q_\beta}{2M_p} F_M(q^2; n \to p) \right] e^{iq\cdot R} \ , \quad (15)$$

and

$$J_\mu^A = \sum_{a=1}^{A} \tau_+^a \left[\gamma_\mu^a \gamma_5^a F_A(q^2; n \to p) + \frac{i q_\mu (M_p + M_n)}{M_\pi^2} \gamma_5^a F_P(q^2; n \to p) \right] e^{iq\cdot R} \ , \quad (16)$$

involves the nucleon operators only. The nuclear states $|N_i\rangle$ and $|N_f\rangle$ in the matrix element are described by the wave function Ψ_{N_i} and Ψ_{N_f} which are functions of $\{R^a\}$, $\{\sigma_3^a\}$ and $\{\tau_3^a\}$, the positions, spin, and isospin coordinates of the a^{th} nucleon. Pion-exchange effects are usually added to the impulse approximation by adjoining a

pion-exchange current[16] to the vector and axial-vector currents. In the calculation of transition matrix elements of nuclear beta decay, further approximations are usually made because of the energies involved in the beta decay process. The spatial part of the lepton wave function $e^{i\vec{q}\cdot\vec{r}(a)}$ can be set equal to unity in allowed transition because the deBroglie wave-length of the lepton wave function is large relative to the average nuclear dimension. The small value of the momentum transfer also allows the use of a nonrelativistic limit for the nucleon motion.

c. Beta Decay of the Nucleus: E-P Theory

The basic equations for the "elementary particle" treatment of nuclear beta decay for the particular transition

$$\left[N_i;\ (J^\pi;T)_i = \tfrac{1}{2}^{\pm};\tfrac{1}{2}\right] \rightarrow \left[N_f;\ (J^\pi;T)_f = \tfrac{1}{2}^{\pm};\tfrac{1}{2}\right] + e^- + \bar{\nu}_e$$

are analogous to those of nucleon beta-decay. Thus, the transition matrix can be written as

$$\langle \bar{\nu}_e e^- N_f | \mathcal{H}(0) | N_i \rangle = \frac{G_F}{\sqrt{2}} \left[\bar{u}_e \gamma_\nu (1+\gamma_5) u_{\nu_e}\right] \left[\langle N_f | j^V_\nu(0) | N_i \rangle + \langle N_f | j^A_\nu(0) | N_i \rangle\right] \quad (17)$$

The current matrix elements are now decomposed according to the structure of the nucleus and can be written as

$$\langle N_f | j^V_\nu(0) | N_i \rangle = \left\{ \bar{u}_{N_f} \tau_+ \left[\gamma_\alpha F_V(q^2; N_L \rightarrow N_f) - \frac{\sigma_{\alpha\beta} q^\beta}{2M_p} F_M(q^2; N_L \rightarrow N_f)\right] u_{N_i} \right\}, \quad (18)$$

and

$$\langle N_f | j_\alpha^A(0) | N_i \rangle = \left\{ \bar{u}_{N_f} \tau_+ \left[\gamma_\alpha \gamma_5 F_A(q^2; N_i \to N_f) + \frac{i q_\alpha (M_{N_i} + M_{N_f})}{M_\pi^2} \gamma_5 F_P(q^2; N_i \to N_f) \right] u_{N_i} \right\} \quad (19)$$

The F-functions (V, M, A, P) now represent the $N_i \longrightarrow N_f$ weak form factors, polar vector, weak magnetism, axial-vector, and induced-pseudoscalar. The functions U_{Ni} and U_{Nf} are the spinors describing the motion of the initial and final nucleus as a whole rather than the constituent nucleons.

On the basis of the CVC and PCAC hypotheses, the following equations can be patterned on the neutron beta decay:

i) analogous to eq. (4) and (5):

$$F_V(0; N_i \to N_f) = Z(N_f) - Z(N_i) = 1$$
$$F_M(0; N_i \to N_f) = [\mu(N_f) - Z(N_f)/A] - [\mu(N_i) - Z(N_i)/A] \quad (20)$$

where $\mu(N_i)$ and $\mu(N_f)$ are the initial and final nucleus magnetic moments, respectively.

ii) analogous to eq. (9) and (10):

$$\langle N_f | \partial_\lambda j_\lambda^A(0) | N_i \rangle = -i q_\alpha \langle N_f | j_\lambda^A(0) | N_i \rangle$$
$$= (M_{N_i} + M_{N_f}) \left[F_A(q^2; N_i \to N_f) + \frac{q^2}{M_\pi^2} F_M(q^2; N_i \to N_f) \right] (\bar{u}_{N_f} \tau_+ \gamma_5 u_{N_i}) \quad (21)$$

$$M_\pi^2 a_\pi \langle N_f | \phi_\pi | N_i \rangle = M_\pi^2 a_\pi \frac{f(q^2; [\pi N_i N_f])}{q^2 + M_\pi^2} (\bar{u}_{N_f} \tau_+ \gamma_5 u_{N_i})$$

where $F(q^2;[\pi N_i N_f])$ is the pion-initial-nucleus-final-nucleus vertex function. Equations (20) and (21) yield within the same approximations as for the nucleon case;

i) $q^2 \to 0$ $\quad F_A(0; N_i \to N_f) \simeq g_\pi \dfrac{F(0;[\pi N_i N_f])}{M_{N_i} + M_{N_f}}$ Goldberger-Trieman relation for nuclei

ii) $q^2 + M_\pi^2 \to 0$ $\quad F_P(q^2; N_i \to N_f) \simeq -\left(\dfrac{g_\pi M_\pi^2}{M_{N_i} + M_{N_f}}\right) \dfrac{F(-M_\pi^2;[\pi N_i N_f])}{q^2 + M_\pi^2}$ One-Pion Exchange dominance for nuclei

For the E-P treatment of the nuclear beta decay presented here, the quantum numbers on the initial and final nuclei are identical to the nucleon beta decay, i.e. $J^\pi; T = \frac{1}{2}^\pm; \frac{1}{2}$. For nuclear beta decay with quantum numbers different from those of the nucleon states, the vector and axial-vector matrix elements must be modified.[1] In general, more form factors are involved.

2. Adler-Weisberger Procedure

The sum rule developed by Kim and Primakoff is fundamentally dependent upon the PCAC hypothesis and the equal-time current commutation (ETC) relation introduced by Gell-Mann:[8]

$$Q_A^+(t)\, Q_A^-(t) - Q_A^-(t)\, Q_A^+(t) = 2 I_3(t) \,, \tag{22}$$

where

$$Q_A^\pm(t) \equiv -i \int \left[J_{A;4}^{(1)}(\vec{x},t) \pm i\, J_{A;4}^{(2)}(\vec{x},t) \right] d\vec{x} \,.$$

The symbols $J^{i}_{A;\mu}$ and I_3 are, respectively, the isovector, axial vector strangeness-preserving weak current and the third component of isospin.

The matrix element of the ETC relation taken between the final nuclear state $|N_f; M_f, \vec{P}_f, M_{J_f}\rangle$ in beta decay yields

$$\left(\frac{1}{2J_f+1}\right)\sum_{M_J=-J_f}^{+J_f}\langle N_f; M_f, \vec{P}_f, M_{J_f}\left|\left[Q_A^+(0), Q_A^-(0)\right]\right|N_i; M_i, \vec{P}_i, M_{J_i}\rangle = \langle|I_3(0)|\rangle , \quad (24)$$

which becomes

$$\left(\frac{1}{2J_f+1}\right)\sum_{M_J=-J_f}^{+J_f}\langle N_f\left|Q_A^+(0)Q_A^-(0)-Q_A^-(0)Q_A^+(0)\right|N_f\rangle = Z_f-(A-Z_f) .$$

Introducing a complete set of hadron states, $|N_s\rangle$ this equation can be written as

$$\left(\frac{1}{2J_f+1}\right)\sum_{M_J}\left[\sum_{N_s}\left|\langle N_f|Q_A^+(0)|N_s\rangle\right|^2-\sum_{N_s'}\left|\langle N_f|Q_A^-(0)|N_i\rangle\right|^2\right] = Z_f-(A-Z_f) . \quad (25)$$

Since the interaction, Q_A^+ (o) , which takes $N_s \longrightarrow N_f$ is charge raising (+) and Q_A^- (o) charge lowering (-), only certain states will contribute to the sum. Because of the selection rules on Q_A^- (o) and Q_A^+ (o) only the intermediate discrete and continuum states with

$$
\begin{aligned}
B(N_s) &= B(N_f) - A_f \\
Z(N_s) &= Z(N_f) \pm 1 \\
I(N_s) &= I(N_f) \mp 1 \;;\; I(N_f) \\
S(N_s) &= S(N_f)
\end{aligned}
\tag{26}
$$

and all $\pi^{\pm}$-N_f states will contribute to the sums over N_s and $N_{s'}$ (where B, Q, I, S are baryon, charge, isospin and strangeness quantum numbers). Therefore, the sums over N_s and $N_{s'}$ of the intermediate states, which contain both discrete and continuum states, can be written as the sum over states below and above the threshold for $N_s \longrightarrow N_f + \pi$ (see Appendix I).

For the sum over the states below the pion threshold, N_I is written by Kim and Primakoff[3, 5] using their "elementary particle" treatment for the nuclear states in the approximation $q^2 \longrightarrow 0$ as

$$
\sum_{N_s N_{s'}} = \sum_{N_I} \left[F_A(0; N_I \rightarrow N_f)^2 \right] (Z_f - Z_I)\, \Phi(J_I, J_f; P_{If}) \tag{27}
$$

where $\Phi(J_I, J_f; P_{If})$ represents a "kinematic" coefficient,[5] which is a function of the spin and parity of the nuclear states.

For complex nuclei with complicated energy level diagrams, many of the coupling constants $F_A(0; N_I \longrightarrow N_f)$ are not known, and therefore, the conventional method of isolating the contribution $F_A(0; N_i \longrightarrow N_f)$ is not useful. Kim and Primakoff, instead, evaluate

this sum over the states below the threshold by transition from the "elementary particle" treatment to an impulse approximation with a pion exchange correction.

Because of the poor overlap of the nuclear states, Ψ_f and Ψ_I for the mass $M_I > M_f + M_\pi$, the sum over N_I (states below threshold) is now extended to include all intermediate states. This allows the closure property of the complete set to be used. Therefore, Kim and Primakoff write

$$\begin{aligned}
&\sum_{N_I} \left[F_A(0; N_I \to N_f) \right]^2 (Z_f - Z_I)\, \Phi(J_I, J_f; P_{If}) \\
&= \tfrac{1}{3} \left| F_A(0; n \to p) \right|^2 \langle \Psi_f | (\sigma^+_{IA} + \sigma^+_{ex})(\sigma^-_{IA} + \sigma^-_{ex}) - (\sigma^-_{IA} + \sigma^-_{ex})(\sigma^+_{IA} + \sigma^+_{ex}) | \Psi_f \rangle , \\
&= \tfrac{1}{3} \left| F_A(0; n \to p) \right|^2 (1+\xi)^2 \langle \Psi_f | \sigma^+_{IA} \sigma^-_{IA} - \sigma^-_{IA} \sigma^+_{IA} | \Psi_f \rangle , \\
&= \left| F_A(0; n \to p) \right|^2 (1+\xi)^2 \langle \Psi_f | \sum_{k=1}^{A} (\tau^3)_k | \Psi_f \rangle , \\
&= \left| F_A(0; n \to p) \right|^2 (1+\xi)^2 \left[Z_f - (A_f - Z_f) \right]
\end{aligned} \tag{28}$$

where, for the purpose of estimating the 'meson exchange' terms, the operator $\sigma^\pm_{ex}$ has been replaced by $\xi \sigma^\pm_{IA}$ where ξ is assumed to vary monotonically and slowly with A_f.[5] The impulse approximation axial operator $\sigma^\pm_{IA}$ is written as

$$\sigma^\pm_{IA} = \sum_{a=1}^{A_f} \{ \tau^\pm \vec{\sigma} \}_a \quad .$$

The sum of the nuclear states above the pion threshold can be written as (see Appendix II)

$$\sum_{N_I N_f} = a_\pi^2 \, K(0; \pi N_i N_f)^2 \, I(-M_\pi^2; \pi N_f) \quad , \tag{29}$$

where

$$a_\pi \equiv F_A(-M_\pi^2; \pi \to VAc) \quad , \tag{30}$$

$$K(0; \pi N_i N_f) \equiv f(0; \pi N_i N_f) \Big/ f(-M_\pi^2; \pi N_i N_f) \quad , \tag{31}$$

and

$$I(-M_\pi^2; \pi N_f) = \frac{M_\pi^2}{\pi} \int \frac{dE_\pi}{E_\pi} \sqrt{E_\pi^2 - M_\pi^2} \left[\bar{\sigma}(-M_\pi^2; \pi N_f) - \bar{\sigma}^+(+M_\pi^2; \pi N_f) \right] . \tag{32}$$

The functions $\bar{\sigma}^{\pm}(-M_\pi^2; \pi N_f)$ are the $\pi^{\pm}$-N_f nuclear total cross sections for $\pi^{\pm} \cdot N_f$ at the total laboratory energy E_π . The constant $K(0; \pi N_i N_f)$ presents a measure of how fast the form factor $f(0; \pi N_i N_f)$ moves off-shell.

Combining the terms for the matrix element of the ETC relation, the sum rule for a final state beta decay nucleus, can be written as

$$\left| F_A(0; A \to p) \right|^2 (1+5)^2 \left[Z_f - (A - Z_f) \right] + a_\pi^2 K(0; \pi N_i N_f)^2 I(-M_\pi^2; \pi N_f) \approx Z_i - (A_i - Z_i) . \tag{33}$$

For the special case of $n \to p + e^- + \bar{\nu}_e$, this equation reduces to

$$\left| F_A(0; n \to p) \right|^2 + a_\pi^2 K(0; \pi n p)^2 I(-m_\pi^2; \pi p) \simeq 1 . \tag{34}$$

Combining these two equations yields the expression

$$I(-m_\pi^2; \pi N_f) \simeq \left[Z_f - (A_f - Z_f) \right] I(-m_\pi^2; \pi p) \left[\frac{K(0; \pi n p)}{K(0; \pi N_i N_f)} \right]^2 \left[\frac{1 - F_A(0; n \to p)^2 (1+\xi)^2}{1 - F_A(0; n \to p)^2} \right] . \tag{35}$$

If we make the approximations that the meson-exchange beta decay correction factor, ξ , is negligible relative to one, i.e. $\xi \ll 1$ and that

$$\left[\frac{K(0; \pi n p)}{K(0; \pi N_i N_f)} \right] \simeq 1 ,$$

then the above expression becomes simply

$$I(-m_\pi^2; \pi N_f) \simeq \left[Z_f - (A_f - Z_f) \right] I(-m_\pi^2; \pi p) . \tag{36}$$

Therefore, subject to these approximations, $I(-m_\pi^2; \pi N_f)$ and $I(-m_\pi^2; \pi p)$ would behave as an additive-type quantum number as a consequence of the ETC relation and the PCAC hypothesis.

B. Effective Pion-Nuclear Coupling Constant

Dispersion relations founded on the basic concepts of causality and analyticity,[17] have been of significant value in many fields of physics as a phenomenological framework for the interpretation of expermental scattering data. The use of forward dispersion relations to

determine pion coupling constants have been used extensively for the nucleon[18, 19, 20] and more recently this approach has been extended to complex nuclei.[21, 11] The basic framework for determining the effective pion-nuclear coupling constant for isospin I = 1/2, will be outlined here.

1. Pion-Nuclear Forward Dispersion Relation

Ericson and Locher[11] have shown that an effective pion-nuclear coupling strength can be obtained from pion scattering by nuclei, A, with I = 1/2. Defining an antisymmetric scattering amplitude,

$$f^{-}(\omega) = \frac{1}{2}\left[f_{\pi^+ A}(\omega) - f_{\pi^- A}(\omega)\right]^{*}, \tag{37}$$

they write the dispersion relation for the real part of the antisymmetric amplitude as

$$\mathrm{Re}\, f^{-}(\omega) = \sum_i \frac{2\omega\Omega_i}{\omega^2 - \omega_i^2} + \frac{2\omega}{\pi} P\int_{\omega_0}^{\infty} d\omega' \frac{\mathrm{Im} f^{-}(\omega')}{\omega'^2 - \omega^2}. \tag{38}$$

*This is defined for a target with excess neutrons. The pion charge can be reversed if the isospin component I_3 is positive.

where w is the pion total energy and w_i is the energy of the i^{th} pole. The real constant Λ_i is the dimensionless residue of the i^{th} pole and is proportional to the square of the coupling constant as the π-AA_i vertex. The pole terms correspond to the ground state and the excited states of the neighboring nuclei A_i with the same nucleon number, but differing in charge from A according to the pion charge. The lower limit of the integration ω_0 lies in the unphysical region ($\omega < M_\pi$) and has a value close to zero. This condition is due to physical pion absorption and is referred to as an unphysical cut below the threshold for scattering.

To obtain an effective coupling constant, Ericson and Locher evaluate equation (38) at $\omega = M_\pi$ while ignoring terms of order ω_i^2/M_π^2 to obtain

$$\mathrm{Re}f^-(M_\pi) = \frac{2}{M_\pi}\sum \Lambda_i + \frac{2M_\pi}{\pi} P\int_{\omega_0}^{\infty} \frac{\mathrm{Im}f^-(\omega')}{\omega'^2 - M_\pi^2} \quad . \qquad (39)$$

The effective coupling strength, Λ_{EFF} may be regarded as the sum of the residues of the poles, $\sum \Lambda_i$, and therefore eq. (39) can be rewritten as

$$\Lambda_{EFF} \simeq \frac{M_\pi}{2}\mathrm{Re}f^-(M_\pi) - \frac{M_\pi^2}{8\pi^2}\int_{\omega_0}^{\infty} d\omega' \frac{\mathrm{Im}f^-(\omega')}{\omega'^2 - M_\pi^2} \quad , \qquad (40)$$

where $k'^2 = \omega'^2 - M_\pi^2$.

Using the optical theorem $\mathrm{Im}f^-(\omega) = \frac{k\sigma^-(\omega)}{4\pi}$,

where $\sigma^- \equiv \frac{1}{2}\left[\sigma_{\pi^- A} - \sigma_{\pi^+ A}\right] \equiv \frac{1}{2}\Delta\sigma^-$,

eq. (40) can be rewritten as

$$\Lambda_{EFF} = \frac{M_\pi}{2} Re f^-(M_\pi) - \frac{M_\pi^2}{8\pi^2} P \int_{\omega_0}^{\infty} d\omega' \frac{\Delta\sigma^-}{k'} \quad . \tag{41}$$

2. Unphysical Region

The unphysical cuts for pion-nucleus (π-A) scattering adds a special feature, relative to the nucleon, in that Im $\bar{f}(w)$ does not equal zero below the physical threshold, $\omega = M_\pi$. The imaginary part, Im $\bar{f}(w)$, in the unphysical region for $\omega_0 < \omega < M_\pi$ cannot be directly measured. The extrapolation of Im $\bar{f}(w)$ from the elastic threshold $\omega = M_\pi$ to $\omega_0 \approx 0$ have been made phenomenologically[11] by a continuation of the complex amplitude above threshold by a replacement of $k \to i|k|$. This leads to the form

$$Im f^-(\omega) \simeq \alpha^- + \beta^- |k| + \gamma^- |k|^2 + \delta^- |k|^3 + \epsilon |k|^4 \tag{42}$$

where the coefficients are given by the complex s, p, and d wave scattering lengths;

$$\alpha^- = Im\, a_0^- \qquad \beta^- \simeq -2\, Re\, a_0^-\, Im\, a_0^- \qquad \gamma^- \simeq -3\, Im\, a_1^-$$
$$\delta^- \simeq 0 \qquad \epsilon^- \simeq 5\, Im\, a_2^-$$

These low energy pion nuclear scattering parameters, (scattering lengths, volumes, etc.) can be obtained from measurement of the electromagnetic levels of π^- -mesic atoms. The Bohr levels are perturbed by the π^--nuclear strong interaction which results in a shift, ΔE, of the energy level as well as broadening, Γ, of the energy level due to strong absorption of the pion. Writing the complex

energy shifts as $\Delta E = Re\Delta E + i\left(\frac{\Gamma}{2}\right)$, Trueman[22] expresses the s- and p wave scattering lengths a_0 and a_1 as (linear terms only)

$$a_0 \simeq \frac{1}{4Z\alpha}\,\frac{\Delta E_{1s}}{E_{1s}}\,M_\pi^{-1}$$
$$a_1 \simeq \frac{2}{3(Z\alpha)^3}\,\frac{\Delta E_{2p}}{E_{2p}}\,M_\pi^{-3} \qquad (43)$$

where Z is the nuclear charge and α the fine structure constant.

Returning to equation (41), we see that the effective pion-nucleus coupling constant can be obtained from the value of $Re\bar{f}(M_\pi)$ and from the integral of the $\pi^{\pm}$-nuclear cross sections with an extension being made into the unphysical region. The scattering amplitude $Re\bar{f}(M_\pi)$ is deducible from π-nucleus scattering lengths. The evaluation of $Re\bar{f}(M_\pi)$, as well as the contribution of the integral will be given in section C of Chapter V for the ^{3}He effective coupling constant.

C. Strong Interaction Cross Sections $\pi^{\pm}$ ^{3}He

Nuclear total cross section for $\pi^{\pm}$ ^{3}He have been calculated by Gurvitz[12] by means of a Feynman diagram technique. The scattering of the meson by the nucleus was regarded in terms of single scattering by each nucleon and all possible rescattering by the remaining nucleons. The contribution to the scattering amplitude from the corresponding diagram for single, double, and triple scattering were considered to yield an expression for the total cross section,

$$\sigma_{TOT} = 3\sigma_{\pi N}^{TOT} - \frac{3\pi^2}{16\pi}\left(\sigma_{\pi N}^{TOT}\right)^2 + \frac{\pi^4}{192\pi^2}\left(\sigma_{\pi N}^{TOT}\right)^2\left(3\alpha^2-1\right).$$

The symbol α is the ratio of the real to imaginary parts of the scat-

tering amplitude in the forward direction and

$$\lambda^2 = 0.87 \times 10^{24}\ cm^{-2}\ .$$

The spin and isospin of the nucleons were not taken into account in the calculations.

The results for the contribution of the rescattering calculated by Gurvitz coincides with the contribution calculated using the Glauber model.[23] Similar calculations were carried out by Gribov[24] for π -D scattering using the diagram technique. The results obtained using the Feynman diagram technique are valid up to an incident pion momentum at which a pion can be produced in the virtual state ($\sim 2 GeV/c$).

III. EXPERIMENTAL PROCEDURE

The experiment was performed at the 600 MeV synchrocyclotron of the N.A.S.A. Space Radiation Effects Laboratory (SREL) in Newport News, Virginia. Data were accumulated in three separate cyclotron runs, each approximately a week in duration. Two conventional beam-lines were used with the pions produced by the cyclotron being brought to a one inch diameter definition at the target. Data for the first two runs were taken in the Neutron-Meson area (NMA4), which will be referred to as Beam I, and yielded cross sections. For the last run, data were accumulated in the Proton-Target area (PTA), which will be designated as Beam II. These measurements produced π^+ cross sections and an additional π^- measurement.

The experimental technique and apparatus used to determine the cross sections will be described in this section. A description of the ^{3}He cryostat, as well as a discussion of the beam characteristics, will also be given in this section.

A. Counter Description

The total cross sections were measured by a transmission technique. The experimental counter arrangement used to measure cross sections for the ^{3}He is shown in Fig. (1). All counters except the Cerenkov counter (not shown) were plastic scintillation counters (Pilot B) with each scintillator viewed through a Lucite light pipe by Amperex 56AVP photomultipliers. The description of the Cerenkov counter and

time of flight counters will be given in section C.

The incident beam from the cyclotron was collimated to a 1 1/2" diameter by a lead shielding wall, 3' width, by 2' height, by 2/3' depth. This wall was erected four feet downstream of the last quadrapole magnet. Three circular counters, S_1, S_2, and S_3 defined the incident beam size. Counters S_1 and S_2 were positioned directly behind the lead shielding and were 2" and 1" in diameter respectively. Counter S_3, which was positioned directly in front of the Mylar entrance window of the cryostat, was 1" in diameter. Counters S_2 and S_3 were separated by 40". Both S_1 and S_2 had a thickness of 1/8", while S_3 was 1/32" thick. The thickness of S_3 was determined by a compromise between keeping the efficiency of the counter greater than 95% and reducing the number of particles scattered out of the incident beam by the counter itself.

For the first data run in Beam I, these three circular counters defined the incident pion signal, $S_1S_2S_3$. This counter coincidence was designated the beam monitor trigger (MT). For the second data run in Beam I and the data run in Beam II, two anticounters, A_1 and A_2, were used in conjunction with the circular counters to define the incident beam according to $\bar{A}_1S_1S_2\bar{A}_2S_3$. The primary purpose of these counters was to define a more parallel beam and to aid in eliminating accidental coincidences. Counter A_1, which had a 8" x 8" x 1/4" active plastic region with a 1 1/8" diameter hole at its center, was positioned between the lead shielding wall and S_1. The purpose of A_1 was to eliminate particles from the incident beam which had lip-scattered from the inside of the lead collimator and traversed a diagonal path between

the edges of S_2 and S_3. The geometry of such a path would have required the particle to pass through A_1, thereby rejecting such an event as a valid master trigger event. With counter A_1 in anticoincidence, the loss of beam was less than 4%. The anticounter A_2, which had a 6" x 6" x 1/4" active region with a 1 1/4" diameter hole at its center, was positioned upstream of S_3. The initial purpose of A_2 was to eliminate accidental coincidence in the transmission counters caused by two particles traversing the beam axis within the resolving time τ of the incident beam coincidence. Suppose a particle triggering S_1, S_2, and S_3 were followed within time τ by a second particle which missed S_3. This second particle could register a false count in one of the transmission counters. The number of such events vetoed by the anticounter A_2 measured less than .5% of the incident beam.

The use of an anticounter positioned before the target to eliminate this second pion problem can, however, give rise to a systematic error in the measured cross section. Incident pions identified by the monitor trigger may interact in the target sending a particle into the backward hemisphere. If the anticounter detects this particle, then a valid event will be rejected causing a systematically lower value in the cross section. The magnitude of the effect depends on the solid angle subtended by the anticounter at the target. The correction made for this effect was typically less than 1% and will be described in section I of Chapter IV.

For the solid targets, the monitor trigger was slightly modified from that described for the ^{3}He-target. This was done because it was not always feasible, from a consideration of available running

time, to remove the helium-3 cryostat from the beam line, once in position. With the cryostat in position, a fourth circular counter, S_4, of 1" diameter and 1/8" thickness, was placed directly behind the exit window of the cryostat. The solid targets were mounted immediately downstream of this counter. The monitor trigger, defining the incident flux upon the target, then became $S_1S_2\bar{A}_1S_3\bar{A}_3S_4$. This beam-defining coincidence was used both in Beam I and Beam II. Some data were, however, accumulated in Beam I without the helium-3 cryostat in position. Under this condition, only the three circular counters, S_1, S_2, and S_3, were used.

A small probe counter 1/4" x 1/4" plastic scintillant measured the beam profile at the target position. The counter was mounted upon a remotely operated traversing platform which allowed a beam profile to be taken in a horizontal and vertical direction. The measured profiles were Gaussian in shape with a typical full-width at half-maximum (FWHM) of 0.75 inches. These profiles were used to assure proper beam alignment and were also used in evaluating the Coulomb scattering correction for a definite beam size (see section C, Chapter IV).

The transmission counters consisted of a 3 1/2" diameter disc-shaped scintillator and four annular shaped counters with increasing radii. The disc-shaped scintillant was 1/16" thick and the annular counters were 1/2" thick. Each of the transmission counters was viewed from one side only by a wedge-shaped Lucite light pipe. The disc-shaped counter was designated as counter T and the annular counters labeled R_{1-4}, in order of increasing radius. The dimensions of the inner and outer radii of the ring counters, as well as all other

scintillators used, are listed in Table I.

The transmission counters were mounted concentrically about the beam axis, as shown in Fig. (1), with R_4 closest to the scattering targets. The counters were spaced approximately 1 mm apart. The system of ring counters was mounted in the Beam II work on a remotely controlled rail system which allowed the ring counters to traverse the beam axis, changing the interval of scattering angles accepted by each counter. Counter T measured the attenuation of the incident beam, while counters R_{1-4} mapped out a differential total cross section of the scattering particles. The differential cross section was used to make the correction for the forward nuclear scattering into the counter T. The procedure for extracting the forward nuclear scattering into counter T using the annular counters, as well as the analysis of the transmission measurements to yield total cross sections will be given in section B of Chapter IV.

The radii of the rings and the thickness of counter T were chosen to minimize the effect of back scattering of the transmitted particle into an adjacent ring. In an early data run, under Beam I conditions, two adjacent counters overlapped by 1/4", and counter T had a thickness of 1/2". The removal of counter T from the beam line produced a 10% effect in the number of particles registered in counters R_{1-4}. This was attributed to the fact that counter T, which normally received 90-95% of the transmitted beam, was back scattering pions into counters R_{1-4}. Counter T was then redesigned as a 1/16" thick scintillant of the same diameter, and the inner radii of the counters R_{1-4} were increased to the nonoverlapping values listed in

Table I. With these new dimensions, the removal of counter T produced less than a 2% change in the number of particles registering in the adjacent counters. A similar effect was obtained for the removal of any of the other counters R_{1-4}. Since the effect is the same for both target full and target empty data runs to first order, no explicit correction was made.

Because of the annular shape of ring counters R_{1-4}, the light collection efficiency for a particle traversing the scintillant closest to the photomultiplier was much higher than for a particle traversing the opposite surface of the ring. This effect produced "jittering" in the timing curve because of the difference in pulse height from the phototube. To minimize this effect, a triangular shaped diffuse reflecting surface was formed on the Lucite light pipe of each counter by painting with Tygon paint (SB-361-white). The area of the triangle painted was proportional to the area of the ring counter. This reflecting surface gave a pulse height response uniform to within 30% over the entire annular surface.

The possibility of false counts from Cerenkov light produced in the light guides of the transmission counters was also investigated. A light guide identical to the one used for counter T, but without any scintillator, was mounted in place of counter T. The number of counts registered under standard beam conditions proved to be less than .1% of the normal T flux.

B. Logic Circuitry

A block diagram of the logic circuitry used in the experiment

is shown in Fig. (2). All the units were modular in form and were commercially manufactured (Chronetics, Inc., E. G. & G., Inc., or Ortec, Inc.). The blocks labeled D are standard 100 MHz discriminators and those labeled C are coincidence units. For all the counters used in the experiment high voltage plateau and delay curves were taken at frequent intervals. The outputs of all discriminators were typically set at 6 nsec FWHM except for the anticounters, which were set at 15 nsec FWHM. The incident beam coincidence unit, the monitor trigger, was gated off for 1 millisecond during the prompt spike of the beam's macrostructure. For this 1 msec. period the instantaneous rates were high and could overload the electronic circuitry, increasing the probability of accidental coincidence. Only the stretched portion of the spill was accepted for Beam I and II.

Signals from the transmission counters were sent to a strobe coincidence unit (E. G. & G. C126/N), which was strobed by the monitor trigger, MT. The widths of the resolution curves for each coincidence (MT(T) and MT(R_i)), were adjusted to be the same within 0.5 nsec. This insured that the ring counters had the same probability for accidental events. The five outputs of the strobe unit were then sent to five individual fanout units. This permitted us, with the aid of equal length signal cables, to form every conceivable two-fold coincidence among the transmission counters, i.e., MT(R_i)(T) and MT(R_i)(R_j) ($i \neq j$). These coincidences were scaled, as were the five outputs of the strobe unit. The complex coincidences, MT(R_i)T and MT(R_i)(R_j) ($i \neq j$) were examined merely for probable systematic errors and were not used in the cross section analysis. Each of the coincidences that made up the

monitor trigger was also scaled.

As a measurement of accidental coincidences between the beam monitor, MT, and the various transmission counters, the monitor trigger input to the strobe unit was delayed 54 nsec. By delaying in this way, we obtained measurements of the probability of accidental coincidences. The corrections made for accidental coincidences will be described in section G of Chapter IV.

C. Measurement of Beam Composition

The composition of the beam incident upon the scattering target was measured in the early runs by time of flight (TOF) method, and in the later runs by a total absorption Cerenkov counter technique. The time of flight system which was used under Beam I conditions consisted of two scintillation counters which were separated by approximately 4 meters. The scintillators were coupled directly to their phototubes without light pipes and gave a timing resolution of 300 psec.

Fig. (3-A) shows a schematic of the time of flight system. The output of the downstream counter T_2 formed the start signal to a time to amplitude converter (TAC) and the upstream counter T_1 was used as the stop signal. The TAC was gated by the monitor trigger pulse, MT, and the output of the TAC was fed to a 512 channel Kicksort analyzer. The resulting spectrum consisted of π and μ peaks with the relative areas giving the beam composition. The electrons present in the incident beam were few in number and typically could not be resolved. Figures (10-A, B) show typical spectra accumulated using the time of flight system. Discussion of the computer fitting procedure used in extracting

the composition from the TOF spectra will be given in section E of Chapter IV.

During the earlier run under Beam I conditions, the downstream counter of the time of flight system was positioned behind the assembly of ring counters. This allowed the beam composition to be measured during the target out runs, but it was necessary to correct the spectra for the pions which decayed between the target and the time of flight counter T_2. During the later runs in Beam I, the downstream counter was positioned at the target position on a traversing platform, which allowed the counter to be put in and out of the beam. The beam composition was then measured between target in and target out runs for a given incident energy.

For the data runs in Beam II, the beam composition was determined from a total absorption Cerenkov chamber. Fig. (3-B) shows a schematic of the Cerenkov chamber with the associated logic circuitry. The chamber used followed the design of ref. (24). The detector was 16 inches long, 4 1/2" in diameter, and was lined with an aluminum reflective liner. A fluorocarbon radiator (3M Co., Type FC 75) was used for all incident energies.

The chamber was viewed through a 1/4" thick Lucite window at the downstream end by a five inch diameter RCA bi-alkali phototube with a gallium-phosphide first dynode, (No. C70135B). The output of the Cerenkov detector served as input to a linear gate (E. G. & G. No. LG102/N), which was gated by the monitor trigger, MT. The output of the linear gate was then sent to a 512 channel pulse height analyzer.

For the beam composition measurement, the front face of the

Cerenkov chamber was positioned at the target location to determine for the various energies the incident beam composition at the target. During data accumulation, the chamber was positioned 12 inches downstream of the transmission counters and was used as a monitor of the complete system. The Cerenkov spectra accumulated under this condition were analyzed and checked for consistancy from one run to the next.

Figures (11-ABC) show typical Cerenkov spectra measured at the target position for Beam II. Fig. (12) shows the spectrum of the π^- beam used in Beam II. Discussion of the fitting procedure for extracting beam composition will also be given in section E of Chapter IV.

D. Beam Characteristics

1. Beam I

For the data runs taken in the Neutron-Meson area(NMA4) negative pions were produced by the 600 MeV protons incident upon an internal carbon production target. Figure (4) shows a layout of the meson beam area at SREL. A pair of 9" diameter quadrapole magnets inside the cyclotron vault focused the beam for passage throggh the main shielding wall of the cyclotron. A bending magnet, outside the shielding wall and at a 45° angle to the beam port, deflected the pion beam onto the experimental apparatus. The incident pion beam was determined by range curve measurement to have an energy of 240 MeV with an energy resolution of $\pm$ 4%.

Beam "stretching" was accomplished by a "harp" production target shaped from 100 thin carbon fibers. With the duty factor defined as

the ratio of the duration of the beam burst to the separation between beam bursts, the duty factor was 20%.

Because the particles exiting from a given beam port have been momentum analyzed by the main magnetic field of the cyclotron, it was necessary to degrade the energy of the incident beam to produce a variable range of energies. Both copper and polyethylene were used as energy degrading materials. The degrader was normally in front of the lead collimator downstream of the bender. For some of the data accumulated under parasitic conditions, it was necessary to place the degrader between the cyclotron shielding wall and the bending magnet because of physical limitations. In those cases, the degrader was dropped into place from a catwalk above the experimental area. The energies developed in this manner ranged from 130 MeV to 240 MeV and are listed in Table II, as are the other beam characteristics.

An attempt was made to extract a π^+ beam under the same experimental layout by reversing the polarity of the main magnetic field of the cyclotron. The pions were produced in the backward direction (relative to the proton beam) from a stainless steel production target. Because of the high proton background and low pion flux encountered, no π^+ data were taken under Beam I conditions.

2. Beam II

To produce a π^+ beam, a second beam line involving the extracted proton beam was used. Pions were produced from a polyethylene target placed in the magnet hall in the path of the proton beam. The stochastic cee was used to stretch the proton beam resulting in a duty factor of 40%.

Figure (5) shows a layout of the Risk[25] pion channel used to transport the pions into the experimental counting area (PTA). The pions were momentum analyzed by two bending magnets, M_1 and M_2, and were focused onto the scattering target by four quadrapole singlets; Q_1, Q_2, Q_3, and Q_4. A field lens (quadrapole doublet Q_1' and Q_2'), placed between M_1 and Q_3, permitted spatial recombination of all momenta at the second bending magnet. A 1 1/2" width beam slit was positioned between Q_1' and Q_2' and gave an energy resolution of $\pm$ 2%. A 1/8" aluminum plate located at the entrance of Q_1' was used to remove protons.

The energy of the incident pion beam used was determined by the current setting of the bending magnets and the thickness of the CH_2 production target. Energies ranging from 170 MeV to 295 MeV were produced by selecting CH_2 production target thicknesses between 18" and 3 1/2". Measurements were taken at 270 MeV and 290 MeV but the cross sections were not computed because it appeared that protons were contaminating the monitor trigger signal. Energies below 170 MeV were produced by degrading the incident beam with CH_2 absorber just before the lead collimating wall. Table III consists of a listing of the energies covered in Beam II and their related parameters.

Beam II was also used to provide a beam of negative pions. By reversing the polarity of the magnets, with the exception of Q_1' and Q_2', in the pion channel, a beam of π^- was provided with the same resolution and energy as the π^+ beam. One energy measurement of π^- on ^3He was taken under this condition.

E. Targets

1. Solid Targets

The carbon and beryllium targets were mounted on a remotely operated traversing platform which provided motion perpendicular to the beam axis. These targets were separated by a 5" blank space which permitted the following data runs to be taken quickly for a given energy and transmission counter-to-target distance: 1) Carbon, 2) Blank, and 3) Beryllium.

The dimensions and weights of the carbon and beryllium targets were measured to determine their densities and number of atoms/cm^2. The targets were machined before use in order to "true" the edges of the target. The carbon target had a mean thickness of .660 $\pm$ .005 inches and had a density of 1.33 $\pm$ .01 g/cm^3. The beryllium target used was .720 $\pm$ .005 inches thick and had a density of 1.85 $\pm$ .01 g/cm^3. A second beryllium target with a .410 $\pm$ .005 inch mean thickness was also used. Measurements for two beryllium thicknesses permitted us to determine the effect of target size upon the cross sections (see section I). The physical dimensions and number of atoms/cm^2 are given in Table IV.

2. Liquid ^{3}He Cryostat

One hundred liters (STP) of ^{3}He gas (on loan from Carnegie-Mellon University) were liquified and used as a scattering target. A schematic of the cryogenic system, together with the auxiliary equipment developed for liquifying and maintaining ^{3}He in a liquid state, is shown in Fig. (6). A description of each of these components and their functions will be given in the following sections.

a. Cryostat Design

A 200 cm^3 ^3He target was suspended beneath a liquid helium 4 reservoir and placed in thermal contact with the reservoir. The ^3He target was housed in a Sulfrian Corporation cryostat, which had a capacity of approximately 30 liters. The reservoir was filled with liquid helium 4 from a 100 liter liquid ^4He storage dewar. The storage dewar was coupled to the cryostat by a rigid transfer line which incorporated a valve to regulate the ^4He flow. The lower section of the cryostat containing the ^3He target is shown in Fig. (7).

The ^4He reservoir of the cryostat was composed of an upper and lower section which were connedted by means of an indium "0"-ring seal, as described by Buckle etaal.[26] This made it possible to remove the lower section to which the ^3He target was connected for easy access to the target. A liquid nitrogen jacket enclosed the upper section of the ^4He reservoir making contact only at the neck of the dewar. All inner walls of the cryostat were gold plated in order to reduce the radiative heating. The lower section of the ^4He reservoir was wrapped in tin foil for the same reason.

Surrounding the ^3He target was a tin foil radiation shield, 50 mils thick (helium tail), which was in thermal contact with the ^4He reservoir. This tail provided a heat shield at approximately the same temperature as the liquid ^3He target and thereby reduced the turbulence of the liquid due to boiling. Surrounding the helium tail was a 1/16" thick copper radiation shield (nitrogen tail), placed in thermal contact with a liquid nitrogen jacket. All surfaces of the helium and nitrogen tails were cleaned and polished to create surfaces of low emissivity.

Quarter-mil aluminized Mylar was used as entrance and exit windows of the nitrogen and helium tails instead of copper and tin, respectively. This was to minimize the non-target material in the beam while still protecting against incident radiation.

A stainless steel vacuum jacket completed the enclosure of the cryostat. Fifteen mil Mylar was used for the entrance and exit windows of the vacuum jacket, which were 4.0" in diameter. The Mylar was captured by a double O-ring (neoprene) seal between a flange on the vacuum jacket and a retaining ring which could be clamped to the vacuum flange. A 2" diameter vacuum line coupled the cryostat to a portable pumping station. The pumping station consisted of a 4" diameter oil diffusion pump (CVC type-PMC 720-A) with a liquid nitrogen cooled baffle. A helium leak detector, which could be calibrated to sense ^{3}He or ^{4}He leaks, was coupled to the system to indicate vacuum leaks that might develop during the course of the experiment.

b. ^{3}He Target

The ^{3}He target was a cylindrical stainless steel vessel, $2.375 \pm .005$" in diameter by $2.575 \pm .009$ inches in length with the symmetry axis of the cylinder aligned with the beam axis. A ferrule was welded at each end of the cylinder into which an end window could be sealed. The end windows for the target initially consisted of 3 mil stainless steel, which was Heliarc welded between two stainless steel rings. The outside ring had an inside diameter of 2.325" and outside diameter of 2.625", and a thickness of 1/32". The inside ring was of the same dimensions and had a cylindrical lip which mated to the ferrule of the target cylinder. Once in position, this window was sealed to the

target with low temperature indium solder. This arrangement for the ^{3}He target window was used for data obtained in Beam I.

Because of the difficulty encountered in making the indium seals at the windows leak proof at liquid helium temperatures, and also to improve the ratio of ^{3}He scattering material to total scattering material (^{3}He + empty target), the window and seal were redesigned. The 3 mil stainless steel was replaced by a sandwich of two 5 mil Mylar sheets bonded with an adhesive of Epon-Versamid. A 50%-50% mixture, by weight, of Epon No. 828 (produced by the Shell Chemical Co.) and Versaid No. 125 (produced by the General Mills, Inc.) was used. The resulting 10 mil Mylar was then bonded with Epon-Versamid to a copper ring and ring flange of the same design as described for the stainless steel window. The joint was mechanically clamped by 16 screws which brought together the two copper rings and the Mylar. All surfaces that were bonded were first cleaned with acetone and lightly sandblasted with a fine powder. Copper was used instead of the stainless steel because of the tendency of the Mylar-stainless joint to crack when cooled to cryogenic temperatures.[27] The Mylar-copper window was then bonded to the target cylinder with Epon-Versamid adhesive, replacing the indium solder joint. Successive layers of adhesive were applied, allowing the previous layer to partially cure before the next layer was added. This adhesive proved to give a mechanically strong, vacuum tight joint.

This arrangement of the 10 mil Mylar window for the scattering target was used under Beam II conditions. The 10 mil Mylar windows gave a ratio of ^{3}He to ^{3}He plus empty target material (g/cm^2) of 72%. This

represented an improvement of 5% over the stainless windows.

c. Gas Handling System

Fig. (8) shows a schematic of gas handling system used in the liquification and recovery of the ^{3}He gas. The ^{3}He gas was normally stored in a 20 liter stainless steel cylinder at a pressure of approximately 65 psig. The storage cylinder was connected to the gas panel through a metering valve which was used to regulate the flow rate and to decrease the high cylinder pressure to a level more easily handled by the rest of the gas system. The gas panel consisted of a double piston pump which was used to transfer the ^{3}He to and from the scattering target; a liquid nitrogen cold trap, used to purify the ^{3}He gas before liquification; a Wallace and Tiernan 0-2 atmosphere absolute pressure manometer (Model FA145), used to measure the vapor pressure of the liquid ^{3}He; and a Vacsorb pump.

The double piston pump used to transfer the ^{3}He gas was similar to that described by Erdman.[28] The upper piston chamber was used as a pumping station. Teflon O-rings were used as seals for the pistons. Two "pop-it" valves connected to the top chamber determined the direction of gas flow through the pump. The second piston chamber was used to drive the upper piston. Dry nitrogen gas at pressures up to 85 psig. was used to operate the lower piston. A four-way solenoid valve regulated the nitrogen gas pressure to provide up and down cycling of the pump. A variable speed control unit regulated the period of the pumping cycle.

The liquid nitrogen cold trap consisted of six stainless steel cylinders containing activated charcoal and connected in series. The

cylinders were placed in a liquid nitrogen bath to remove those impurities in the ^{3}He gas which condense above 77° K. The charcoal trap was initially baked in a heating jacket and evacuated before each use.

All elements of the gas panel were connected with 1/4" copper tubing. A Marsh vacuum-pressure gauge was placed in the line between the metering valve and the 20 liter storage tank to register the pressure in the tank. Other Marsh vacuum-pressure gauges were placed at various critical points in the gas panel lines.

The gas panel was coupled to the cryogenic scattering target by two long 1/8" o.d. by 0.020" wall stainless steel tubes which served as the input and return lines for the ^{3}He gas. The stainless tubes passed through the liquid ^{4}He reservoir and penetrated the bottom isolation plate of the reservoir into the ^{3}He target chamber. The two tubes were carefully hard soldered to the 1/4" thick stainless steel plate which separated the target region from the ^{4}He reservoir section to prevent mixing of the isotopes. The input line for the ^{3}He was wound in a helical coil to enhance heat exchange with the ^{4}He. The gas panel, stainless steel tubing, and ^{3}He target thus formed a closed system which was initially pumped out by the Vacsorb pump.

d. Target Preparation

The process used in preparing the ^{3}He target was the following:

After the cryostat and gas panel proved to be leak-proof at room temperature, the liquid nitrogen jacket of the cryostat was filled. Cold nitrogen gas was also allowed to flow into the ^{4}He reservoir section until a temperature of $\sim$ 125°K was attained. Cold helium 4 gas from the 100 liter liquid helium storage dewar was then allowed to flow

into the reservoir, continuing the cooling process. The initial cool-down to liquid nitrogen temperature proceeded slowly, taking 2-3 hours, in order to prevent vacuum leaks due to differential contractions in the target. The leak detector coupled to the system monitored the system for the development of leaks during and after cool-down. The temperature during cool-down was monitored by two copper-constantan thermocouples, one fastened to the ^{4}He tail and the other to the nitrogen tail. Once the liquid helium began to collect in the reservoir, it could be filled rapidly. The reservoir was normally filled to a 20-25 liter capacity. The valve of the ^{4}He transfer line was then closed, isolating the storage dewar from the cryostat. The entire cooling process ($T = 300^\circ$ K to $T = 4.2^\circ$ K) took 4-5 hours.

With the helium 4 reservoir full, a small amount of ^{3}He gas was allowed to flow into the scattering target to test for ^{3}He leaks at liquid ^{4}He temperature. The 0-2 atmosphere Wallace and Tiernan absolute pressure manometer which was coupled to the closed ^{3}He system monitored the amount of ^{3}He gas transferred to the target cell. This pressure gauge was also used to monitor the target vapor pressure after liquification of the ^{3}He in order that its density[29] could be determined.

Since the normal boiling point of liquid ^{4}He occurs at 4.2° K and helium 3 liquifies at 3.2° K under normal pressure, it was necessary to lower the temperature of the ^{4}He reservoir. This involved pumping on the ^{4}He reservoir, in order to lower its vapor pressure and consequently its temperature. With the top of the reservoir vacuum sealed, the system was pumped by a 425 l/min. Welch mechanical pump through a 1" dia-

meter pumping port. Interrupting the pumping system, between the reservoir and the mechanical pump, was a cartesian manostat[30] which was used to regulate and maintain a set ^{4}He vapor pressure. A 0-1 atmosphere Wallace and Tierman absolute pressure gauge (Model FA145) was used in order to monitor the reservoir vapor pressure. The vapor pressure was usually maintained at 110 mm of Hg, which corresponded to a temperature of 2.7° K. This somewhat arbitrary temperature was chosen to restrict the temperature between 2.2° K, and λ point for ^{4}He and 3.2° K, normal condensation point for ^{3}He. Since the ^{3}He target was in thermal contact with the reservoir, the measurement of the ^{4}He vapor pressure gave a second method for determining the temperature and density of ^{3}He.

A by-pass valve with 1" orifice was installed in parallel with the manostat. This was utilized in the initial pump-down of the reservoir and in any refilling of the reservoir after the temperature had been set at 2.7° K. After the vapor pressure had been lowered to about 125 mm of Hg, following an initial pumping, the by-pass ball-valve was closed and the Cartesian manostat with its 1/8" pumping orifice then regulated the vapor pressure.

With the ^{4}He reservoir cooled to the desired temperature, the main valve of the 20 liter ^{3}He storage tank was opened. The ^{3}He gas was first passed through the liquid nitrogen cold trap to aid in removing residual impurities. As the gas passed through the 1/8" diameter input line in the reservoir, the ^{3}He liquified and collected in the target volume. The piston pump was used to empty the 20 liter storage tank and to pump the ^{3}He gas toward the cryostat. The entire process

of liquification took 2-3 hours.

Unlike the solid target arrangement where a target-out run followed a target-in run, a series of ^{3}He target-full runs were taken over a set of energies before the corresponding target-out runs were taken. In order to have the target-full and target-empty data runs at a given energy follow each other as closely as possible in time, the process used was normally the following: A series of target-empty runs were taken over an energy range with the cryostat at 2.7° K. The target was then filled and the data runs taken over the same energy range. With the target still full, a second set of runs was taken over a different set of energies, after which the target was emptied and the corresponding empty runs were taken.

Since the ^{3}He target was normally emptied while the cryostat was at 2.7° K, a small heating resistor attached to the target was utilized to hasten evacuation. A 10 ohm, 1/4 watt carbon resistor was fastened to the underside of the target by cryogenic epoxy (Helex Epoxy Products, type R313). A current of 500-700 ma passing through the resistor provided sufficient heat input to slowly vaporize the ^{3}He. The piston pump was used in junction with the carbon resistor to pump the ^{3}He gas back into the 20 liter storage tank. The process of emptying the target took 3-4 hours.

F. Energy Measurement

The energy and energy spread of the pion beams were obtained from analysis of differential range curves in copper. The range telescope, shown in Fig. (9-A), was positioned in front of the lead colli-

mator. The telescope consisted of two plastic scintillators, W_1 and W_2, placed in front of a variable copper absorber, with two plastic scintillators, W_3 and W_4, placed behind the absorber. Counters W_1 and W_2 were 2" x 2" x 1/4". W_3 had dimensions of 5" x 5" x 1/8", while W_4, which was used as an anticounter, was 10" x 10" x 1/4".

The variable beam degrader consisted of 12" x 12" copper plates whose total thickness could be changed in steps of 1/16". This "copper-dropper" worked on an inclined plane principle with each plate riding downhill on a set of ball bearings. The individual plates were held out of the beam line by a spring-loaded lever arm which could be remotely released to allow the plate to slide into place. The plates were held vertical between two grooved platforms to assure proper alignment. A television camera monitored the position of each plate upon release.

A thin absorber, usually a 1/16" iron plate, was inserted between counters W_3 and W_4. This absorber was used to increase the stopping target thickness and had the effect of increasing the signal-to-noise ratio.

A plot of the coincidence $W_{123\bar{4}}$ (W_4 in anticoincidence) per W_{12} versus the g/cm^2 of the copper absorber yielded a peak at the mean range of the incident pion beam. Figures (9-B) and (9-C) show they typical range curves taken in Beam I and Beam II. The centroid of the peak was determined by a least square curve fitting computer code (see section E, Chapter IV). The distribution was fitted to a Gaussian with a sloping background.

The mean range determined in this manner represented the mean depth of penetration along a straight line. The actual path length of the pion in the absorber is always larger than the measured range because of multiple Coulomb scattering. Corrections to the mean range for multiple scattering were made following the procedure of Lewis[31] and Janni[32] and were of the order of a percent or less.

The mean range was also corrected for the energy loss in counters W_1, W_2, and W_3. The amount of copper thickness equivalent to the energy loss in the counters was added to the mean range. This equivalent amount of copper, Δx , was obtained by solving the equation

$$\int \frac{dE}{dx} \Delta x \Big|_{Cu.} = \int \frac{dE}{dx} dx \Big|_{SCINT.} = \text{ENERGY LOSS} .$$

An equivalent amount of copper for one-half the thickness of the 1/16" iron plate was also added. One-half of the thickness was used because the maximum counting rate corresponds to the pions with the most probable energy stopping in the middle of the iron plate. The energy of the incident beam was then determined by the use of a range-energy table.[33]

When the flux of muons in the incident beam was high enough to yield good statistics, the mean range of the muons was also determined. Since the pions and muons in the incident beam have the same momentum, this provided a second method of obtaining the incident energy.

For two of the Beam II magnet current settings, a separate experimental group[34] had determined the incident energy of the pion channel by the wire orbit technique. The two different methods yielded agreement to within 1%, with the range curve method producing the lower

value of the two.

The energy resolution of the incident beam was determined from the full-width at half-maximum (FWHM) of the fitted Gaussian. The width of the measured differential range curve can be expressed as the result of the combined effects of straggling, incident energy spread, and the stopping target resolution. The amount of straggling for each incident beam energy was computed[35] and subtracted from the FWHM. For the percentage of range straggling ϵ, defined by

$$\epsilon = 100 \times \left(\frac{\langle \Delta R^2 \rangle^{\frac{1}{2}}}{R} \right) ,$$

where $\langle \Delta R^2 \rangle^{\frac{1}{2}}$ represents the mean square deviation of the range to straggling, the values of ϵ ranged from 1.2% to 1.5% over the energies covered in this experiment. As an estimate of the effect of the stopping target resolution, one-half of the thickness of the absorber positioned between W_3 and W_4 is subtracted for the measured FWHM. The energy spread of the incident beam measured in this manner was $\pm$ 4.0% at 240 MeV and increased to 5.2% at 145 MeV for Beam I. For Beam II, the energy spread was consistant at $\pm$ 2.0% for all energies except 198 MeV where the value rose to $\pm$ 3.0%.

All energies quoted for the cross sections are energies at the center of the target. Those values were obtained from the incident energies with corrections applied for the energy loss caused by the material in the beam, namely counters S_1, S_2, and S_3, and 1/2 the target thickness.

IV. DATA ANALYSIS

A. General Considerations

The transmission technique of measuring nuclear total cross sections involves a comparison of particle flux transmitted by a target to a reading of the particle flux transmitted with the target removed. This method automatically corrects for instrumental effects and attenuation by any target holder or other material in the beam.

Under idealistic conditions (narrow parallel or pencil beam, no Coulomb scattering, and a transmission counter of such a reduced size that any pions interacting with the scattering material would be absorbed or scattered beyond the acceptance of the transmission counter) the number of pions, T, detected in the transmission counter for a beam of I_o particles incident on the target can be written as

$$T_F = (I_o)_F e^{-\sigma_T N x} e^{-B} . \qquad (1)$$

The parameter x represents the thickness of the target, σ_T the total nuclear cross section for the scattering material, and N the number of scattering nuclei per unit volume. The factor e^{-B} accounts for background scattering due to any target container material, attenuation in the air and beam-defining counters upstream of the target. Subscripts designate readings taken either for a full target (F) or an empty target (E). Under the same beam conditions the corresponding measurement [illegible] can be written as

with the target material removed can be written as

$$T_E = (I_o)_E e^{-B} . \tag{2}$$

Dividing eq. (1) by eq. (2) yields

$$\frac{(T/I_o)_F}{(T/I_o)_E} = e^{-\sigma_T N x} ,$$

or

$$\sigma_T = \frac{1}{Nx} \ln\left[\left(\frac{T}{I_o}\right)_E \Big/ \left(\frac{I}{I_o}\right)_F\right] . \tag{3}$$

The standard deviation for the computed cross section due to counting statistics alone is given by

$$\Delta\sigma_T = \frac{1}{Nx}\left[\frac{1}{T_F} - \frac{1}{(I_o)_F} + \frac{1}{T_E} - \frac{1}{(I_o)_E}\right]^{\frac{1}{2}} . \tag{4}$$

B. Experimental Method

For a transmission counter of finite size, subtending a half angle θ measured from the target center, the measured cross section, σ_M using eq. (3) is less than the true total cross section by an amount due to forward scattering events, both elastic and inelastic, which scatter into the transmission counter. If the number of particles registering in the transmission counter is written as the sum of transmitted particles, T, (no nuclear interaction) and forward nuclear scattered particles, FNS, then eq. (3) can be written as (setting $I_{oF} = I_{oE}$)

$$\sigma_M = \frac{1}{Nx} \ln\left[T_E/(T+FNS)_F\right] . \tag{5}$$

This equation can be rewritten in terms of the true cross section as

$$\sigma_M = \frac{1}{Nx} \ln\left(\frac{T_E}{T_F}\right) - \frac{1}{Nx} \ln\left(1+\frac{FNS}{T}\right),$$

or (6)

$$\sigma_M = \sigma_T - \frac{1}{Nx} \ln\left(1+\frac{FNS}{T}\right) .$$

The second term in eq. (6) represents the correction for the forward nuclear scattering into the transmission counter. The number of particles nuclear scattered into the transmission counter is given by

$$FNS = I_o Nx \int_o^\theta \left(\frac{d\sigma}{d\Omega}\right)_{ch} d\Omega , \tag{7}$$

where $\left(\frac{d\sigma}{d\Omega}\right)_{ch}$ represents the value of the nuclear differential cross section.

For the counter arrangement used in the present experiment as shown in Fig. 1, counter T measured the attenuation of the incident beam and yielded the value σ_M . The annular counters, R_{1-4}, measured the angular distribution of both elastic and inelastic events. The angular distribution was plotted versus the mean angle of acceptance of the annular counters and extrapolated to $\theta = 0$ degrees. In this way, it was possible to numerically calculate the forward nuclear scattering contribution of eq. (7).

The differential cross section measured by the annular counter R_i can be expressed as

$$\left(\frac{d\sigma}{d\Omega}\right)_i = \frac{1}{Nx}\left[\frac{\left(\frac{R_i}{I_o}\right)_F - \left(\frac{R_i}{I_o}\right)_E}{\Delta\Omega_i}\right] , \tag{8}$$

where $(R_i)_F$ and $(R_i)_E$ are the i^{th} counter events corrected to yield only the nuclear events for the target full and empty, respectively. The symbol $\Delta\Omega_i$ represents the average solid angle subtended by the annular counter R_i. These solid angle values were calculated by a Monte Carlo method which averaged over (1) the finite beam size using the measured incident beam distribution (see section A, Chapter III), and (2) the t target thickness. The statistical error for the differential cross section is given in the manner of eq. (9) by adding in quadrature the probabilities that a particle has been transmitted into the annular counter under target full and target empty conditions:

$$\Delta\left(\frac{d\sigma}{d\Omega}\right)_i = \frac{1}{Nx}\left[\left[\frac{I_o\left(1-\frac{R_i}{I_o}\right)\left(\frac{R_i}{I_o}\right)}{I_o}\right]^2 + \left[\frac{I_o\left(1-\frac{R_i}{I_o}\right)\frac{R_i}{I_o}}{I_o}\right]^2\right]^{\frac{1}{2}} \Big/ \Delta\Omega_i . \tag{9}$$

For the beams used in this work, the beam intensity I_o incident upon the scattering material can be written as

$$I_o(\pi,\mu,e) = f_\pi I_o + f_\mu I_o + f_e I_o . \tag{10}$$

The f's represent the fractional number of pions, muons, and electrons (positrons) present in the incident beam and satisfy the expression

$$f_\pi + f_\mu + f_e = 1 \quad . \tag{11}$$

For the pion interaction with the scattering material, the "reaction" cross section can be written as

$$\begin{aligned} |F_N + F_c|^2 &= |F_N|^2 + |F_c|^2 + |F_N F_c| \quad , \\ &= \frac{d\sigma_N}{d\Omega} + \frac{d\sigma_c}{d\Omega} + \frac{d\sigma_{Nc}}{d\Omega} \quad . \end{aligned} \tag{12}$$

where F_N is the nuclear scattering amplitude and F_C the Coulomb scattering amplitude. The number of particles, $T_E(\pi,\mu)$, registering in the finite size transmission counter, T, for the target empty condition can be written as (neglecting the electron term for economy of space since the muons and electrons interact in the same manner)

$$T_E(\pi,\mu) = f_\pi I_o(\pi,\mu) e^{-\bar{\sigma}_c \bar{N} \bar{x}} e^{-\bar{\sigma}_N \bar{N} \bar{x}} e^{-\bar{\sigma}_{Nc} \bar{N} \bar{x}} + f_\mu I_o(\pi,\mu) e^{-\bar{\sigma}_c \bar{N} \bar{x}} , \tag{13}$$

where

$$\bar{\sigma}_c = \int_{\theta_1}^{\pi} \frac{d\sigma}{d\Omega} d\Omega =$$

Probability for particle to Coulomb scatter between θ and π from the target holder,

$$\bar{\sigma}_N = \int_{\theta_1}^{\pi} \frac{d\sigma_N}{d\Omega} d\Omega \,,$$

Probability for nuclear scattering (elastic and inelastic) from target holder,

(14)

$$\bar{\sigma}_{NC} = \int_{\theta_1}^{\pi} \frac{d\sigma_{NC}}{d\Omega} d\Omega \,,$$

Probability for pion to scatter into the angular range $\theta \longrightarrow \pi$ due to the nuclear-Coulomb interference,

$\bar{N}$ = number of nuclei per volume of the target holder material,

and

$\bar{x}$ = thickness of the target holder material in the beam.

(Inelastic events such as particle knock-out registering in counter T are included in the argument π of T_E of eq. (13)). With the target material in position, the number of particles registering in the transmission counter can be expressed as

$$T_F(\pi,\mu) = f_\pi I_o e^{-\sigma_c N x} e^{-\bar{\sigma}_N \bar{N} x} e^{-\sigma_{NC} N x} e^{-\bar{\sigma}_c \bar{N} \bar{x}} e^{-\bar{\sigma}_N \bar{N} \bar{x}} e^{-\bar{\sigma}_{NC} \bar{N} \bar{x}} + f_\mu I_o e^{-\sigma_c N x} e^{-\bar{\sigma}_c \bar{N} \bar{x}} , \quad (15)$$

where σ_C , σ_N , σ_{NC} , N and x represent the corresponding target-full quantities.

From the experimentally determined values, T_E (π , μ) and T_F (π , μ) the number of pions registering in the transmission counter can be obtained by computing

$$T_F(\pi) = T_F(\pi,\mu) - f_\mu I_o e^{-\bar{\sigma}_C \bar{N} \bar{x}} e^{-\sigma_o N x} , \tag{16}$$

and

$$T_E(\pi) = T_E(\pi,\mu) - f_\mu I_o e^{-\bar{\sigma}_C \bar{N} \bar{x}} .$$

Taking the ratio of these last two expression yields

$$\frac{T_E(\pi)}{T_F(\pi)} = \frac{f_\pi I_o e^{-\bar{\sigma}_C \bar{N} \bar{x}} e^{-\bar{\sigma}_N \bar{N} \bar{x}} e^{-\bar{\sigma}_{NC} \bar{N} \bar{x}}}{f_\pi I_o e^{-\bar{\sigma}_C \bar{N} \bar{x}} e^{-\bar{\sigma}_N \bar{N} \bar{x}} e^{-\bar{\sigma}_{NC} \bar{N} \bar{x}} e^{-\sigma_C N x} e^{-\sigma_N N x} e^{-\sigma_{NC} N x}} , \tag{17}$$

$$= e^{+\sigma_C N x} e^{+\sigma_N N x} e^{+\sigma_{NC} N x} .$$

Finally, taking the natural log of both sides of this equation and re-writing, the result becomes

$$\sigma_N = \frac{1}{Nx} \ln \left(\frac{T_E(\pi)}{T_F(\pi)} \right) - \sigma_C - \sigma_{NC} . \tag{18}$$

Invoking the definitions for the σ's in eq. (14), eq. (18) can be written as

$$\int_0^\pi \frac{d\sigma_N}{d\Omega} d\Omega = \frac{1}{Nx} \ln \left(\frac{T_E(\pi)}{T_F(\pi)} \right) - \int_{\theta_1}^\pi \frac{d\sigma_C}{d\Omega} d\Omega - \int_{\theta_1}^\pi \frac{d\sigma_{NC}}{d\Omega} d\Omega . \tag{19}$$

The nuclear total cross section σ_T can be constructed from eq. (19) by adding to both sides the correction for the forward nuclear scattering as illustrated in eq. (6).

$$\sigma_T = \int_{\theta_1}^{\pi} \frac{d\sigma_M}{d\Omega} d\Omega = \frac{1}{Nx} \ln \frac{T_E(\pi)}{T_T(\pi)} - \int_{\theta_1}^{\pi} \frac{d\sigma_C}{d\Omega} d\Omega - \int_{\theta_1}^{\pi} \frac{d\sigma_{NC}}{d\Omega} d\Omega + \frac{1}{Nx} \ln \left(1 + \frac{FNS}{T_T(\pi) - FNS}\right)$$

$$\sigma_T = \int_{0}^{\pi} \frac{d\sigma_M}{d\Omega} d\Omega = \frac{1}{Nx} \ln \frac{T_E(\pi)}{T_T(\pi)} - \int_{\theta_1}^{\pi} \frac{d\sigma_C}{d\Omega} d\Omega - \int_{\theta_1}^{\pi} \frac{d\sigma_{NC}}{d\Omega} d\Omega + \frac{1}{Nx} \ln \left(1 + \frac{FNS}{T_T(\pi) - FNS}\right) .$$

$$(\text{MEAS } \sigma) \quad (\text{Coul}) \quad (\text{Coul-Nucl}) \quad (\text{For. Nucl.}) \tag{20}$$

For a given beam energy, data were accumulated for up to three different positions of the transmission counters, with each position yielding a cross section measurement. The differential cross sections measured by the annular counters for each position of the transmission counters, after all corrections had been made to yield only nuclear events, were combined to form a single plot from which the extrapolation to zero degrees could be made. The transmission counters were positioned to cover the range of momentum transfer from 50 to 150 MeV/c. The lower limit was required in order to keep the Coulomb-nuclear interference correction of the order of 1%, while the upper limit kept the correction for the forward nuclear scattering of the order of a 10% correction. The values obtained for the total cross section at each position of the transmission counters were then averaged to give the final cross section at that energy.

C. Coulomb Correction

Corrections for the Coulomb scattering of the beam constituents were applied as required by eqs. (16) and (20). For incident

pions of momentum p, the Coulomb scattering amplitude is given by

$$\left|f_c(t)\right| = -2\pi \frac{p}{|t|} F_\pi(t) F_{tgt}(t) \,, \tag{21}$$

where $|t|$ is the four momentum transfer

$$t = -2p(1-\cos\Theta) \,, \tag{22}$$

and η is the effective Coulomb coupling constant,

$$\eta = \frac{3Z\alpha^2}{\beta} \,. \tag{23}$$

The parameters z and Z are the charge of the pion and the charge of the target nucleus, respectively; β is the velocity of the incident pion and α is the fine-structure constant.

The functions $F_\pi(t)$ and $F_{tgt}(t)$ are the pion and target nucleus charge form factors, respectively. The pion form factor can be expressed as[36]

$$F_\pi(t) = \exp\left[-\frac{1}{6}\Omega_\pi^2 |t|\right] \tag{24}$$

with Ω_π = 0.8 fm, while the form factor for carbon and beryllium can be written as[37]

$$F_{tgt}(t) = \left(1 - \frac{\alpha |t|^2 a_0^2}{2(2+3\alpha)}\right) e^{-\frac{|t|^2 a_0^2}{4}} \,, \tag{25}$$

where $\alpha = 1/3\ (Z-2)$ and $a_o = 1.63$ fm for carbon and 1.56 fm for beryllium. For helium-3 the form factor was expressed by[38]

$$F_{s_{He}}(t) = e^{-\frac{|t|a_o^2}{4}}, \tag{26}$$

where $a_o = 1.31$ fm.

For the muons and electrons in the incident beam, the Coulomb scattering amplitude can be written as in eq. (21) with the form factor of the incident particle set equal to one and corrected to take into account the spin of the projectile. The spin of the incident particle can be taken into account by multiplying eq. (21) by the factor $(1 - \beta^2 \sin^2\frac{\theta}{2})$ where β is the velocity of the incident muon or electron. Further corrections to the scattering amplitude for the spin of the nucleus of the recoil of the nucleus have been neglected since these corrections are proportional to the inverse of the mass of the nucleus. The neglect of these terms yielded uncertainties in the Coulomb correction of the order of 0.1% or less.

To evaluate the effect of the finite beam size incident upon the scattering target, the measured beam profile (see section A, Chapter III) was folded into the integral for the Coulomb correction. The resulting integral for the Coulomb scattering was evaluated numerically by Simpson's rule. The Coulomb correction was typically a 1-3% correction, depending on the incident energy and the position of the transmission counters. The Coulomb corrections for the π^+ and π^- cross section measurements are listed for carbon in Tables VI and VII; for beryllium-9 in Tables VIII and IX; and for helium-3 in Tables X and XI.

In addition to correcting for particles which missed counter T because of Coulomb scattering, corrections were also made for the number of particles registering in the individual annular counters, R_{1-4}, because of Coulomb scattering. This was required by eq. (7) since the extrapolation to zero of the differential cross section, which provides the forward nuclear scattering correction, must involve nuclear events only. The calculation was performed in the same manner as above with the limits of integration carried over the angular acceptance of each counter.

The correction to the cross section for multiple Coulomb scattering was also investigated. Following the technique of Sternheimer,[39] the number of particles missing the transmission counter T, because of multiple Coulomb scattering could be calculated. The correction to the carbon cross section at the two lowest energies was calculated and found to be completely negligible. Therefore, no correction to any of the cross section measurements was made.

D. Coulomb-Nuclear Interference

The data were corrected for the interference between the elastic nuclear amplitude and the Coulomb amplitude. The differential cross section involving these two amplitudes can be written as

$$\left(\frac{d\sigma}{d\Omega}\right)^{\pm} = \left| \mp |f_c| e^{i2\delta} + f_N \right|^2 , \qquad (27)$$

where f_c (f_n) stands for the Coulomb (nuclear) scattering amplitude and 2δ is a phase which includes the pure Coulomb phase and the relative

phase between the two scattering amplitudes. The upper sign corresponds to π^+ scattering and the lower to π^-.

In the evaluation of the Coulomb-nuclear interference term, the nuclear amplitude was parameterized following the work of Binon et al.[36] They measured the Coulomb-nuclear interference for π^--C^{12} elastic scattering over the 3-3 resonance. They used as the nuclear scattering amplitude the phenomenological expression

$$f_N(t) = \left[\mathrm{Re}\, f(0) + i\, \mathrm{Im}\, f(0)\right] e^{-\frac{1}{6}R_s^2|t|}, \quad \text{or}$$
$$f_N(t) = \mathrm{Im}\, f(0)\left[i+\alpha\right] e^{-\frac{1}{6}R_s^2|t|}, \tag{28}$$

where α = Ref(o)/Im f(o) and R_S was used to introduce a strong interaction r.m.s. radius. The parameter t is the squared four-momentum transfer

$$t = -2p^{*2}(1-\cos\Theta),$$

where p* and θ^* are the momentum and scattering angle in the center of mass system, respectively. The use of this nuclear amplitude was supported by previous data[40] in which the exponential decrease with $|t|$ of the elastic nuclear differential cross section was determined for $|t|$ values between the interference region and the first minimum. With the nuclear amplitude parameterized in this manner, the interference term of eq. (21) can be written as

$$\left(\frac{d\sigma}{d\Omega}\right)^{\pm}_{INTER} = \mp 2|f_c|\,\mathrm{Im}\, f(0)\, e^{-\frac{1}{6}R_s^2|t|}\left[\alpha\cos 2\delta \pm \sin 2\delta\right]. \tag{29}$$

The relative phase shift δ was obtained from an expression by

West and Yennie[41] and is given by

$$2\delta = -2\eta \sin\frac{\theta^*}{2} - \eta \int_{-4p^2}^{0} \frac{dt'}{|t'-t|}\left[1 - \frac{F_N(t')}{F_N(t)}\right], \qquad (30)$$

where η is the effective Coulomb coupling constant (eq. (23)). The phase shift, using the nuclear scattering amplitude of eq. (28), can be written as

$$2\delta = -\eta\left[2\ln\sin\frac{\theta^*}{2} + C + \ln(2p^{*2}R_s/3) - \sum_{N=1}^{\infty}\left(\frac{|t|R_s}{6}\right)^N/(N\cdot N!)\right], \qquad (31)$$

where C is Euler's constant (C = 0.5772).

For the evaluation of the interference term, the parameters R_s, α , and Im f(o) need to be determined for each target. The values for the carbon measurements were interpolated from the existing interference data on carbon.[36] The values of R_s for ^{9}Be and ^{3}He, which are representative of a strong interaction radius, were scaled from the carbon values assuming an $A^{1/3}$ dependence. The data proved to be insensitive to the value of R_s because of the range of momentum transfer covered in this work. The values of R_s determined in this matter were varied 20% from the scaled values and yielded an uncertainty of 0.3% or less in the final cross sections. The values of R_s used in making the Coulomb-nuclear interference correction, as well as the values of α used, are listed in Table V for each target.

In determining the parameter α , Binon demonstrated that for π^- scattering, the interference was constructive at energies below the π^- nucleus resonance and became destructive at energies above the

resonance. This characteristic feature of the interference gave a curve for Re f(o) that passed through zero at the π-nucleus resonance. Landau and Locher in reference (36) calculated Re f(o) from a dispersion relation using the total cross section for carbon from reference (40). They generated a curve for Re f(o) which agreed with the experimental results of Binon. The values of α for carbon could then be constructed from the calculated values of Re f(o) and the measured cross section. A plot of the parameter α for carbon over the energy range of this experiment yielded a curve ranging from the value of 0.2 at the low energies, passing through zero at the π-nucleus resonance and approaching the value -0.3 at 240 MeV.

Approximations to the values of α for ^{9}Be and ^{3}He were determined from the plot of α for carbon with the energy axis displaced such that the curve for α crossed the energy axis at the π-nuclear-resonance energy. The values of α determined in this manner were varied 20% and yielded an uncertainty of the order of 0.5% or less in the final cross section.

For the determination of the values for Im f(o) to be used in eq. (29), a "self-consistency" type of approach was used. A value for Im f(o) was first determined by the optical theorem, from the measured cross section without a Coulomb-nuclear interference correction. This value was used to make the interference correction, yielding a new cross section which, in turn, produced a new Im f(o) to be used in evaluating the interference correction. The iteration process was continued until a change of 0.01% or less in the total cross section occured. The process was usually terminated after three to four iterations. This "self-

consistency" method was tested for the carbon measurements, where previous total cross sections were available, and proved to be satisfactorily convergent.

The integration for the Coulomb-nuclear scattering interference was performed in the same manner as the Coulomb correction. A numerical integration was performed with the beam profile folded into the integral. The corrections arising from the interference were typically 1% or less of the total cross section near the resonance energy and increased to a 3% correction at energies off resonance. The values for Coulomb-nuclear interference corrections for π^+ and π^- cross section measurements are listed for carbon in Tables VI and VII; for beryllium-9 in Tables VIII and IX; and for helium-3 in Tables X and XI.

E. Beam Composition

Composition of the incident beam was determined by applying a Gauss-Seidel[42] least-squared fitting procedure to the pulse height spectra. Figs. 10-A, B show typical spectra and computer fits for the time-of-flight (TOF) system.

Peaks in the TOF spectra were initially assumed to be Gaussian and were fitted to the function

$$f(x) = A \exp\left[\frac{-(x-c)^2}{2\sigma^2}\right], \qquad (32)$$

where A is the amplitude of the peak, C is the center channel of the peak, and FWHM = $2\sqrt{2\ln 2}\,\sigma$ is the full width at half maximum. The fitting procedure varied the parameters A, C, and σ so as to minimize

the value of χ^2 which is defined as

$$\chi^2 = \sum_{i=1}^{N} \left[\frac{Y_i - f(x_i)}{\sqrt{Y_i}} \right]^2 , \tag{33}$$

where Y_i is the number of counts in the channel x_i and N is the number of channels included in the fit. The parameters were varied in such a way as to minimize χ^2 until the change in each parameter per iteration was less than .01%. The "goodness of fit" was measured by the variance of fit. This quantity is defined as the value of χ^2 divided by N - P, the number of points fitted minus the number of parameters, and is expected to have a value of 1.0 for a "perfect" fit.

In order to obtain good fits for the TOF spectra (variance of fit less than 1.5) it became necessary to modify the fitting function. Following Routti and Prussin,[43] each peak in the fitting code was described by a Gaussian with an exponential joined on either side. The exponentials were joined to the Gaussian so that the function and its first derivative were continuous. The fitting function can be represented by

$$\begin{aligned} f(x) &= A\exp\left[-(x-c)^2/2\sigma^2\right] && c-x_1 < x < c+x_2 \\ &= A\exp\left[\tfrac{1}{2}x_1(2x-2c+x_1)/\sigma\right] && x < c-x_1 \\ &= A\exp\left[\tfrac{1}{2}x_2(2c-2x+x_2)/\sigma\right] && x > c+x_2 \end{aligned} \tag{34}$$

where A, C, and σ are as defined in eq. (32), x_1 is the distance in channels to the lower junction point, and x_2 is the distance in channels to the upper junction point. In fitting the peaks, it was necessary

to add a tail only to the low side of the pion peak and to the high side of the muons. The junction points were treated as parameters and allowed to vary in the fitting procedure.

Although deviations of the peaks from a true Gaussian in the TOF spectra were not fully understood, it was felt that it could be attributed to fluctuations of time connected with the difference in length of the light paths from different parts of the scintillators. Several attempts to improve the TOF system, following the techniques of Charpak[44] and Ward[45] were made to eliminate resolution degradation caused by irregular light collection from the scintillant. These attempts consisted of viewing the scintillators from both ends by phototubes and forming two separate TOF systems. However, the TOF system as described in section C of Chapter III yielded the best resolution and was used in all TOF measurements.

The π and μ peaks in the TOF spectra were fitted with the function in eq. (34). The fitting procedure yielded the parameters for each peak with their associated errors. The area under the two curves was numerically integrated with the relative areas giving the beam composition. Errors on the beam composition were calculated using standard Gaussian statistics and represented one statistical standard deviation.

Electrons present in the beams used in the NMA4 area (Beam I) were few in number and could not be resolved in the TOF spectra. To determine the number of electrons present in a given spectrum, a standard procedure was to sum the spectrum in the region two standard deviations removed above the μ peak. The contributions of electrons determined in this manner were always less than .5%.

It was determined in calculating the cross section that because of the low electron contamination in the beam, the electrons could be treated as muons without any further increase in the uncertainty of the cross section. The positron contribution measured in Beam II (PTA) was also found to be small and treated in the same manner. The only cross section measurement in which the electron contamination was explicitly treated was the π^- measurement in Beam II. In this case, the electron contribution as shown in Fig. 12 was 17% of the incident beam.

For the TOF spectra with pion energies greater than 150 MeV, a constraint was applied to the fitting procedure. In these spectra, the fitting program could not resolve the π and μ peaks because of the similar flight times. The channel separation of the two peaks was calculated knowing the flight path interval and the time calibration of the pulse height analyzer. The spectra were fit with the channel separation of the centroids of the two peaks held constant. In this case, fits were performed over various channel intervals of the spectrum to check that the fit results were insensitive to the choice of interval. The composition of the incident beam in the Beam I area are listed in Table II.

For the measurement of beam composition in the Beam II area, the total absorption Cerenkov chamber was used. The composition of the incident beam used in Beam II (PTA) are listed in Table III. The Cerenkov counter was required in Beam II because of the higher energies available there. The counter also gave good energy resolution for pions and muons over the range of energies measured and thereby eliminated the difficulty encountered in the fitting procedure of the TOF system during

earlier runs.

Figs. 11-A, B, C show typical Cerenkov pulse height spectra for the positive incident beams. Fig. 12 shows the composition of the one π^- measurement made using Beam II. As shown in these spectra, the pion exhibits a peak with a low pulse height tail. This low tail can be attributed to pions which interact in flight with the fluorocarbon radiator, either by absorption or by scattering from the chamber. Pions interacting in this manner were assumed to be removed from the radiator without producing the full Cerenkov light that a pion exiting the downstream end of the chamber would produce.

In fitting the Cerenkov spectra, it was determined that over the range of energies measured, the low pulse height tail could be parameterized by

$$f(x) = \frac{C_1 (x - C_2)}{1 + \exp[C_3 (x - C_4)]} , \qquad (35)$$

where the C's were variable parameters in the fitting procedure. The pion peak of the spectra was fitted with a Gaussian. The muons in the spectra were fitted with a Gaussian with a low energy tail similar to eq. (34). The need for a tail on the low side of the muon peak was attributed to muons which Coulomb scattered out of the chamber. The beam composition was determined by a numerical integration of the fitted spectra with the relative areas giving the percentage of the beam constituents.

F. Decay Pions

It was necessary to apply a small correction to the cross section data for pions which missed counter T because of decay between target and counter T. The correction was applied only to the transmission counter T, since this counter normally received 90% of the transmitted beam and yielded the largest contribution to the final cross section.

From the kinematics for relativistic decay,[46] the maximum opening angle, θ_{LAB}^{MAX}, for the decay muon in the lab, is given by

$$\tan \theta_{LAB}^{MAX} = \frac{\beta^{\mu'}}{\gamma(\beta^2 - \beta^{\mu'2})^{\frac{1}{2}}},$$

where $\beta^{\mu'}$ is the velocity of the decay muon in the center of mass system, β is the velocity of the pion in the lab, and $\gamma = 1/(1-\beta^2)^{\frac{1}{2}}$. The decay cross-section in the lab system can be written as

$$\left(\frac{d\sigma}{d\Omega}\right)_{LAB} = N\left(\frac{d\Omega_{CM}}{d\Omega_{LAB}}\right) = NJ$$

where N, the decay cross section in the center of mass, is constant because of the isotropic decay of the pion. The symbol, J, represents the Jacobian for the transformation from the center mass to the lab system and is given by

$$J = \frac{\sin^2\phi'}{\sin^2\phi_L \cos\theta_L (\gamma \tan\theta_L \sin\phi' + \cos\phi')},$$

where the angle ϕ' is the center of mass angle and θ_L the corresponding lab angle. When the Jacobian is evaluated for the available lab angles, the decay cross section becomes singular at the maximum opening angle.

Under actual beam conditions, when the momentum resolution of the incident beam is folded into the theory, the cross section yields a sharp but finite peak at the maximum opening angle. Coulson et al.[47] have measured the angular distribution of the decay muons coming from a 12 cm. segment of an incident beam with a 5 cm x 5 cm cross sectional area and have shown the cross section to be sharply peaked at θ_{LAB}^{MAX} .

Since the decay cross section has the characteristic shape of a halo of muons propagating at the angle θ_{LAB}^{MAX} , the assumption was made that all decaying pions with θ_{LAB}^{MAX} greater than the angle subtended by counter T at the point of decay, produce muons which miss counter T. The correction for the pion decay was always smaller than 1% and was significant only at the higher energies when the transmission counters were at their furthermost point from the target. The corrections to the cross sections for pion decay are listed in Tables VI through XI for the three targets. For a large number of the transmission counter positions, no entry is given for the correction because the counter T, encompassed the halo of decay muons and no correction was needed.

G. Accidental Coincidences

A correction for accidental events was made for those events in which a transmitted particle was scattered outside the acceptance of a transmission counter, but because of a spurious count in the transmission counter, the particle appeared to have scattered into that counter. The spurious count may be caused by (1) a beam particle which missed the monitoring telescope but was registered in a transmission counter, or by (2) a second beam particle traversing the beam line within the resol-

ving time of the monitor trigger coincidence.

The use of the two anticoincidence counters, A_1 and A_2, aided in eliminating or reducing the random events described above in case (1). The contribution to the accidentals as described in case (2) was measured by forming a coincidence between the monitor trigger delayed and the transmission counter, to give $\alpha = (MT)_\Delta \cdot R_i$, where the subscript Δ indicated a signal delayed by one R. F. period of the cyclotron. The number of accidental coincidences, N_i for the i^{th} counter can then be written as [48]

$$N_i = \alpha (1 - r_i) \quad ,$$

where r_i = MT·R coincidences per MT, the probability that a particle traversed the target and was recorded in the i^{th} counter. The accidental coincidences measured in this manner were typically 1 to 2% of the recorded coincidences and yielded a correction of the order of 0.5% or less to the final cross section. Cross section corrections for accidental events for the three targets are given in Tables VI through XI.

H. Forward Nuclear Scattering

After all corrections to the annular counter events were made such that the remainder represents only nuclear events, the differential cross section measured by each annular counter was formed as given by eq. (8) (section B). For a given incident energy, the measured differential cross sections from each positioning of the transmission counters were combined to form one plot. The differential cross section generated in this manner was least-square fitted to an exponential in the

momentum transfer $|t|$ over the measured values. The functional fit was then extrapolated to zero degrees. Figs. 13 A, B, C show plots of the measured differential cross sections and the functional fit for carbon, beryllium, and helium-3, respectively.

The number of particles registering in the transmission counter T because of a nuclear event was calculated from eq. (7). The integral was evaluated numerically for each positon of the attenuation counter T, using the fitted differential cross section. Corrections to σ_T for $\pi^{\pm}$ and π^- forward nuclear scattering are given for carbon in Tables VI and VII; for beryllium-9 in Tables VIII and IX; and for helium-3 in Tables X and XI.

For the cross section measurement of π^+ and π^- on helium-3 at the two lowest energies, the measured differential cross section could not be fitted to an exponential in $|t|$. At these energies, the measurement differential cross section was flat with a slight rise for larger $|t|$ values. This deviation from an exponential could possibly be attributed to scattered pions in the ^{3}He target being rescattered by the stainless steel target chamber into one of the annular counters. This systematic error was possible because of the small target diameter and the nature of the distribution of scattered pions from a low Z element at low incident energies. The first minimum in the elastic differential cross section moves to larger angles as the incident energy or the target atomic number decreases.[49, 50]

To make the forward nuclear scattering corrections for these measurements, the average of the measured differential cross section was used to make the correction for the forward nuclear scattering. The

uncertainty in these corrections for the two low energy measurements on helium-3 is reflected in the quoted error for the final cross section.

I. Beam Rate, Counter Efficiency, and Target Size

Measurements were made of the observed cross section as a function of beam rate for one of the targets used. The measurement consisted of varying the internal current of the cyclotron for the incident energy with the highest count rate. The cross sections measured in this manner were found to be constant within the statistical counting uncertainty.

The efficiency of the attenuation counter, T, was measured under experimental conditions. The measurement consisted in positioning the counter between the two 1" diameter scintillators, S_1 and S_2. The efficiency of the counter was calculated from

$$\text{Efficiency}(T) = \left(\frac{1T2}{12}\right) * 100\% .$$

The efficiency measured in this manner was 99.7%. The assumption was made that the efficiency of the counter, T, was constant over the duration of the experiment. Based upon this assumption, the efficiency of the counter cancelled in the ratio of target empty to target full readings. Therefore, no correction to the cross sections was made for the efficiency of counter T.

The efficiencies of the four annular counters were not measured as described above because of the lack of beam time and the difficulty of such a measurement owing to the geometrical shape of the counters. From a comparison of the measured carbon cross section using the annular counters to existing cross section data, the efficiencies

of the annular counters were estimated to be 95% or greater. This level of efficiency was believed to have been maintained for all cross section measurements throughout this experiment. Voltage plateaus and delay curves for each of the annular counters were taken and rechecked throughout the course of the experiment. The output of each counter also gave well defined separations between the noise and beam particle pulse heights, indicative of a high efficiency.

As stated in section A of Chapter III, the use of an anticounter positioned before the scattering target can give rise to a systematic error. Beam particles in the monitor trigger can back scatter into the anticounter, vetoing the event as a good monitor trigger and thus yielding a low cross section. For those cross section measurements in which A_2 was in place, the number of particles back scattering into A_2 can be found by taking the difference in the coincidences $S12\bar{A}_1\bar{3}\bar{A}_2$ for target full and empty conditions normalized to the same number of monitor triggers. The number of particles back scattering into A_2 was typically less than 1% of the target full monitor triggers and yielded a 0.5% correction to the cross section.

As stated in section E of Chapter III, a second beryllium target was used to investigate the possible influence of target thickness upon the cross section measurement. For two incident negative energies, cross sections were measured using both beryllium targets. The measured values were found to be consistant within the statistical error.

J. Final Cross Sections and Errors

The final values for the total cross sections for each target

are given in Table XII. These values represent an average over the π cross section measured at each position of the transmission counters for an incident energy. Figs. 14, 15, and 16 show a plot of the total cross sections versus the lab kinetic energy for carbon, beryllium, and helium-3, respectively. Existing carbon and beryllium total cross sections[40, 51, 52, 53] are also included in Figs. 14 and 15. For the cross sections listed in Table XII and for the compilation of cross sections listed in Tables XIII - XV, no Coulomb distortion (section K) corrections have been included.

The uncertainties due to the various corrections were added in quadrature together with the statistical error for each position of the transmission counters. Finally the errors assigned to individual positions were added in quadrature to give the final error quoted in Table XII. Estimates for the uncertainties associated with a correction were generated by varying within reason the parameters used in making the correction. Uncertainties for the forward nuclear corrections were generated by adding in quadrature the errors on the curve fitting parameters. The statistical counting error, beam composition, and target thickness accounted for the main sources of error in this experiment.

K. Coulomb Distortion Corrections

In evaluating the integrals over the incident pion energy for both the sum-rule and the dispersion relation, the term $\Delta\sigma = \sigma^-(\pi^- A) - \sigma^+(\pi^+ A)$ in the integral is due to the nuclear interaction only. As shown in Fig. 14, the π^--carbon cross sections are significantly larger than

the π^+-carbon cross section. The difference was first measured by Clough[54] et al. who measured π^+ and π^- carbon cross sections under the same experimental setup from 90 to 850 MeV. This difference in the measured cross sections is viewed, not as a violation of charge independence, but is attributed to the distortion of the incident pion wave function by the Coulomb field. The positive pion is repelled by the nucleus and therefore, will not have the same impact parameter as a negative pion of the same incident energy which is attracted toward the nucleus. This Coulomb contribution to the $\pi^{\pm}$ nucleus cross sections has previously been calculated explicitly in a semi-classical approximation by Fäldt and Pilkuhen.[55] The corrections to the cross section differences for the Coulomb distortion are listed in Table XVI. As a point of interest it is noted that because of the isospin dependence of ^{9}Be and ^{3}He the Coulomb distortion correction made the ^{9}Be difference $(\sigma_{\pi^-} - \sigma_{\pi^+})$ less positive while the ^{3}He difference is more negative. A discussion of the correction for Coulomb distortion to the sum rule and to the dispersion relation will be given in Chapter V.

V. EVALUATION AND DISCUSSION OF RESULTS

In this section the numerical evaluation of the sum rule for nuclear beta decay (Eq. 35) will be made for ^{3}He, ^{7}Li and ^{9}Be. A range of values for the meson-exchange correction factor, ξ , and the ratio of the on-to-off shell coupling constants for the nucleon and the nucleus $K(0;\pi NN)/K(0;\pi NN_{\xi})$, which are compatible with these sum rule evaluations will be given. For the ^{9}Be evaluation, the compilation of $\pi^{\pm}$ - ^{9}Be cross sections in Table XIV has been combined with the ^{9}Be measurements of this work in generating the integral $I(m_{\pi}^{2};\pi N_{\xi})$ in the sum rule. Estimates for that portion of the ^{3}He integral at kinetic energies above 243 MeV which was not measured in this work are also presented. This estimate for the ^{3}He integral is taken directly from the measured fractional influence of ^{7}Li and ^{9}Be data above 243 MeV. The $\pi^{\pm}$ - ^{7}Li cross sections have been obtained from references (51) and (52) and are given in Table XV.

The remainder of this section will consist of an estimate of the effective pion-nuclear coupling constant for ^{3}He. A direct comparison of the multiple scattering calculation of $\sigma_{T}(\pi^{\pm}{}^{3}\mathrm{He})$ by Gurvitz will also be made with the ^{3}He cross section measurements in this work.

A. Sum Rule

In evaluating the sum rule for nuclear beta decay, the discussion will be presented in two parts. The first part will involve

the evaluation of the integral over the pion energy of the total cross section and the second part will involve the evaluation of the sum rule.

Before evaluating the integral $I(-M_\pi^2; \pi N_f)$, it is advantageous to review the general functional form of the integral. Rewriting eq. (32) of Chapter II,

$$I(-M_\pi^2; \pi N_f) = \frac{M_\pi^2}{\pi} \int_{M_\pi}^{\infty} \frac{dE_\pi \sqrt{E_\pi^2 - M_\pi^2}}{E_\pi^2} \left[\bar{\sigma}(M_\pi^2; \pi N_f) - \bar{\sigma}^+(-M_\pi^2; \pi N_f) \right],$$

we see that the explicit energy dependence of the integral has a form which peaks at the kinetic energy $(\sqrt{2} - 1) M_\pi$ and approaches a 1/E dependence for $E_\pi \gg M_\pi$. Measured $\pi^\pm$-nuclear cross sections are characterized by the 3/2-3/2 resonance which occurs approximately at the pion mass energy and which approach the same value about 1 BeV. When these characteristics of the integral are considered, the major contribution to the integral can be seen to come, therefore, from the 3/2-3/2 energy region.

In carrying out the integration, the measured cross sections were first smoothed using a smoothing function which fitted a least squared, one degree polynomal to three successive data points.[56] These smoothed values became the input to a spline-fit interpolation computer routine[57] which gave interpolated values for every MeV. The smoothing of the measured cross section was essential to the interpolating routine as the interpolated values oscillated strongly between the measured values when the data were not smoothed. The interpolated values were then used to evaluate $I(-M_\pi^2; \pi N_f)$ by a numerical intergration. The cross section curves which were generated in this way and used in integrating $I(-M_\pi^2; \pi N_f)$ are plotted as smooth curves in Figs. (15-A) and (16).

The low energy cross section region from $E_\pi = M_\pi$ (threshold) up to the lowest energy data position were generated by assuming a momentum cubed dependence for the cross sections. An extrapolation was made from the lowest measured cross section to zero kinetic energy. For the π^- ^{3}He data, a linear extrapolation was made using the measured cross section to 123 MeV and the generated momentum dependent cross sections started at that point. No attempt was made to match these two forms continuously.

As discussed in section K of Chapter IV, the measured cross section must be corrected for the Coulomb distortion of the incident pion wave functions. This correction was made using the semi-classical approach of Fäldt and Pilkuhn.(55) In making this correction to the measured cross section, it was necessary to impose a cutoff at an incident energy below which no correction was made. This was necessary because of the unrealistic divergence of the semi-classical model at low energies. The cutoff for ^{3}He, ^{7}Li and ^{9}Be was set at 70 MeV. This value was determined from two sources. The π^+ and π^- cross sections on carbon (Fig. 14-A), which is an isospin zero nucleus, converges below 70 MeV for which no further Coulomb distortion correction is necessary. Secondly, an evaluation of the effective-pion-nucleus coupling constant for ^{9}Be and ^{7}Li, produced agreement with the results of Squier, et al.(58) when the cutoff was taken at 70 MeV. The cutoff used in the evaluation of $I(-n_0^2; \pi N_0)$ was varied by 10 MeV and yielded a 4% change in $I(-n_0^2; \pi N_0)$.

The value of the integral, $I(-n_0^2; \pi N_0)$, for ^{9}Be yielded a value of 0.48 ± 0.08), while the ^{7}Li cross section yielded a value of 0.60 ± 0.09). The integral for the ^{3}He cross sections up to 243 MeV produced

a value of $-0.61 \pm .11$. The integral for the nucleon was also calculated using a compilation of nucleon data[59] up to 60 BeV and yielded a value of $-.50 \pm .01$.

As mentioned earlier in this chapter, the integrals of ^{9}Be and ^{7}Li were investigated to determine the degree to which the region above the 3/2-3/2 resonance contributed to the sum rule in beta decay. The values of these integrals up to 243 MeV determined in this manner produced 90% for beryllium and 93% for lithium of their normal values for which an upper limit of 1 BeV was taken. This relatively small contribution to the integral above 243 MeV is primarily due to the fact that the cross section curve for π^{+} and π^{-} cross at approximately 550 MeV. This crossing of the cross section curves, which is characteristic for isospin one-half nuclei, most likely reflects the influence of a higher I = 1/2 resonance. Since ^{3}He is an isospin one-half nucleus as well, the assumption is made that the $\pi^{\pm}$ - ^{3}He cross section will also cross and the contribution to the ^{3}He integral above 243 MeV would, therefore, be similar to that observed in ^{7}Li and ^{9}Be. For this reason the region above 243 MeV in ^{3}He was assumed to contribute an additional 8% to the integral. In assuming this 8% addition, the assumption is made that higher resonances in the ^{3}He cross sections, if present, would not be a dominant feature. This assumption is supported by the smearing of higher resonances by the Fermi motion in deuterium and helium-4.[60] As a final comment, it is noted that an evaluation of the integral $I(-n_{\pi}^{2};\pi p)$ to include only the 3/2-3/2 resonance yields 72% of its normal value. The value is representative of a maximum correction. With the 8% addition to the helium-3 integral, the final value is $-0.66 \pm .15$.

With the values of $I(-M_\pi^2; \pi N_f)$ for ^{3}He, ^{7}Li, and ^{9}Be and $I(-M_\pi^2; \pi p)$ stated above, the sum rule was evaluated. The values of the ratio $K(0;\pi m_p)/K(0;\pi N;N_f)$ for a range of values of the meson exchange correction factor ξ, from $\xi = -0.1$ to 0.1 have been plotted in Fig. 17. The curves for the three nuclei have the same characteristic shape with a negative slope. Kim and Primakoff[3] have estimated the meson exchange correction factor to be of the order of 0.05. Harper et al.[61] have calculated $\xi_{^3He}$ from experimental ft values for triton beta decay to be $\simeq 6\%$. These values of ξ indicated a ratio of $K(0;\pi m_p)/K(0;\pi N;N_f)$ of ≤ 1. This fact indicates that for the nuclei considered, the coupling constant moves off-shell slightly slower than the nucleon.

B. Effective Coupling Constant

Rewriting the expression for the effective coupling constant presented as eq.(41) in section B of Chapter II,

$$\Lambda_{eff} = \frac{M_\pi}{2} \mathrm{Re}\, f^-(M_\pi) - \frac{M_\pi^2}{8\pi^2} P\int_{\omega_0}^{\infty} \frac{d\omega' \Delta\sigma^-(\omega)}{k'} ,$$

we see that the term Λ_{eff} consists of three contributions: the value of Re $f^-(M_\pi)$; the integration over the physical region, $M_\pi < \omega < \infty$; and the integral over the unphysical region, $\omega_0 < \omega < M_\pi$. The evaluation of the integral over the physical region for ^{3}He was performed in the sum rule integral of Kim and Primakoff. The Coulomb distortion correction was cut off at 70 MeV and the low energy cross sections were generated by assuming a momentum cubed dependence. The contribution to the integral above 243 MeV was obtained in a manner similar to that for the K-P sum rule. The dispersion relation was evaluated for ^{9}Be and ^{7}Li

using the data in Tables XIV and XV. Termination of the integrals at 243 MeV produced 91% for ^{9}Be and 94% for ^{7}Li of the 1 BeV limit integration. With an 8% addition the contribution of the physical region to the coupling constant was (.037 $\pm$ .010).

For the contribution from the unphysical region, an attempt was made to parameterize the imaginary part of the antisymmetric amplitude according to eq. (42) of Chapter II. The antisymmetric scattering length can be written as

$$a^{-} = \frac{1}{2}\left(a_{\pi^{+}A} - a_{\pi^{-}A}\right),$$

where $a_{\pi^{\pm}A}$ are the $\pi^{\pm}$-A scattering length. The π^{-} scattering lengths can be obtained from π-pionic atoms. However, no experimental evaluation of $a_{\pi^{+}A}$ has been carried out. Ericson and Locher[11] have evaluated the contribution from the unphysical region for $Z = N \pm 1$ nuclei using effective π-nucleon scattering lengths. They obtained a value of 0.01 for the contribution from the unphysical region.

The value of Re $f^{-}(M_{\pi})$ has been determined by ref. 11 and ref. 58 from pionic atoms to have the value 0.048 $\pm$ 0.010 M_{π}^{-1}. The Re $f^{-}(M_{\pi})$ can be expressed as $1/3(\alpha_3 - \alpha_1)$ where α_1 and α_3 are the effective π-nucleon scattering lengths. The π-nuclear scattering length a_o was expressed as $1/3[2Z\ \alpha_1 + (3N + Z)\ \alpha_3]$.[62] Values for a_o from seven low Z nuclei were obtained from energy level shifts in pionic atoms[63, 64] and fit using a least squares method to give the effective values of α_1 and α_3.

Combining the three contributions, the effective pion-nuclear coupling constant for ^{3}He has the value (.071 $\pm$ .012). The values of

Ω_{eff} for ^{9}Be and ^{7}Li have been calculated recently by Squier et al.[58] using their measured cross sections. They obtained the values, $\Omega_{eff} = .068 \pm .008$ for ^{7}Li and $\Omega_{eff} = .061 \pm .007$ for ^{9}Be. Both of these values include a contribution of 0.01 from the unphysical region.

In a nuclear model where the nucleons in the nucleus are treated as free particles, the value of Ω_{eff} would presumably equal the pion-nucleon value of 0.08.[65] In this same model, the nuclear cross section would be equal to a value of A times the free pion-nucleon cross sections. The ratio of the effective pion-nuclear coupling constant to the pion-nucleon value can, therefore, be considered as a measure of nuclear shadowing effects.

C. Strong Interaction Model

To apply the expression for the total cross section developed by Gurvitz[12] to the ^{3}He case, the isospin dependence of the ^{3}He nucleus must be taken into account. The three terms in the expression for the total cross section for single, double and triple scattering can be replaced for ^{3}He as the following:

1) Single $\quad 3\sigma_{\pi N}^{TOT} \rightarrow \sigma_{\pi p} + \sigma_{\pi p} + \sigma_{\pi n}$

2) Double $\quad \frac{3\pi^2}{16\pi}\left(\sigma_{\pi N}^{TOT}\right)^2 \rightarrow \frac{\pi^2}{16\pi}\left[\sigma_{\pi p}\sigma_{\pi p} + \sigma_{\pi p}\sigma_{\pi n} + \sigma_{\pi n}\sigma_{\pi p}\right]$

3) Triple $\quad \frac{\pi^4}{192\pi^2}\left(\sigma_{\pi N}\right)^3 \rightarrow \frac{\pi^4}{192\pi^2}\sigma_{\pi p}\sigma_{\pi p}\sigma_{\pi n}$

Evaluating this expression at the nucleon's 3/2-3/2 resonance (i.e. α = 0) and using as input values

$$\sigma_{\pi^+ p} = \sigma_{\pi^- n} = 200 \text{ mb}$$

$$\sigma_{\pi^- p} = \sigma_{\pi^+ n} = 70 \text{ mb} \quad ,$$

the following π - ^{3}He cross sections are computed:

$$\sigma_{\pi^+ {}^3\text{He}} = 340 \text{ mb}$$

$$\sigma_{\pi^- {}^3\text{He}} = 280 \text{ mb}$$

Although Gurvitz's model does not predict any energy shift of the 3/2-3/2 resonance for the 3-nucleon system, the magnitude of the nuclear cross sections at resonance are found to be in good agreement with this work. These are to be compared to our experimental values of 340 mb for $\sigma(\pi^+ - {}^3\text{He})$ and 260 mb for $\sigma(\pi^- - {}^3\text{He})$.

VI. APPENDICES

Appendix I

The sum over the intermediate state can be written as

$$\sum_{N_s} = \sum_{\text{below}}^{\text{disc.}} + \sum_{\text{below}}^{\text{cont.}} + \sum_{\text{Above}}^{\text{cont.}},$$

where 1) $\sum_{\text{below}}^{\text{disc.}}$ contains all states with $M_s \simeq M_f$ (with isospin invariance)

2) $\sum_{\text{below}}^{\text{cont.}}$ contains all continuum states below $\pi + N_f$ threshold

3) $\sum_{\text{Above}}^{\text{cont.}}$ contains all states above $\pi + N_f$ threshold

For example, the sum of the intermediate states for the independent cases in which the final nucleus is first p and then ^{3}He can be written as:

$N_f = p$

$\sum_{\text{below}}^{\text{disc}}$ $|s\rangle$: n $|s'\rangle$: NONE

$\sum_{\text{below}}^{\text{cont.}}$ $|s\rangle$: NONE $|s'\rangle$: NONE

$\sum_{\text{Above}}^{\text{cont.}}$ $|s\rangle$: $\pi^0 n$; $\pi^- p$ $|s'\rangle$: $\pi^+ p$

$N_f = {}^3He$

$\sum_{\text{below}}^{\text{disc}}$ $|s\rangle$: ${}^3H$; ${}^3He^*$ $\qquad$ $|s'\rangle$: NONE

$\sum_{\text{below}}^{\text{Cont.}}$ $|s\rangle$: nd, nnp $\qquad$ $|s'\rangle$: ppp

$\sum_{\text{Above}}^{\text{Cont}}$ $|s\rangle$: $\pi^0 {}^3He$; $\pi^- {}^3H$ $\qquad$ $|s'\rangle$: $\pi^+ {}^3He$

APPENDIX II

The sum over the states above the threshold,

$$\sum_{\text{Above}} = \sum_{N_s} |\langle N_f | Q_A^+(0) | N_s \rangle|^2 - \sum_{N_s} |\langle N_f | Q_A^-(0) | N_s \rangle|^2 ,$$

can be evaluated following an Adler-Weisberger procedure. These sums can be rewritten in terms of the divergence of the axial-vector current using the following identities:

$$\langle N_f | \partial_\lambda j_\lambda^A(0) | N_s \rangle = \frac{1}{i}(P_f - P_s)_\lambda \langle N_f | j_\lambda^A(0) | N_s \rangle ,$$

$$\langle N_f | j_4^A(0) | N_s \rangle = \frac{1}{(\epsilon_f - \epsilon_s)} \left[\langle N_f | \partial_\lambda j_\lambda^A(0) | N_s \rangle - \frac{1}{i}(\vec{P}_f - \vec{P}_s) \langle N_f | j_4^A(0) | N_s \rangle \right] ,$$

and

$$\langle N_f | Q_A^+(0) | N_s \rangle \equiv \frac{1}{i} \int d^3x \langle N_f | j_4^A(\vec{x}, 0) | N_s \rangle = \frac{1}{i} (2\pi)^3 \delta^3(\vec{P}_f - \vec{P}_s) \langle N_f | j_4^A(0) | N_s \rangle ,$$

where translational invariance has been used in writing the last terms. These identities allow the matrix element of $Q_A(o)$ to be written as

$$\langle N_f | Q_A^+(0) | N_s \rangle = (2\pi)^3 \delta^3(\vec{P}_f - \vec{P}_s) \frac{1}{i(\epsilon_f - \epsilon_s)} \langle N_f | \partial_\lambda j_\lambda^A(0) | N_s \rangle ,$$

where for the sum over the states above threshold, $\epsilon_f = \epsilon_s$.

Considering the sum over N_s, this term can be written as

$$\sum_{N_s} = \left| \sum_{N_s} (2\pi)^3 \delta^3(\vec{P}_f - \vec{P}_s) \left(\frac{1}{i(\epsilon_f - \epsilon_s)} \right) \langle N_f | \partial_\lambda j_\lambda^A(0) | N_s \rangle \right.$$

$$= \sum_{N_s} (2\pi)^6 \delta^3(\vec{P}_f - \vec{P}_s) \left| \frac{1}{\epsilon_f - \epsilon_s} \right|^2 \left| \langle N_f | \partial_\lambda j_\lambda^A(0) | N_s \rangle \right|^2 .$$

This expression contains a 3-momentum conservation only. Following the procedure of Bell,[16] this expression can be changed to a formal 4-momentum conservation where ϵ_f is allowed to be a "free" parameter. The sum over the states, N_s can be written as

$$\sum_{N_s} = \left(\frac{1}{2\pi}\right)\int \frac{d\Delta}{\Delta^2} \sum_{N_s} (2\pi)^4 \delta^4(P_f - P_s - q) \left|\langle N_f | \partial_\lambda J_\lambda^A(0) | N_s \rangle\right|^2,$$

where $\Delta = \epsilon_f - \epsilon_s$ and $q = (0, i\Delta)$.

Using covariance, the dependence of $\langle N_f | \partial_\lambda J_\lambda^A(0) | N_s \rangle$ on ϵ_f can be extracted by evaluating the sum in the lab (prime) frame. The sum can be written as

$$\sum_{s} = \left(\frac{1}{2\pi}\right)\int \frac{d\epsilon_{q'}}{\epsilon_{q'}} \sum_{N_s} (2\pi)^4 \delta^4(p_f' - p_s - q') \left|\langle N_f(p_f'=0) | \partial_\lambda J_\lambda^A(0) | N_s \rangle\right|^2.$$

Using PCAC

$$\partial_\lambda J_\lambda^A(0) = a_\pi M_\pi^2 \Phi_{\pi^-},$$

$$\left[\Box^2 - M_\pi^2\right]\Phi_{\pi^-} = -J_{\pi^-},$$

this sum can be written as

$$\sum_{N_s} = \left(\frac{1}{2\pi}\right)\int \frac{d\epsilon_{q'}}{\epsilon_{q'}} \sum_{N_s} (2\pi)^4 \delta^4(p_f' - p_s - q') \frac{a_\pi M_\pi^2}{q^2 + M_\pi^2} \left|\langle N_f(p_f'=0) | J_{\pi^-} | N_s \rangle\right|^2,$$

$$= \left(\frac{1}{2\pi}\right)\int \frac{d\epsilon_{q'}}{\epsilon_{q'}} \sum_{N_s} (2\pi)^4 \delta^4(p_f' - p_s - q') \frac{a_\pi M_\pi^2}{q^2 + M_\pi^2} \left|\langle N_s | J_{\pi^-}^\dagger | N_f(p_f'=0) \rangle\right|^2.$$

From the definition for total cross sections which can be written as

$$\left[2\pi |V_{\pi N_f}| \sigma_{\pi^- N_f}^{\text{Total}}\right]_{\substack{\text{ANY} \\ \text{FRAME}}} = \sum_{N_s} (2\pi)^4 \delta^4(p' - p_s - q') \left|\langle N_s | J_{\pi^-}^\dagger | N_f \rangle\right|^2.$$

The sum over the states, N_s, can be written in the limit $V_f \to 1$ (as $q \to 0$)

$$\sum_{N_s} \longrightarrow \frac{a_\pi^2}{M_\pi^2} \left| f(0; \pi N_s N_f) \right|^2 \frac{1}{\pi} \int_{M_s}^{\infty} \frac{dE_{q'}}{E_{q'}^2} \left[|q'| \, \sigma_{\pi^- N_f}^{\text{TOTAL}} \right] .$$

A similar term holds for the sum over $N_{s'}$. The combined term for the sum of states above the threshold can be written as

$$\sum_{\text{Above}} \longrightarrow \frac{a_I^2}{M_\pi^2} \left| f(0; \pi N_I N_f) \right|^2 \frac{1}{\pi} \int_{M_\pi}^{\infty} \frac{dE_{q'}}{E_{q'}^2} \left[|q'| \left\{ \sigma_{\pi^- N_b} - \sigma_{\pi^+ N_f} \right\} \right]_{LAB} .$$

VII. ACKNOWLEDGEMENTS

The author wishes to acknowledge the assistance and support received from the following persons:

Dr. John R. Kane, his advisor, for his continued guidance and aid during the course of the experiment and in the preparation of this manuscript.

Drs. J. Carroll and C. H. Hsieh, for aid and support both during the preparation for the experiment and in the taking of experimental data.

Dr. Y. Y. Yam, for helpful discussions of the sum rule and the dispersion relations, and a careful reading of the manuscript.

Drs. M. Eckhause and B. O. Sapp for aid rendered during the collection of the experimental data.

Drs. H. O. Funsten, R. G. Winter and R. A. Orwall for reading the manuscript.

Mr. Stanley G. Hummel and the Physics Department machine shop, for the excellent construction of much of the equipment.

Dr. R. T. Siegel and the staff of the Space Radiation Effects Laboratory, for their efficient operation of the synchrocyclotron and aid rendered during the collection of the experimental data.

The staff of the William and Mary Computer Center for their aid during the analysis of the experimental data.

Messrs. M. Mattie, B. Buckheit and D. Buckle for aid rendered during the taking of the experimental data.

Mr. R. Hill for help in analyzing the experimental data.

Drs. S. P. Agarwal, S. Johnston and J. C. Wells for help in collecting the experimental data.

Mrs. Katharine H. Nelson for typing the manuscript.

His wife, Lynn, for constant support in various tasks of punching, typing, and proof reading and for being a constant ray of sunshine.

The U. S. Government for financial aid in the form of an NDEA Fellowship.

VIII. REFERENCES

1. C. W. Kim and H. Primakoff, Phys. Rev. 139, B1447 (1965).
2. C. W. Kim and H. Primakoff, Phys. Rev. 140, B566 (1965).
3. C. W. Kim and H. Primakoff, Phys. Rev. 147, 1034 (1965).
4. C. W. Kim, Phys. Rev. 151, 1261 (1966).
5. H. Primakoff, High Energy Physics and Nuclear Structure, 409, (1969).
6. S. L. Adler, Phys. Rev. 140, B736 (1965).
7. W. Weisberger, Phys. Rev. 143, 1302 (1966).
8. M. Gell-Mann, Phys. Rev. 125 (1962); Physics 1, 63 (1964).
9. Y. Nambu, Phys. Rev. 4, 380 (1960).
10. J. Bernstein, S. Fubni, M. Gell-Mann, and W. Thirring, Nuovo Cimento 17, 757 (1960).
11. T. E. O. Ericson and M. P. Locher, Nucl. Phys. A148, 1 (1970).
12. S. A. Gurvitz, Sov. Journal of Nucl. Phys. 10, 182 (1970).
13. R. P. Feynman and M. Gell-Mann, Phys. Rev. 109, 193 (1958).
14. G. Feinberg and L. M. Lederman, Ann. Rev. Nucl. Sci., 13, 105 (1963).
15. J. Hamilton and W. S. Woolcock, Rev. Mod. Phys. 35, 737 (1963).
16. J. S. Bell and R. J. Blin-stoyle, Nucl. Phys. 6, 87 (1958).
17. For example, see J. D. Jackson, Dispersion Relations, G. R. Screaton, ed., Oliver and Boyd, Ltd., Edinburgh (1960).
18. M. L. Goldberger, H. Miyazawa and R. Oehme, Phys. Rev. 99, 986 (1955).
19. G. Hohler, H. Schlaile and R. Strauss, Z. Phys. 229, 217 (1969).
20. V. K. Samaranayake and W. S. Woolcock, Nucl. Phys. B48, 205 (1972).

21. G. Fäldt, Nucl. Phys. B10, 597 (1969).

22. T. L. Trueman, Nucl. Phys. 26, 57 (1961).

23. R. J. Glauber, In Lectures in Theoretical Physics, W. E. Britten, et al. ed., Vol. 1, Interscience Publishers, Inc., New York, 315 (1959).

24. V. N. Gribov, Zh. Eksp. Teor. Fiz. 56, 892 (1969).

25. C. Richard-Serre, M. J. M. Saltmarsh, D. F. Measday, Nucl. Instr. and Methods 63, 173 (1968).

26. W. S. Risk, Design of a Pi Meson Beam for the Extracted Proton Beam at the SREL 600 MeV Cyclotron, (unpublished).

27. D. C. Buckle, J. R. Kane, B. D. Orrick, R. T. Siegel, and R. J. Wetmore, Nucl. Instr. and Methods, 77, 249 (1970).

28. R. S. Hickman, R. W. Kenney, R. C. Mathewson, and R. A. Perkins Rev. Sci. Instr. 30, 983 (1959).

29. K. L. Erdman, L. P. Robertson, D. Axen, and J. R. MacDonald, Rev. Sci. Instr. 34, 1280 (1963).

30. W. E. Keller, Helium 3 and Helium 4, Plenum Press, New York, N. Y. (1969).

31. R. Gilmont, Ind. Eng. Cheml. Anal. 18, 633 (1946).

32. H. Lewis, Phys. Rev. 78, 526 (1950).

33. J. F. Janni, Calculations of Energy Loss Range, Pathlength, Straggling, Multiple Scattering and the Probability of Inelastic Nuclear Collisions for 0.1 to 1000 MeV Protons, Tech. Report No. AFWL-TR-65-150, (1966).

34. SREL 600 MeV Cyclotron Handbook, College of William and Mary (1964).

35. W. S. Risk, private communication.

36. R. M. Sterheimer, Phys. Rev. 117, 485 (1960).

37. F. Binon, V. Bobyr, P. Duteil, M. Gouanere, L. Hugon, J. P. Peigneux, J. Renuart, C. Schmit, M. Spighel, and J. P. Stroot, Nucl. Phys. B33, 42 (1971).

38. R. Hofstadter, Ann. Rev. Nucl. Sci. 7, 274 (1957).

39. K. Okamoto and C. Lucas, Nucl. Phys. B2, 347 (1967).

40. R. M. Sternheimer, Rev. Sci. Instr. 25, 1070 (1954).

41. F. Binon, P. Duteil, J. P. Garron, J. Görres, L. Hugon, J. P. Peigneux, C. Schmit, M. Spighel, and J. P. Stroot, Nucl. Phys. B17, 168 (1970).

42. G. B. West and D. R. Yennie, Phys. Rev. 172, 1413 (1968).

43. R. H. Moore and R. K. Zeigler, LA-2367, Los Alamos Scientific Laboratory, (1959).

44. J. T. Routti and S. G. Purssin, Nucl. Instr. and Methods 72, 125 (1969).

45. G. Carpak, L. Dick, and L. Feuvrais, Nucl. Instr. and Methods 15, 323 (1962).

46. C. Ward, A. Berick, E. Tagliaferri, and C. York, Nucl. Instr. and Methods 30, 61 (1964).

47. R. Hddeorn, Relativistic Kinematics, W. A. Benjamin, New York (1964).

48. L. V. Coulson, C. R. Fletcher, E. V. Hungerford, G. S. Mutchler, G. C. Phillips, M. L. Scott, J. C. Allred, C. Goodman, and B. W. Mayes, Nucl. Instr. and Methods 101, 247 (1972).

49. D. V. Bugg, D. C. Salter, G. H. Stafford, R. F. George, K. F. Riley, and R. J. Tapper, Phys. Rev. 146, 980 (1966).

50. L. S. Kisslinger, Phys. Rev. 98, 761 (1955).

51. R. M. Edelstein, W. F. Baker, and J. Rainwater, Phys. Rev. 122, 252 (1961).

52. B. W. Allardyce, C. J. Batty, D. J. Baugh, W. J. McDonald, R. A. J. Riddle, L. H. Watson, M. E. Cage, G. J. Pyle, G. T. A. Squier, A. S. Clough and G. K. Turner, High Energy Physics Division, Rutherford Laboratory, RL-73-038 (1973) (unpublished).

53. C. Wilkin, C. R. Cox, J. J. Dimingo, K. Gahathuler, E. Pedroni, J. Rohlin, P. Schwaller and N. M. Tanner, Nucl. Phys. (to be published).

54. N. D. Gabitzsch, G. S. Mutchler, C. R. Fletcher, E. V. Hungerford, III, L. Coulson, D. Mann, T. Witten, M. Furic, G. C. Phillips, B. Mayes, L. Y. Lee, J. Hudomalj, J. C. Allred, and C. Goodman, Phys. Lett. (to be published).

55. A. S. Clough, G. K. Turner, B. W. Allardyce, G. J. Batty, D. J. Baugh, W. J. McDonald, R. A. J. Riddle, L. H. Watson, M. E. Cage, G. J. Pyle and G. T. A. Squier, Phys. Lett. B43, 476 (1973).

56. G. Fäldt and H. Pilkuhn, Phys. Lett. B40, 613 (1972).

57. See F. B. Hildebrand, Introduction to Numerical Analysis, McGraw-Hill, New York (1956) pp. 258-311.

58. See. R. H. Pennington, Computer Methods and Numerical Analysis, MacMillan Co., London, 1965 p. 445.

59. G. T. A. Squier, M. E. Cage, C. J. Pyle, A. S. Clough, G. K. Turner, B. W. Allardyce, C. J. Batty, D. J. Baugh, W. J. McDonald, R. A. J. Riddle, L. H. Watson, High Energy Physics Division, Rutherford Laboratory, RL-73-037 (1973) (unpublished).

60. Compilation of $\pm$ p cross sections, CERN Report, Giacomelli (1969).

61. See the cross section curves in ref. 11.

62. E. P. Harper, Y. E. Kim, A. Tubis, and M. Rho, Phys. Lett. B40, 533 (1972).

63. S. Deser, M. L. Goldberger, K. Baumann and W. Thirrey, Phys. Rev. 96, 774 (1954).

64. R. J. Harris, Jr., W. B. Shuler, M. Eckhause, R. T. Siegel and R. E. Welsh, Phys. Rev. Lett. 20, 505 (1968).

65. G. Bachenstoss, Ann. Rev. Nucl. Sci. 20, 467 (1970).

66. M. Ericson, Ann. Phys. 63, 562 (1971).

IX. TABLES

TABLE I.

Counter Geometries. All measurements for the counters are given in inches.

Range Telescope:	Counter	(X,Y,Z)		
	W1	2,2,1/4		
	W2	2,2,1/4		
	W3	5,5,1/16		
	W4	10,10,1/4		
Incident Beam Telescope:	Counter	Diameter	Thickness	
	S1	2	1/8	
	S2	1	1/8	
	S3	1	1/32	
	(S4)	1	1/8	
	A1	1 1/8 (anti-hole)	8,8,1/4	
	A2	1 1/4 (anti-hole)	6,6,1/4	
Transmission Counters:	Counter	Inside Diameter	Outside Diameter	Thickness
	T	--	3.50	1/16
	R1	3.62	5.5	1/2
	R2	5.62	7.5	1/2
	R3	7.63	9.5	1/2
	R4	9.64	12.0	1/2
Other Counter Used:				
TOF	T1	2,2,1/4		
	T2	2,2,2		
Profile Counter		1/4,1/4,1/4		
Cerenkov Chamber		16, 4-1/2 (Dia.)		

TABLE II.

Beam Characteristics for Beam I

	Energy (Incident) (MeV)	Degrader (g/cm^2)	MT/sec	Pion Composition (Per cent)
I. First Data Run	228[a]	-----	650	88.4 ± 1.0
		11.4[b]	200	85.1 ± 0.8
		22.8[b]	100	81.8 ± 0.7
		34.1[b]	60	78.6 ± 0.6
		45.5[b]	40	75.5 ± 0.6
II. Second Data Run	237[a]	-----	1500	87.0 ± 0.8
		2.5[c]		84.5 ± 0.8
	187[a]	21.9[c]	250	77.2 ± 0.6
		24.4[c]		74.3 ± 0.6
	157[a]	35.9[c]	80	68.5 ± 0.5
		38.4[c]		68.0 ± 0.5

a) Energies measures by range curve
b) Cu (g/cm^2) degrader positioned after bending magnet
c) CH_2 (g/cm^2) degrader positioned before bending magnet

TABLE III.

Beam Characteristics for Beam II

	Energy (Incident) (MeV)	CH_2 (Production tgt.) (Inches)	Degrader (Inches)	MT/sec	Pion Composition (Per cent)
I. Positive Beam	127	18	9.4 (CH_2)	200	83.4 ± 0.4
	153	18	4.7 (CH_2)	250	88.2 ± 0.4
	178	18	---------	1.75 K	93.1 ± 0.4
	204	12	---------	2.75 K	96.0 ± 0.4
	222	9 3/8	---------	2.9 K	96.5 ± 0.5
	246	5 1/2	---------	1.8 K	97.0 ± 0.8
	270	4 1/2	---------	------	----------
	290	3 1/2	---------	------	----------
II. Negative Beam	204	6 (Graphite)	---------	50	75.6 ± 0.6 (μ= 7.1 ± 0.5) (e=17.3 ± 0.5)

TABLE IV.

Target Dimensions and Properties

Target	Surface Dimensions (Inches)	Thickness (Inches)	Density (g/cm^3)	No. Atoms
Carbon	x:5.696 ± .005 y:5.699 ± .005	.660 ± .005	1.33 ± .01	.112 ± .001x10^{24}
Beryllium	x:5.090 ± .005 y:5.115 ± .005	.720 ± .005	1.85 ± .01	.226 ± .001x10^{24}
		.410 ± .005		.128 ± .001x10^{24}
Liquid ^{3}He Mylar Window	2.375 ± .005 (Dia.)	2.575 ± .009	.071 ± .006	.929 ± .008x10^{23}
Stainless Window	2.375 ± .005	2.580 ± .010	.070 ± .006	.924 ± .009x10^{23}

TABLE V.

Values for the Parameters α and R_s used in the Coulomb-nuclear interference correction.

I. Carbon-12

Energy (MeV)	α	R_s(fm)	Energy (MeV)	α	R_s(fm)
121	0.21	3.47	97	.37	3.65
147	0.05	3.34	134	.13	3.40
172	-0.08	3.21	142	.08	3.36
198	-0.18	3.09	146	.06	3.35
216	-0.23	3.00	171	-.07	3.23
240	-0.29	2.90	175	-.09	3.20
			204	-.20	3.06
			223	-.25	2.98
			227	-.26	2.96

II. Beryllium-9

Energy (MeV)	α	R_s(fm)	Energy (MeV)	α	R_s(fm)
120	.25	3.15	96	.40	3.30
146	.09	3.02	141	0.11	3.06
171	-.05	2.91	146	0.08	3.04
198	-.16	2.82	170	-0.05	2.93
215	-.22	2.73	203	-.18	2.78
240	-.28	2.63	223	-.24	2.71
			227	-.25	2.70

III. Helium-3

Energy (MeV)	α	R_s(fm)	Energy (MeV)	α	R_s(fm)
123	.27	2.19	141	0.15	2.12
151	.08	2.10	146	0.11	2.10
176	-.05	2.02	157	0.05	2.06
202	-.16	1.95	162	0.20	2.05
219	-.22	1.89	175	-0.45	2.00
243	-.28	1.83	179	-0.65	1.99
			202	-0.16	1.93
			209	-0.18	1.92
			213	-0.20	1.90

TABLE VI.

Correction to total cross section measurements for π^+-Carbon-12. All corrections are in millibarns. The uncorrected column represents eq. (5) of Chapter IV. The ring position is the distance in inches between the center of the target and counter T.

Energy (MeV)	Ring Position	Uncorrected (Raw Data)	Accidentals	Muon Contam.	μ-Decay	Coulomb	Coul-Nucl.	Forward Scattering
121	8.5	509.0	0.5	104.9	-2.9	-12.5	17.5	29.6
	12.4	475.3	0.4	99.5	----	- 5.1	12.2	58.4
147	8.5	566.4	0.5	79.6	-1.7	- 8.6	6.5	36.6
	12.4	536.6	0.4	75.7	----	- 3.3	4.2	71.3
172	8.5	619.6	0.6	48.9	-4.4	-11.9	-0.8	25.9
	12.4	589.9	0.6	47.1	-0.4	- 6.3	-1.4	42.8
	16.3	544.2	0.5	43.4	----	- 2.3	-1.1	82.7
198	12.4	598.9	1.7	26.2	-3.0	- 9.5	-7.0	25.9
	16.3	571.4	1.7	25.3	----	- 4.7	-6.2	44.2
216	12.4	572.3	1.0	21.8	-2.0	- 7.9	-9.3	25.4
	16.3	541.2	1.1	20.7	----	- 3.8	-7.8	43.4
241	12.4	533.6	0.5	16.8	-0.9	- 6.3	-11.0	25.4
	16.3	501.9	0.4	16.1	----	- 2.9	-8.9	43.3

TABLE VII.

Correction to total cross section measurements for π^--Carbon-12. All corrections are in millibarns. The uncorrected column represents eq. (5) of Chapter IV. The ring position is the distance in inches between the center of the target and counter T.

Energy (MeV)	Ring Position	Uncorrected (Raw Data)	Accidentals	Muon Contam.	μ-Decay	Coulomb	Coul-Nucl.	Forward Scattering
97	10.8	407.2	0.1	209.9	-1.9	-14.0	-26.8	68.1
134	10.8	488.4	0.1	166.1	-0.6	- 7.4	- 5.9	51.8
142	16.6	472.8	0.3	231.6	-4.4	-20.4	- 0.1	18.1
146	16.6	502.3	0.3	191.3	-4.8	-19.3	1.5	26.1
171	16.6	507.1	0.4	161.4	-3.7	-14.2	10.1	24.8
175	16.6	497.5	0.4	158.1	-3.4	-13.7	10.9	26.9
204	10.8	492.3	0.5	67.6	----	- 3.0	14.7	59.2
223	16.6	469.3	0.7	94.7	-1.6	- 8.3	16.9	28.3
227	16.6	461.2	0.7	107.8	-1.4	- 7.9	16.9	26.4

TABLE VIII.

Corrections to total cross section measurement for π^+-Beryllium-9. All corrections are in millibarns. The uncorrected column represents eq. (5) of Chapter IV. The ring position is the distance in inches between the center of the target and counter T.

Energy (MeV)	Ring Position	Uncorrected (Raw Data)	Accidentals	Muon Contam.	μ -Decay	Coulomb	Coul-Nucl.	Forward Scattering
120	8.4	409.1	0.4	87.5	-2.3	-5.9	9.0	19.5
	12.3	383.1	0.3	82.5	----	-2.4	6.5	38.7
146	8.4	469.6	0.4	70.1	-1.4	-4.1	3.9	26.1
	12.3	450.4	0.3	68.5	----	-1.6	2.6	51.4
171	12.3	503.0	0.5	41.4	-0.4	-3.0	-0.4	32.2
	16.2	467.2	0.5	39.2	----	-1.1	-0.2	62.8
198	12.3	501.1	1.0	27.9	-0.6	-4.5	-3.0	18.1
	16.2	481.4	1.1	22.0	----	-2.2	-2.7	30.9
215	12.3	474.0	0.8	18.7	-1.7	-3.8	-4.4	17.8
	16.2	454.5	0.8	18.0	----	-1.9	-3.7	30.7
240	12.3	434.4	0.4	14.5	-0.7	-3.0	-5.2	17.9
	16.3	421.8	0.5	14.0	----	-1.4	-4.3	30.8

TABLE IX.

Corrections to total cross section measurements for π^--Beryllium-9. All corrections are in millibarns. The uncorrected column represents eq. (5) of Chapter IV. The ring position is the distance in inches between the center of the target and counter T.

Energy (MeV)	Ring Position	Uncorrected (Raw Data)	Accidentals	Muon Contam.	μ-Decay	Coulomb	Coul-Nucl.	Forward Scattering
96	10.8	338.9	0.1	181.0	-1.6	-16.6	-18.5	36.4
141	16.6	425.3	0.3	192.2	-4.0	-10.0	- 2.9	17.2
146	16.6	435.7	0.3	205.1	-3.7	- 8.6	- 1.4	21.8
170	16.6	467.4	0.4	153.2	-3.5	- 6.9	4.8	21.6
203	10.8	459.1	0.5	65.0	----	- 1.5	8.5	46.3
223	16.6	429.0	0.6	86.2	-1.6	- 4.1	10.0	22.6
227	16.6	414.4	0.6	80.4	-1.3	- 3.6	9.4	24.2

TABLE X.

Corrections to total cross section measurements for π^+-Helium-3. All corrections are in millibarns. The uncorrected column represents eq.(5) of Chapter IV. The ring position is the distance in inches between the center of the target and counter T.

Energy (MeV)	Ring Position	Uncorrected (Raw Data)	Accidentals	Muon Contam.	μ-Decay	Coulomb	Coul-Nucl.	Forward Scattering
123	13.2	230.5	0.1	50.9	-3.2	-3.9	3.7	2.5
	17.2	219.9	0.1	48.9	-1.5	-1.6	3.5	4.3
151	13.2	296.3	0.1	44.3	-3.0	-1.9	1.7	4.5
	17.2	289.2	0.1	43.4	-1.0	-1.1	1.5	7.6
176	13.2	302.7	0.3	24.5	-2.3	-1.4	-0.2	7.1
	17.2	299.4	0.3	23.8	-0.4	0.8	-0.3	11.8
202	13.2	290.4	0.5	12.9	-1.5	-1.1	-1.5	8.5
	17.2	282.6	0.5	12.6	----	-0.6	-1.4	12.9
219	13.2	250.2	1.2	9.5	-0.9	-0.9	-1.7	7.1
	17.2	239.3	0.7	9.1	----	-0.5	-1.6	11.7
243	13.2	218.4	0.3	7.0	-0.4	0.8	-1.9	7.7
	17.2	216.5	0.1	6.9	----	0.4	-1.7	12.7

TABLE XI.

Corrections to total cross section measurements for π^--Helium-3. All corrections are in millibarns. The uncorrected column represents eq. (5) of Chapter IV. The ring position is the distance in inches between the center of the target and counter T.

Energy (MeV)	Ring Position	Uncorrected (Raw Data)	Accidentals	Muon Contam.	μ -Decay	Coulomb	Coul-Nucl.	Forward Scattering
141	15.7	159.4	0.1	65.7	-1.3	-2.1	- 1.7	6.1
146	15.7	174.3	0.1	68.0	-1.3	-1.9	- 1.3	6.2
157	15.7	188.5	0.2	60.7	-1.2	-1.6	- 0.2	10.1
162	15.7	191.1	0.2	52.5	-1.0	-1.5	- 0.1	11.0
175	15.7	200.2	0.2	48.6	-0.9	-1.3	1.1	11.7
179	15.7	202.2	0.2	49.8	-0.8	-1.2	1.3	12.2
191	15.7	210.1	0.4	41.4	-0.7	-1.0	2.1	9.7
194	15.7	207.2	0.4	40.2	-0.6	-1.1	2.2	8.5
202	17.1	162.4	0.5	53.4	-0.6	-1.1	1.5	7.9
209	15.7	193.2	0.5	26.5	-0.4	-0.8	2.4	8.7
213	15.7	188.5	0.5	26.7	-0.3	-0.8	2.8	5.1

TABLE XII.

Measured $\pi^{\pm}$ Cross Section Values

I. Carbon-12

Energy (MeV)	π^+ (mb)	Energy (MeV)	π^- (mb)
121	644 ± 10	97	642 ± 14
147	682 ± 10	134	692 ± 12
172	678 ± 7	142	698 ± 12
198	633 ± 7	146	696 ± 12
216	598 ± 8	171	686 ± 9
241	554 ± 8	175	676 ± 9
		204	631 ± 9
		223	599 ± 11
		227	587 ± 11

II. Beryllium-9

Energy (MeV)	π^+ (mb)	Energy (MeV)	π^- (mb)
120	512 ± 8	96	529 ± 14
146	567 ± 8	141	644 ± 9
171	570 ± 6	146	649 ± 9
198	531 ± 7	170	636 ± 7
215	500 ± 8	203	577 ± 8
240	460 ± 8	223	542 ± 10
		227	523 ± 10

III. Helium-3

Energy (MeV)	π^+ (mb)	Energy (MeV)	π^- (mb)
123	277 ± 16	141	266 ± 20
151	341 ± 14	146	234 ± 18
176	333 ± 12	157	256 ± 16
202	308 ± 12	162	252 ± 16
219	262 ± 13	175	260 ± 17
243	232 ± 15	179	263 ± 17
		191	260 ± 19
		194	257 ± 20
		202	222 ± 22
		209	229 ± 22
		213	222 ± 22

TABLE XIII.

Compilation of $\pi^{\pm}$ Carbon Total Cross Sections

Energy (MeV)	π^- Cross Section (mb)	Ref.	Energy (MeV)	π^+ Cross Section (mb)	Ref.
87	583.1 ± 15.4	a	87	501.3 ± 24.9	a
113	673.0 ± 18.7		113	624.6 ± 14.2	
127	687.6 ± 17.6		127	646.9 ± 11.6	
155	699.4 ± 9.5		155	682.7 ± 12.0	
186	661.5 ± 13.0		186	640.9 ± 10.5	
228	584.1 ± 8.5		228	569.4 ± 13.5	
258	534.9 ± 8.0		258	522.7 ± 8.0	
287	492.2 ± 6.5		287	473.7 ± 8.0	
335	421.3 ± 4.5		335	408.4 ± 4.5	
480	314.3 ± 2.5		480	304.4 ± 3.0	
565	301.2 ± 2.0		565	291.9 ± 4.5	
694	304.5 ± 4.0		694	297.7 ± 4.0	
854	326.2 ± 6.0		854	322.2 ± 6.0	
78	508.0 ± 6.0*	b	78	438.0 ± 6.0*	b
106	661.1 ± 4.0		106	593.0 ± 4.0	
141	707.5 ± 4.0		141	678.5 ± 4.0	
185	664.0 ± 4.0		185	658.0 ± 4.0	
221	600.5 ± 3.0		221	591.5 ± 3.0	
258	532.5 ± 3.0		258	523.5 ± 3.0	
151	716 ± 19.0	c	115	620.0 ± 18.0	c
90	590 ± 12.0	d	132	680.0 ± 17.0	

TABLE XIII.

Compilation of $\pi^{\pm}$ Carbon Total Cross Sections (cont'd)

Energy (MeV)	π^- Cross Section (mb)	Ref.	Energy (MeV)	π^+ Cross Section (mb)	Ref.
108	666.0 ± 10.0		155	682.0 ± 16.0	
120	681.0 ± 7.0		177	634.0 ± 17.0	
150	696.0 ± 7.0		210	601.0 ± 17.0	
180	670.0 ± 7.0				
230	584.0 ± 6.0				
260	536.0 ± 6.0				
280	510.0 ± 6.0				
69.5	537.0 ± 20.0	e			
87.5	571.0 ± 20.0				

a. B. W. Allardyce, et al. Ref. 51.

b. C. Wilkin, et al., Ref. 52.

c. N. D. Gabitzsch, et al., Ref. 53.

d. F. Binon, et al., Ref. 40.

e. R. M. Edelstein, et al., Ref. 50.

* Statistical error only

TABLE XIV.

Compilation of $\pi^{\pm}$ Beryllium Total Cross Section

Energy (MeV)	π^- Cross Section	Ref.	Energy (MeV)	π^+ Cross Section	Ref.
89	466.5 ± 11.1	a	89	421.5 ± 11.3	a
115	567.1 ± 30.2		115	491.7 ± 14.9	
128	620.6 ± 9.8		128	516.6 ± 8.0	
156	645.2 ± 9.8		156	561.9 ± 12.3	
187	610.8 ± 8.8		187	540.5 ± 8.8	
229	526.4 ± 7.2		229	469.1 ± 11.9	
259	469.5 ± 6.8		259	418.1 ± 7.3	
289	415.5 ± 6.1		289	383.4 ± 6.3	
337	343.8 ± 4.9		337	312.3 ± 5.1	
409	282.9 ± 3.4		409	267.7 ± 2.9	
482	237.1 ± 2.8		482	236.5 ± 2.6	
567	225.4 ± 3.0		567	233.2 ± 3.8	
696	232.7 ± 3.0		696	244.3 ± 3.8	
855	258.8 ± 4.0		855	268.6 ± 5.7	
107	556.0 ± 4.0*	b	107	454.0 ± 4.0*	b
142	654.0 ± 4.0		142	565.0 ± 4.0	
186	614.0 ± 3.0		186	554.0 ± 3.0	
222	542.0 ± 3.0		222	495.0 ± 3.0	
260	460.0 ± 2.0		260	422.0 ± 2.0	
151	661.0 ± 13.0	c	113	483.0 ± 10.0	c
			131	589.0 ± 11.0	
			153	581.0 ± 11.0	
			176	549.0 ± 10.0	
			209	500.0 ± 10.0	

a. B. W. Allardyce, et al., Ref. 51.

b. C. Wilkin, et al., Ref. 52.

c. N. D. Gabitzsch, et al., Ref. 53.

* Statistical error only

TABLE XV.

Compilation of $\pi^{\pm}$ Lithium-7 Total Cross Sections

Energy (MeV)	π^- Cross Section (mb)	Ref.	Energy (MeV)	π^+ Cross Section (mb)	Ref.
91	371.7 ± 19.8	a	91	312.0 ± 8.2	a
117	510.9 ± 8.6		117	384.4 ± 13.3	
130	548.9 ± 4.3		130	420.4 ± 4.6	
158	565.3 ± 10.5		158	487.3 ± 12.0	
189	528.3 ± 10.8		189	480.7 ± 8.6	
231	448.4 ± 8.0		231	394.2 ± 7.8	
261	395.9 ± 8.6		261	356.4 ± 6.6	
291	344.4 ± 5.6		291	308.6 ± 5.4	
338	277.5 ± 4.3		338	258.5 ± 4.3	
411	229.9 ± 2.6		411	212.0 ± 2.5	
483	190.3 ± 2.6		483	191.8 ± 2.3	
568	181.3 ± 2.3		568	194.3 ± 3.3	
698	189.2 ± 2.9		698	199.3 ± 3.9	
857	210.6 ± 4.0		857	227.7 ± 5.0	
110	484.0 ± 4.0*	b	110	387.0 ± 4.0*	b
145	575.0 ± 4.0		145	483.0 ± 4.0	
188	547.0 ± 4.0		188	467.0 ± 4.0	
225	467.0 ± 3.0		225	426.0 ± 3.0	
262	393.0 ± 3.0		262	358.0 ± 3.0	

a. B. W. Allardyce, et al., Ref. 51.

b. C. W. Wilkin, et al., Ref. 52.

* Statistical error only

TABLE XVI.

Coulomb Distortion Corrections. All Corrections are in Millibarns.

Energy (MeV)	^{3}He $\Delta\sigma = (\sigma^- - \sigma^+)$	^{3}He -Coul.	^{7}Li $\Delta\sigma = (\sigma^- - \sigma^+)$	^{7}Li -Coul.	^{9}Be $\Delta\sigma = (\sigma^- - \sigma^+)$	^{9}Be -Coul.
80	- 35.4	7.8	45.5	17.7	47.8	26.7
100	- 53.7	7.4	81.5	16.9	78.3	25.5
120	- 76.3	7.2	117.0	15.9	83.2	23.1
140	-105.8	7.0	105.0	14.7	79.5	21.4
160	- 90.5	6.7	82.7	13.4	77.2	19.2
180	- 70.2	6.1	66.4	12.0	66.3	17.1
200	- 65.7	5.4	60.4	10.7	64.2	15.2
300			29.9	6.2	30.9	9.0
400			13.8	4.1	17.6	6.1
500			- 0.1	3.2	0.9	4.7
600			- 9.9	2.7	- 1.5	3.9
700			- 11.7	2.4	- 9.7	3.5
800			- 10.7	2.2	-10.0	3.1

X. FIGURES

Figure 1. Experimental counter arrangement.

Figure 2. Block diagram of logic circuitry. The units labeled D are standard discriminators and those labeled C are coincidence units.

Figure 3-A. Schematic of time of flight system with logic circuitry.

Figure 3-B. Schematic of Cerenkov chamber with logic circuitry.

Figure 4. Plan view of meson area at SREL (Beam I).

Figure 5. Plan view of pion channel for the PTA (Beam II).

Figure 6. Cryogenic system for liquid ^{3}He target.

Figure 7. Liquid Helium-3 target section and thermal radiation shielding.

Figure 8. Gas handling system.

Figure 9-A. Range telescope.

Figure 9-B,C. Differential range curves for π^+ and π^- beams.

Figure 10-A,B. Time of flight spectra taken in Beam I. The first Gaussian corresponds to π^- present in the incident beam and the second Gaussian corresponds to the μ^- present.

Figure 11-A,B,C. Cerenkov spectra taken in Beam II for incident π^+ beam. Least square fit shows curves for interacting pions in liquid radiator (FC75) and Gaussian peak for

pions not interacting in chamber. Second Gaussian represents muons present in the incident beam.

Figure 12. Cerenkov spectrum taken in Beam II for incident π^- beam. Third Gaussian represents electron in incident beam.

Figure 13-A,B,C. Measured differential cross section for Carbon, Beryllium, and Helium-3 at one of the incident energies. The solid line represents the computer fit to the differential cross section using an exponential in $|t|$, the momentum transfer. Vertical error bars are statistical and horizontal error bars represent angular acceptance of counter.

Figure 14-A,B. Plot of the π^+ and π^--Carbon cross sections. The darker figures are the π^+ measurements.

Figure 15-A,B. Plot of the π^+ and π^- Beryllium cross sections. The darker figures are the π^+ measurements. The smooth curves in Figure 15-A are the cross sectional curves used in evaluating the sum rule.

Figure 16. Plot of the π^+ and π^- Helium-3 cross sections. The darker figures are the π^+ measurements. The smooth curves are the cross sectional curves used in evaluating the sum rule and dispersion relation.

Figure 17. Plot of $K(0; \pi p \rightarrow)/K(0; \pi N_1 N_2)$ verus ξ, the mean correction factor.

INCIDENT PION - $\bar{A}_1 S_1 S_2 \bar{A}_2 S_3 S_4$

TRANSMITTED PION - (INCIDENT PION) T_i

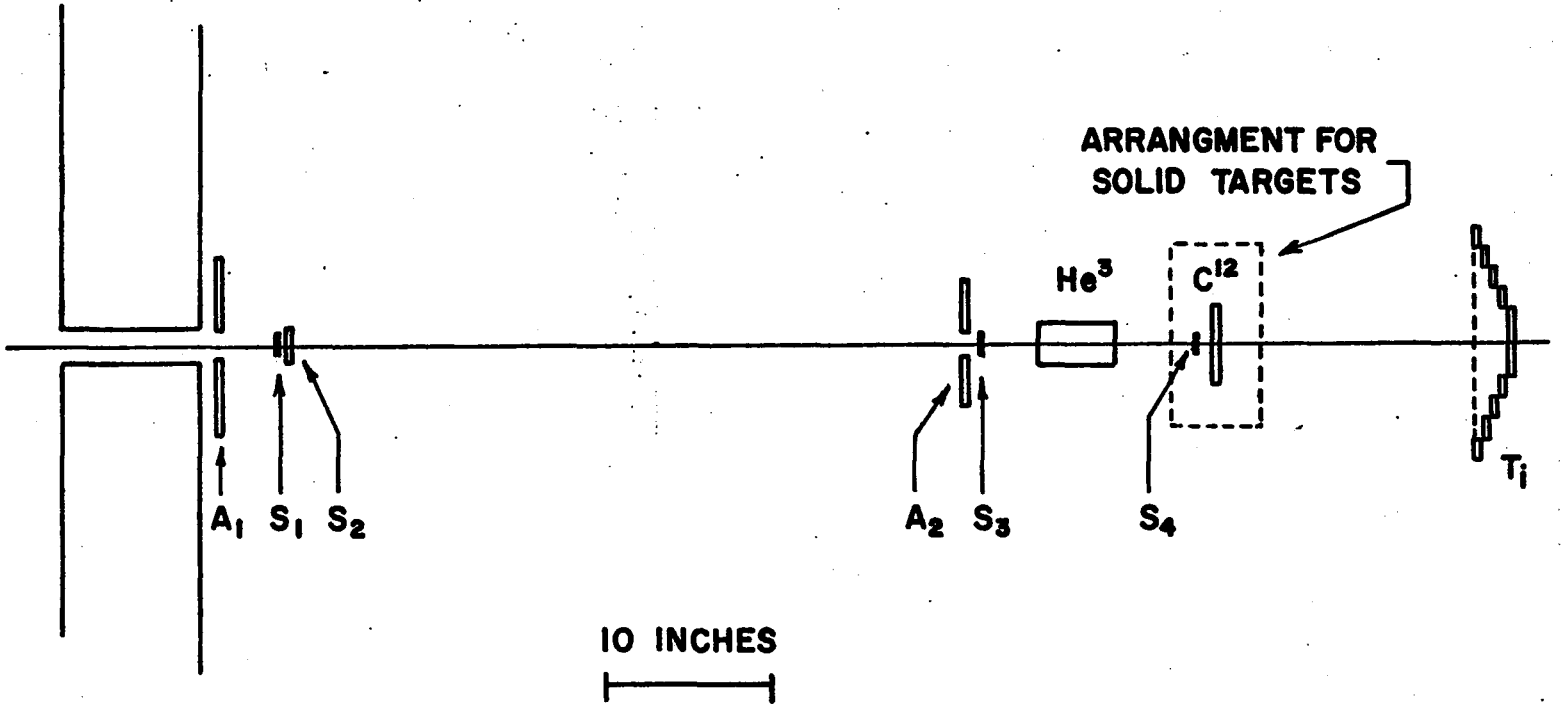

FIG. 1

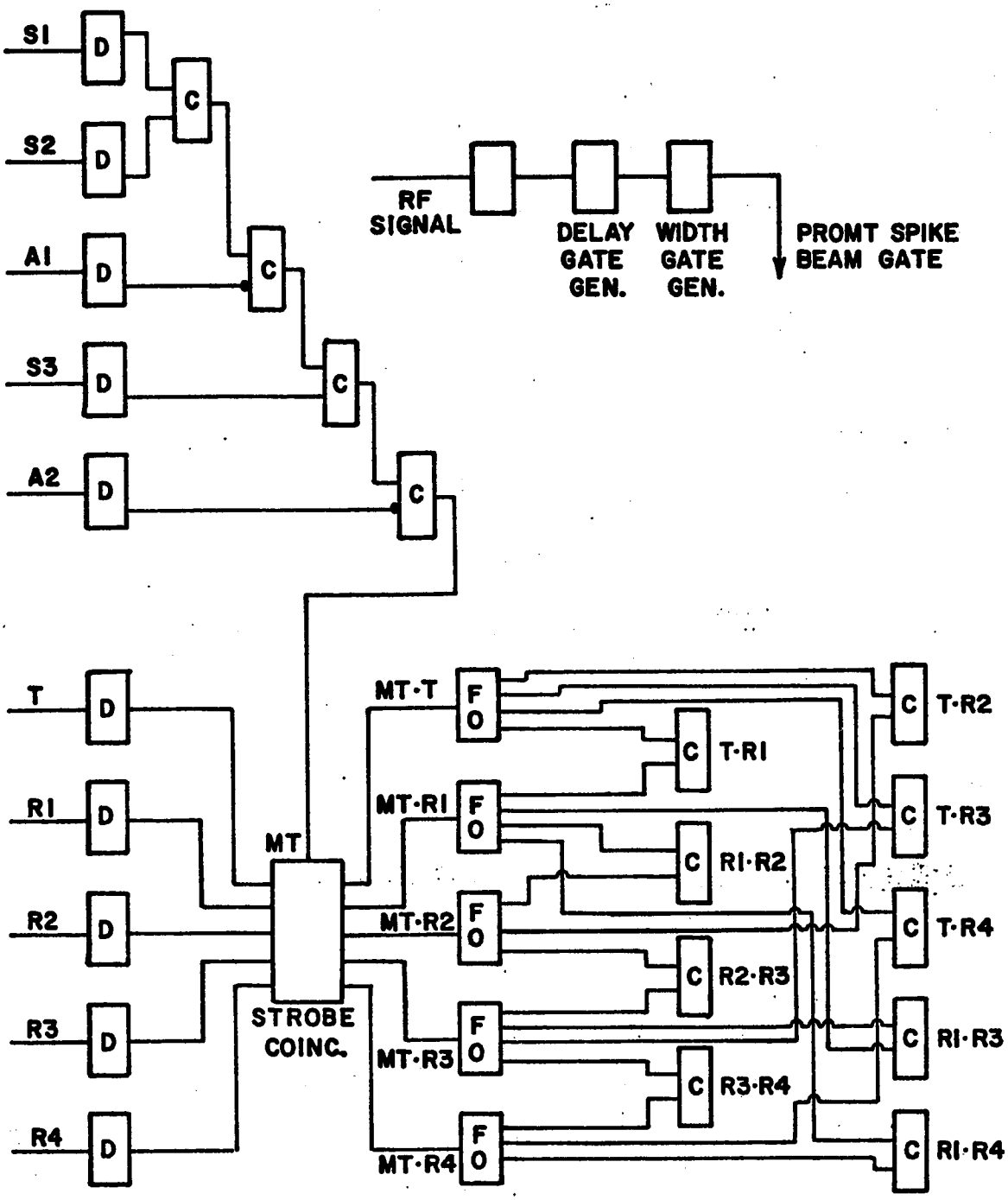
S1
S2
A1
S3
A2
T
R1
R2
R3
R4
D
C
MT
STROBE COINC.
RF SIGNAL
DELAY GATE GEN.
WIDTH GATE GEN.
PROMT SPIKE BEAM GATE
MT·T
MT·R1
MT·R2
MT·R3
MT·R4
F O
T·R1
T·R2
T·R3
T·R4
R1·R2
R2·R3
R3·R4
R1·R3
R1·R4

FIG. 2

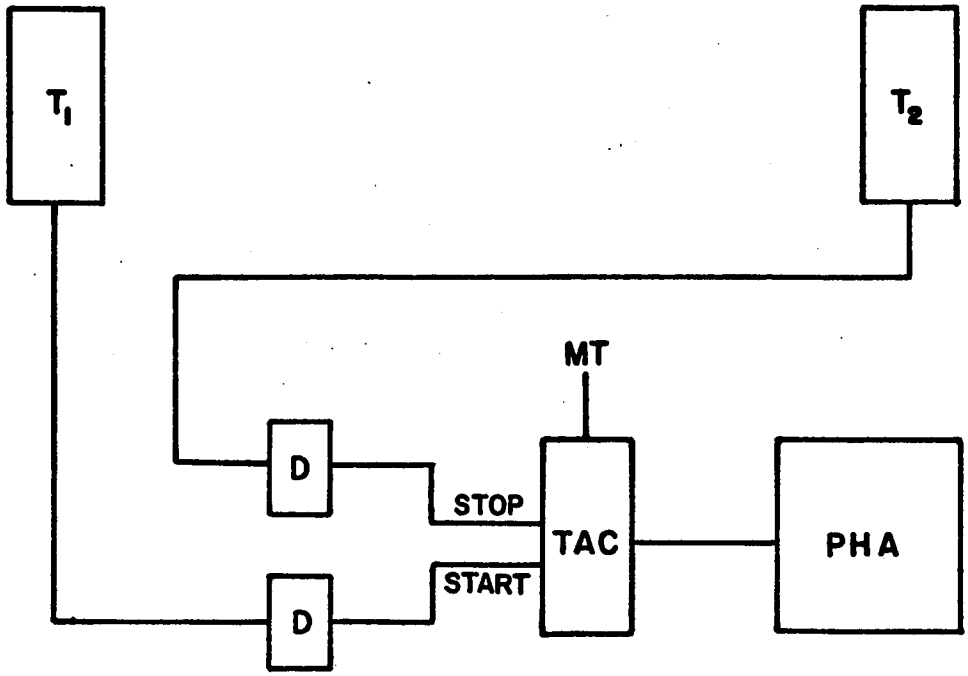
T1
T2
MT
D
STOP
TAC
PHA
START
D

FIG. 3—A

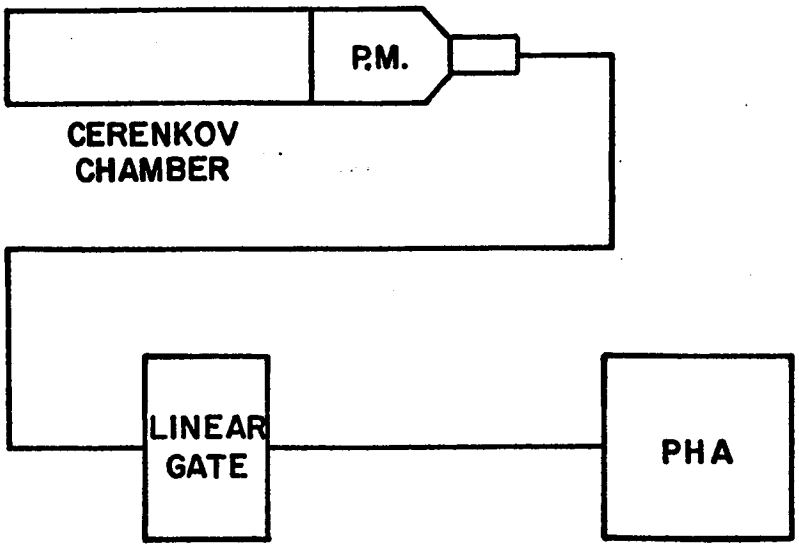
P.M.
CERENKOV
CHAMBER
LINEAR
GATE
PHA

FIG. 3—B

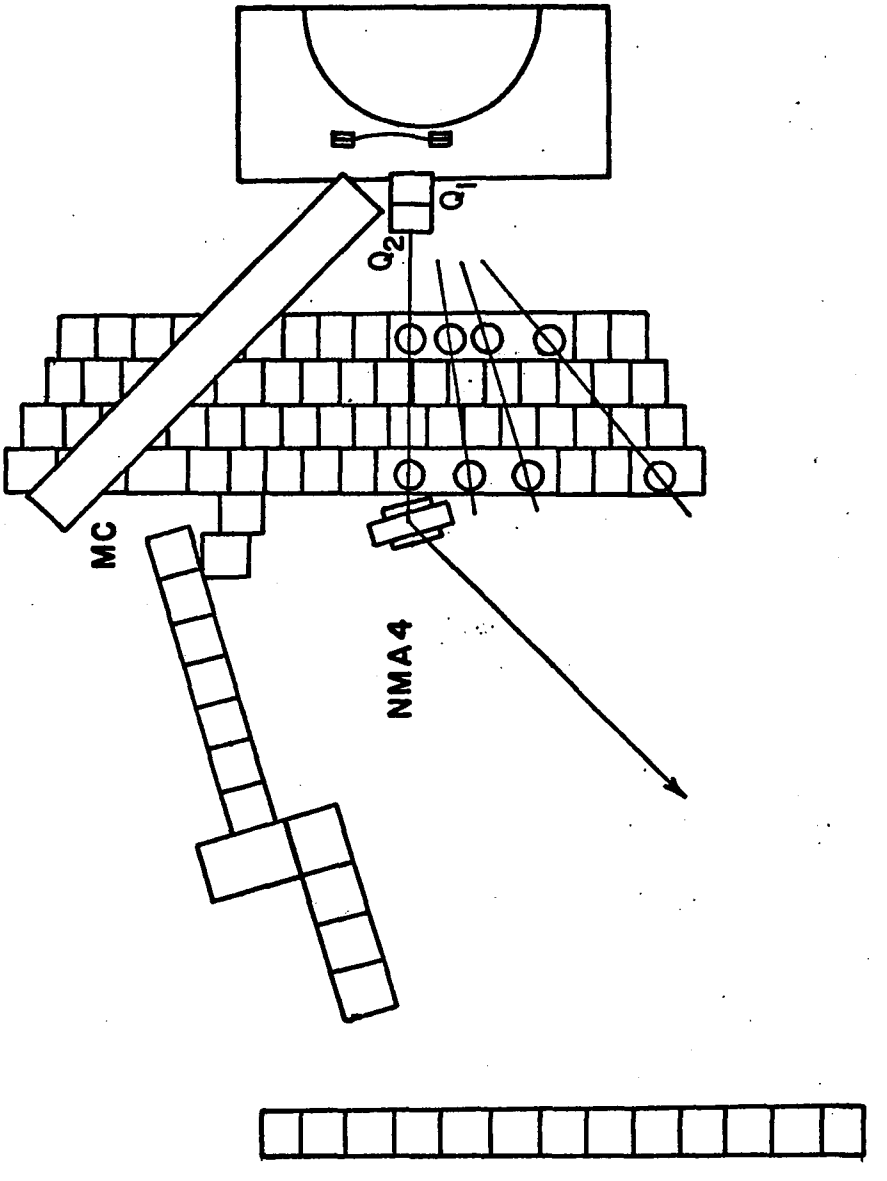

FIG. 4

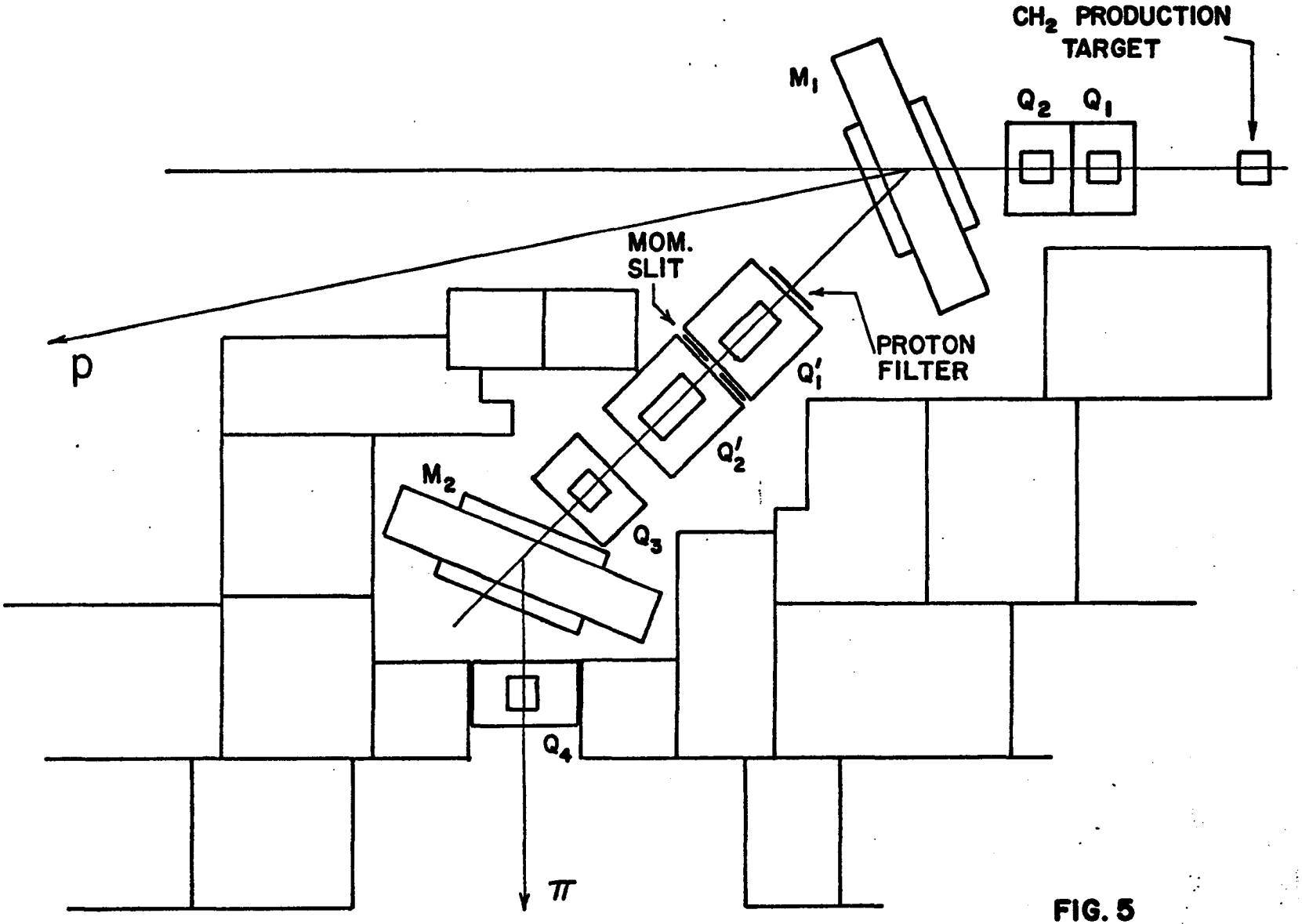
CH2 PRODUCTION
TARGET
M1
Q2
Q1
MOM.
SLIT
PROTON
FILTER
p
Q'1
Q'2
M2
Q3
Q4
π

FIG. 5

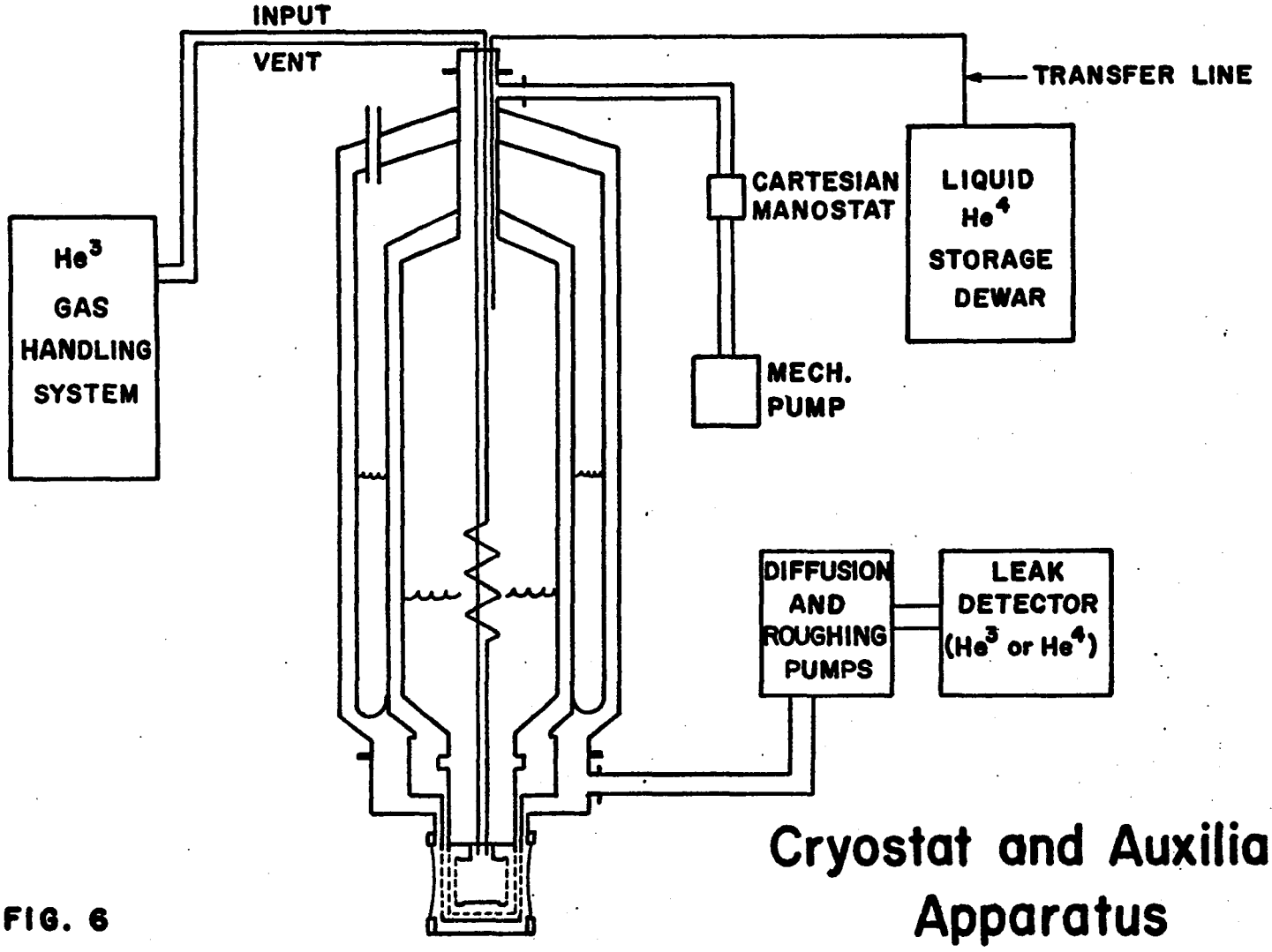

FIG. 6

Cryostat and Auxiliary Apparatus

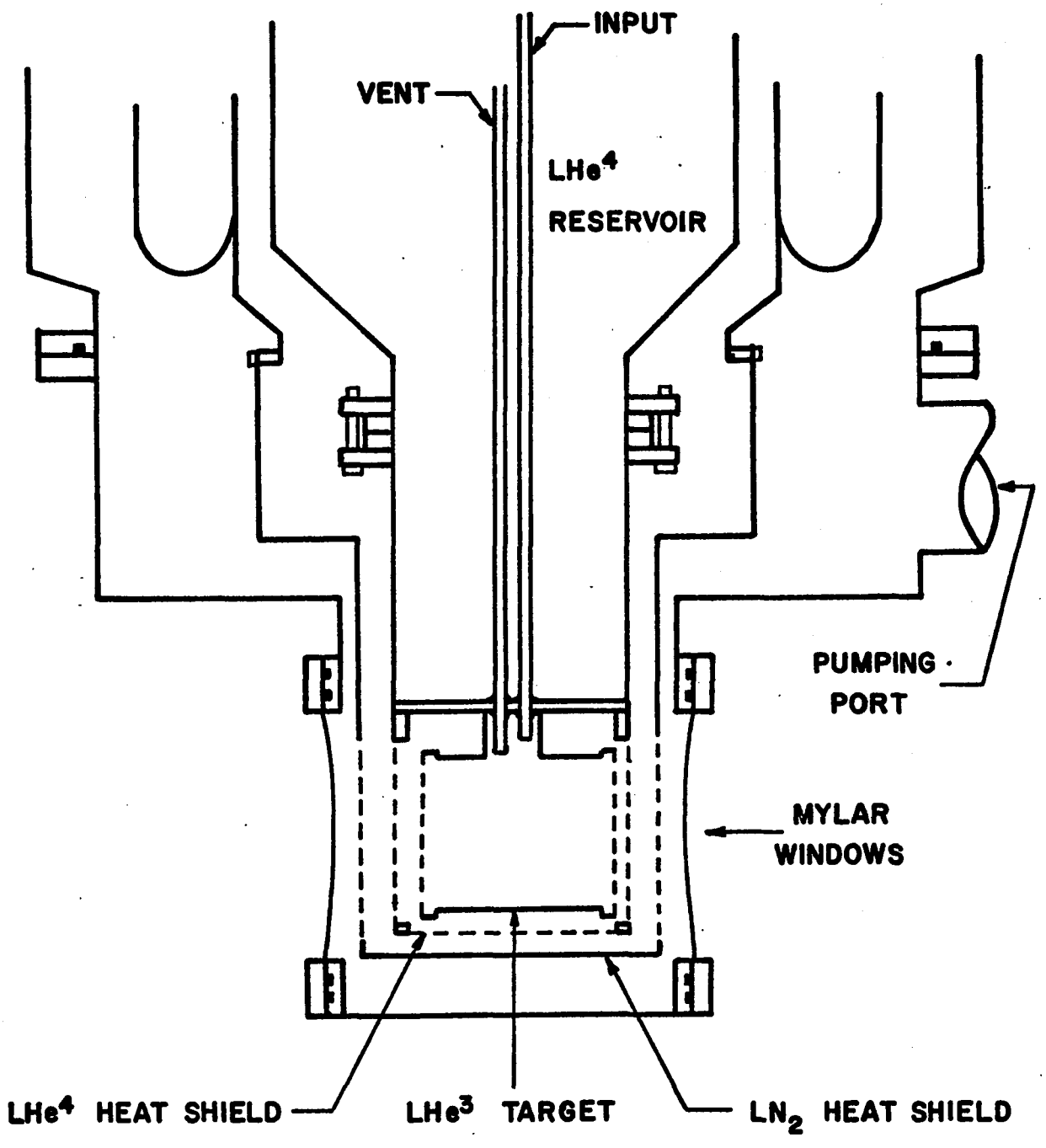
INPUT
VENT
LHe4
RESERVOIR
PUMPING
PORT
MYLAR
WINDOWS
LHe4 HEAT SHIELD
LHe3 TARGET
LN2 HEAT SHIELD

FIG. 7

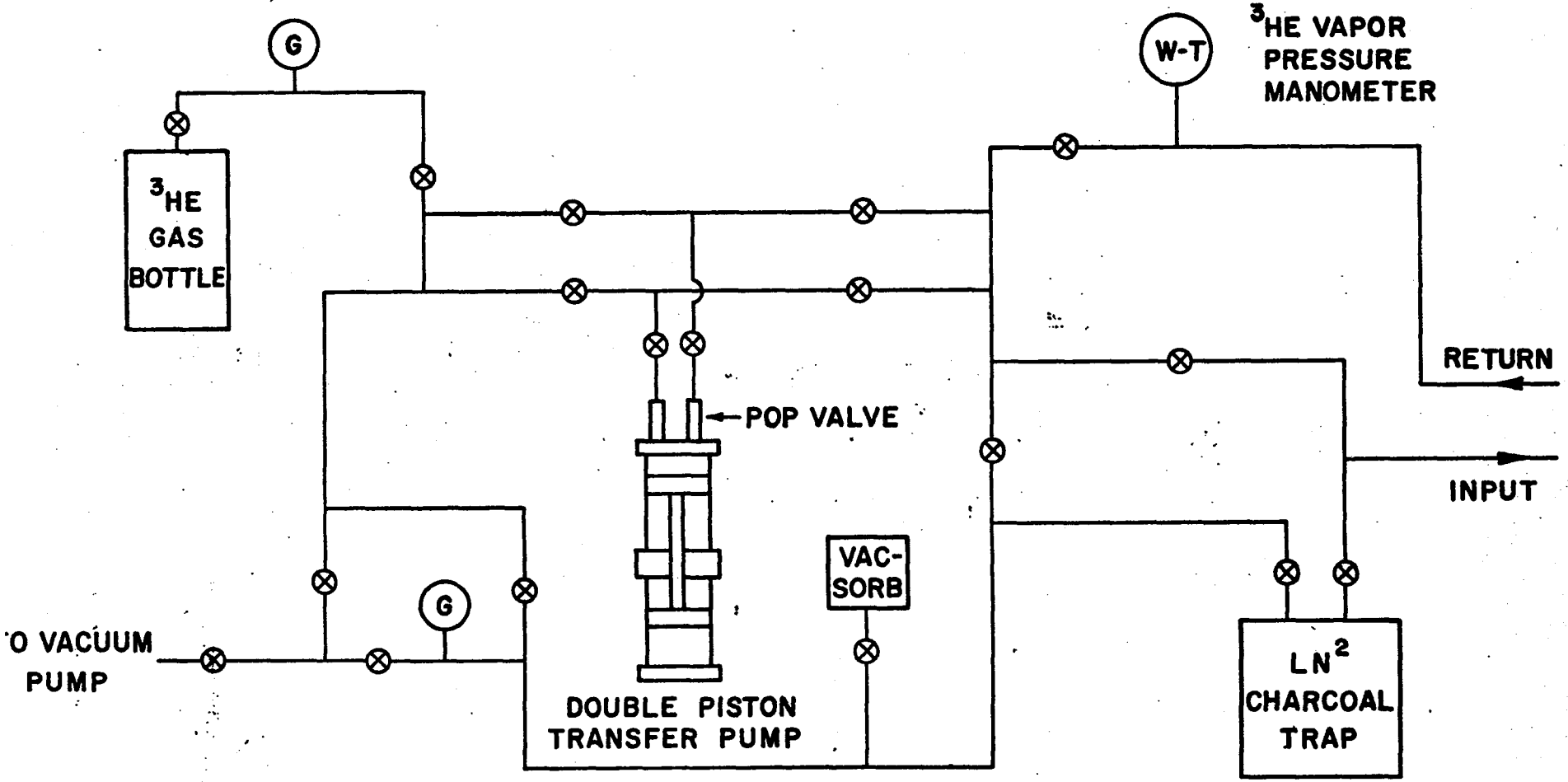
G
^{3}HE GAS BOTTLE
W-T
^{3}HE VAPOR PRESSURE MANOMETER
RETURN
INPUT
POP VALVE
VAC-SORB
G
O VACUUM PUMP
DOUBLE PISTON TRANSFER PUMP
LN^2 CHARCOAL TRAP

FIG. 8

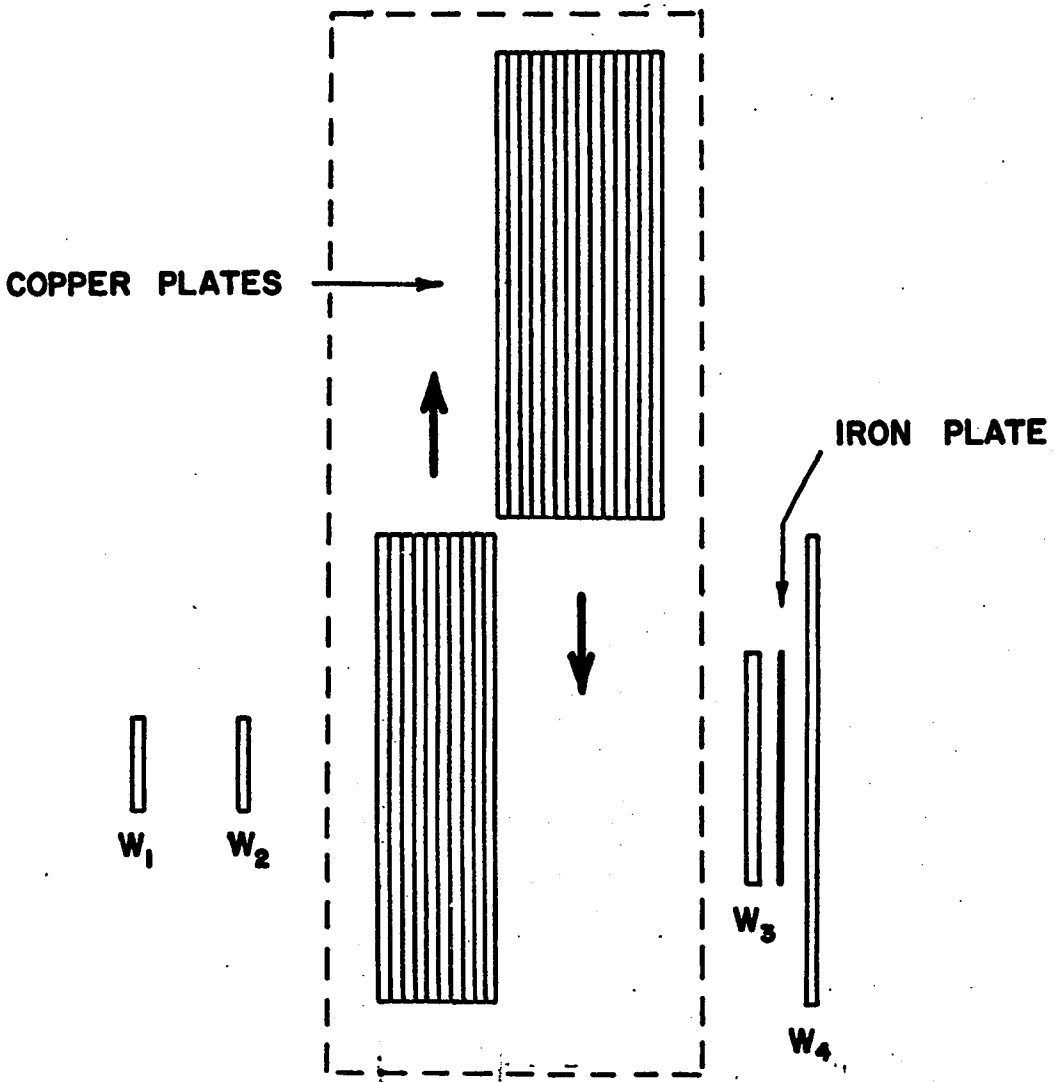

FIG. 9-A

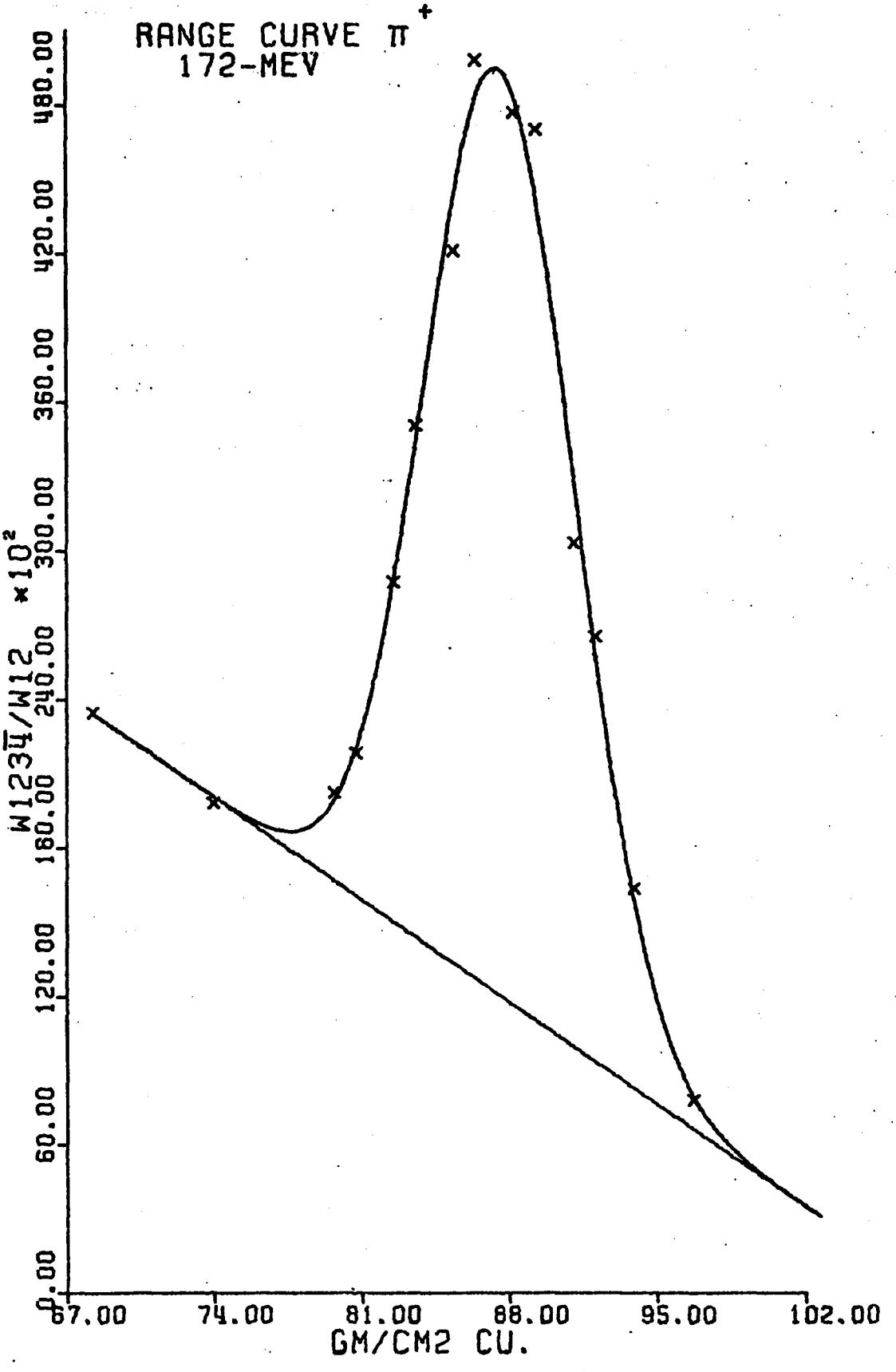
RANGE CURVE π+
172-MEV
W1234/W12 ×10²
0.00
60.00
120.00
180.00
240.00
300.00
360.00
420.00
480.00
67.00
74.00
81.00
88.00
95.00
102.00
GM/CM2 CU.

FIG. 9-B

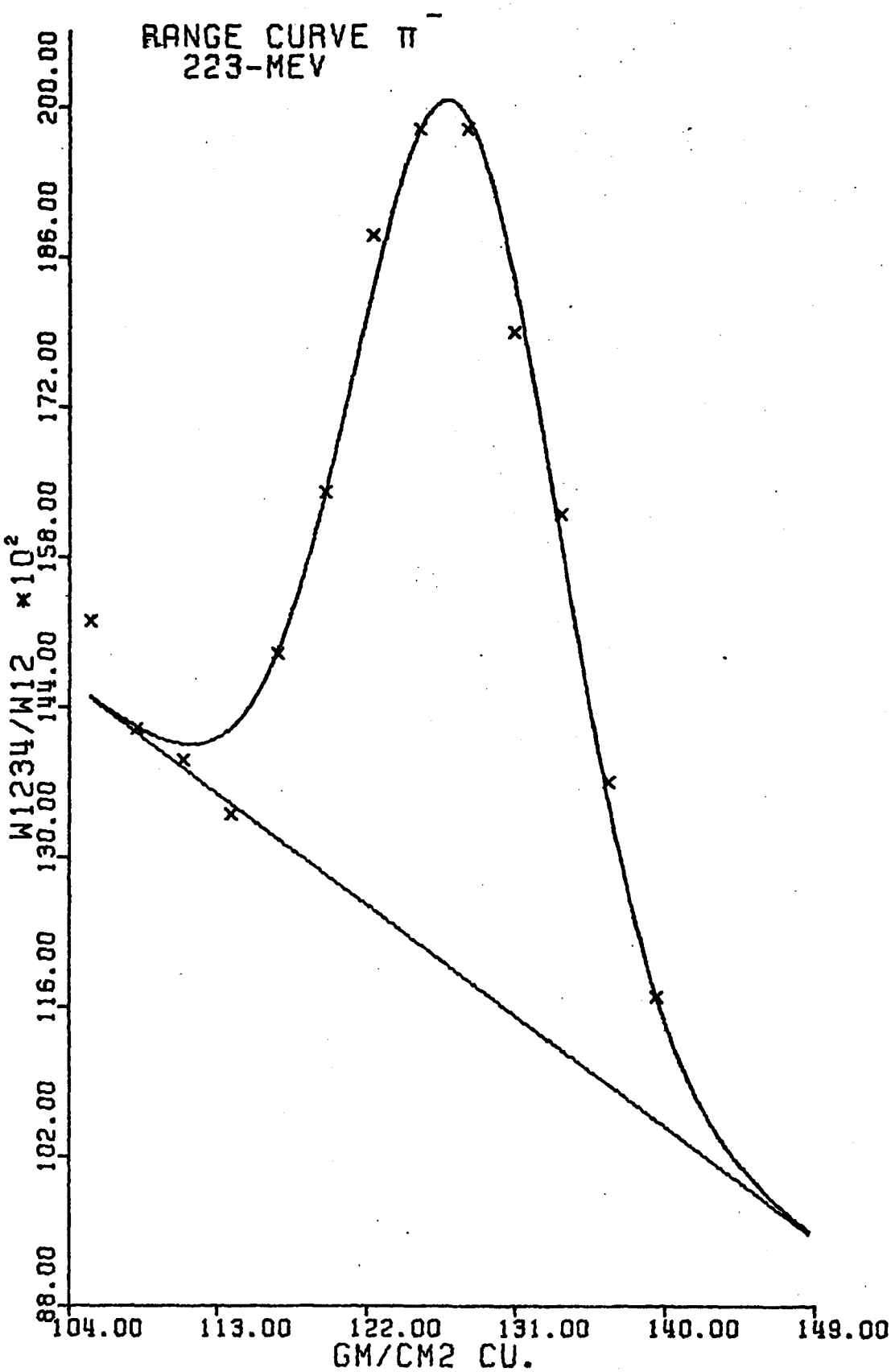
RANGE CURVE π⁻
223-MEV
W1234/W12 *10²
200.00
186.00
172.00
158.00
144.00
130.00
116.00
102.00
88.00
104.00
113.00
122.00
131.00
140.00
149.00
GM/CM2 CU.

FIG. 9-C

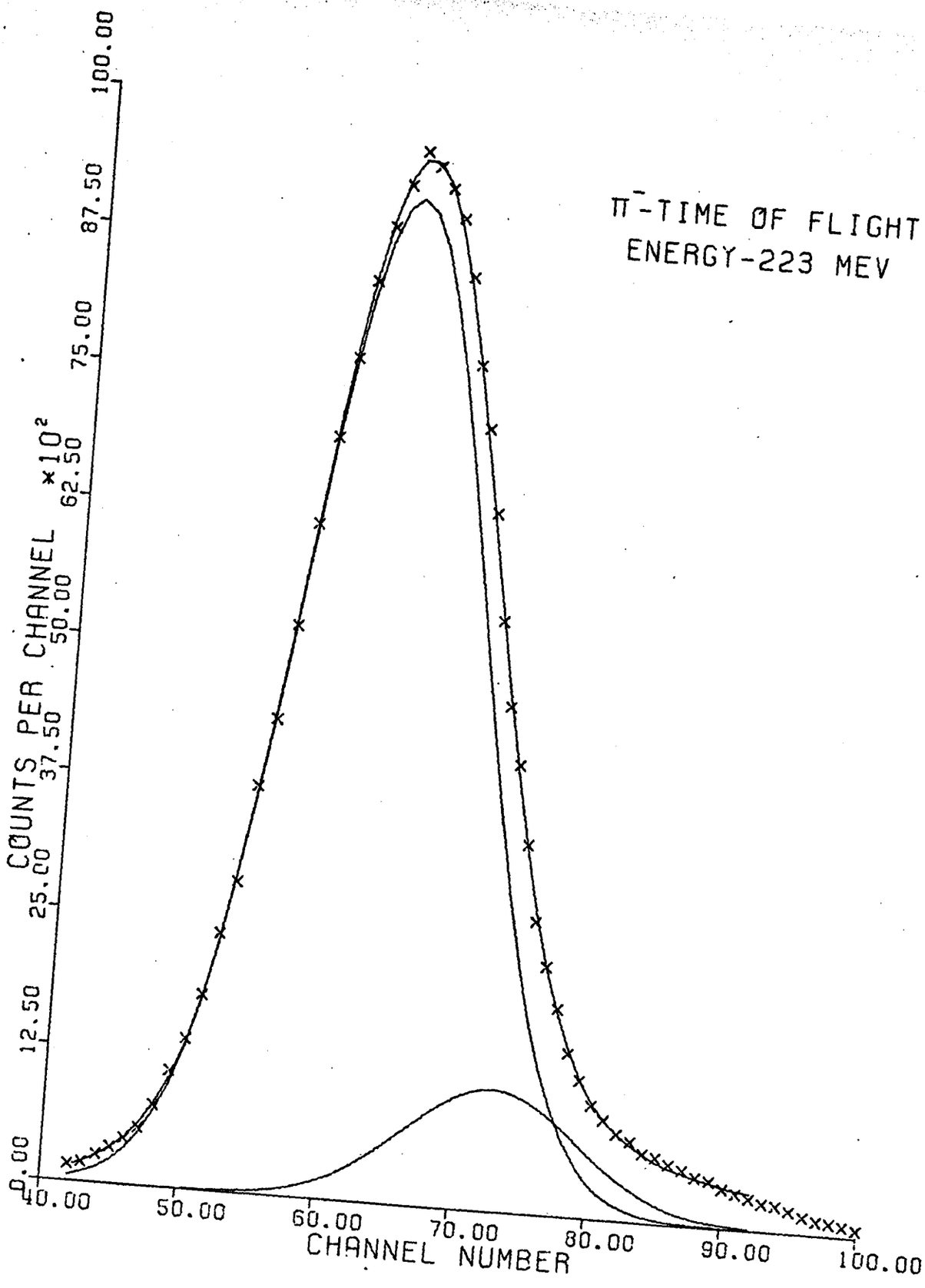
π⁻-TIME OF FLIGHT
ENERGY-223 MEV
COUNTS PER CHANNEL *10²
0.00
12.50
25.00
37.50
50.00
62.50
75.00
87.50
100.00
40.00
50.00
60.00
70.00
80.00
90.00
100.00
CHANNEL NUMBER

FIG. 10-A

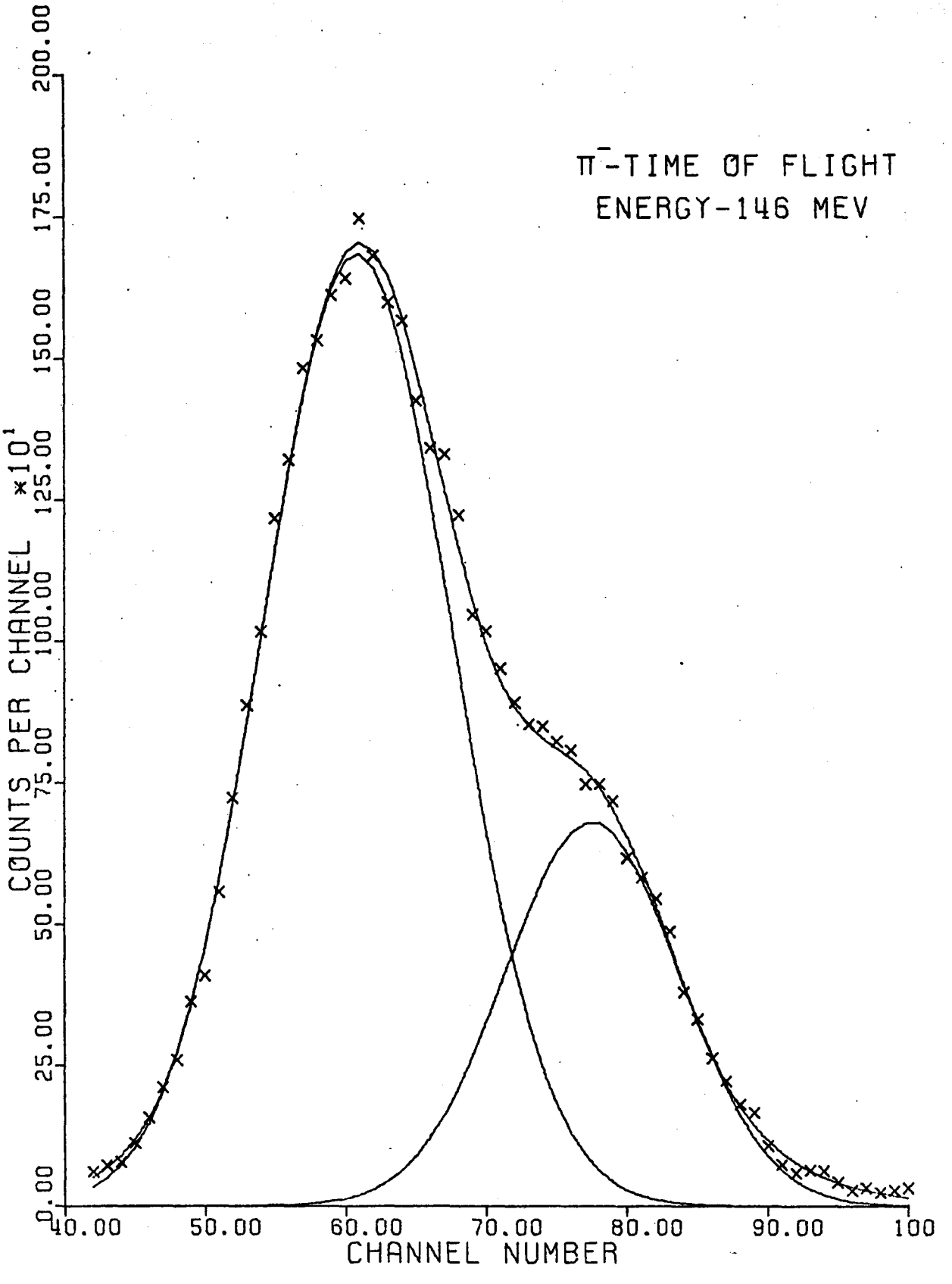
π⁻-TIME OF FLIGHT
ENERGY-146 MEV
COUNTS PER CHANNEL *10¹
0.00
25.00
50.00
75.00
100.00
125.00
150.00
175.00
200.00
40.00
50.00
60.00
70.00
80.00
90.00
100
CHANNEL NUMBER

FIG. 10-B

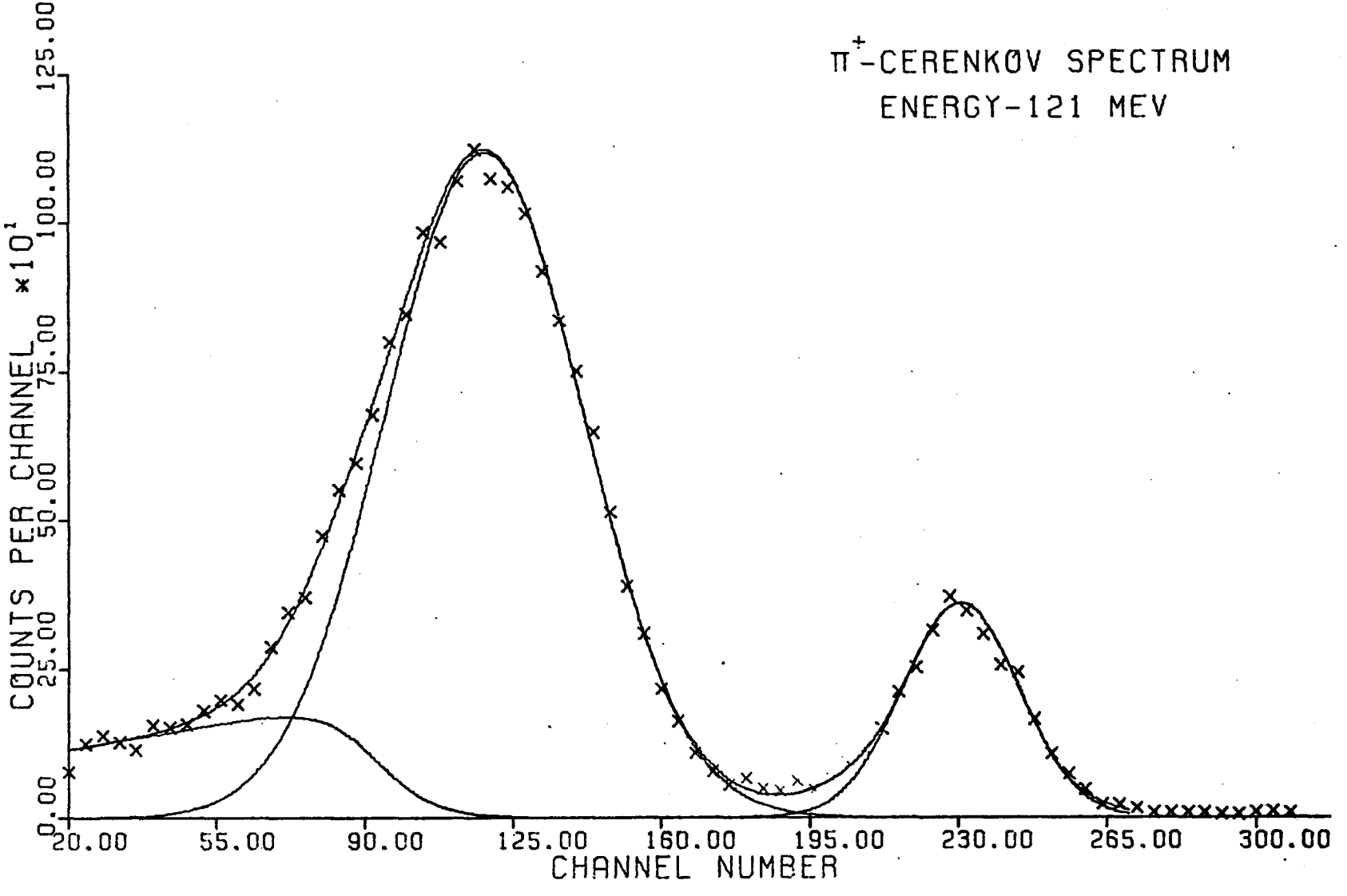
π+-CERENKØV SPECTRUM
ENERGY-121 MEV
COUNTS PER CHANNEL ×10¹
0.00
25.00
50.00
75.00
100.00
125.00
20.00
55.00
90.00
125.00
160.00
195.00
230.00
265.00
300.00
CHANNEL NUMBER

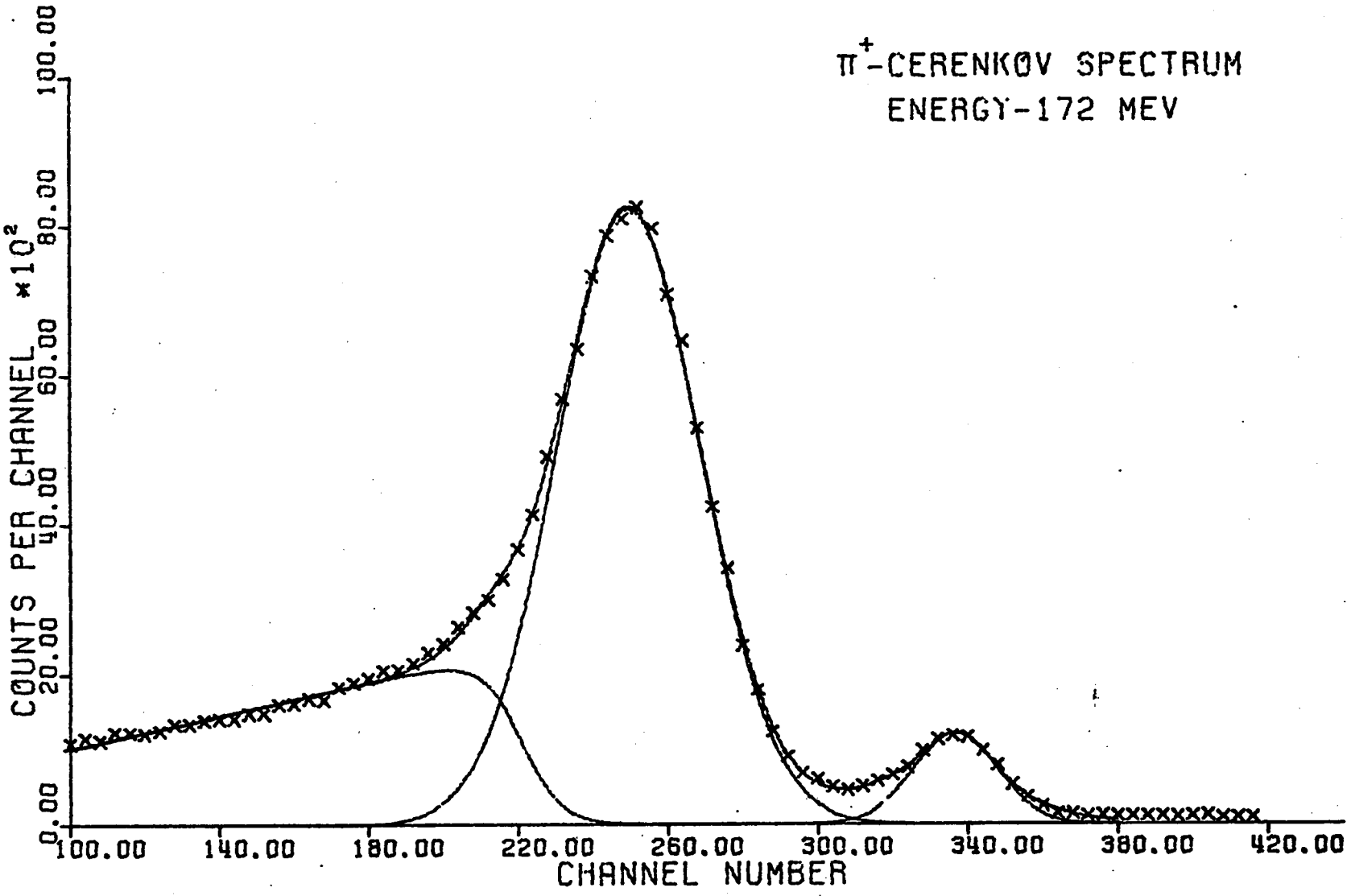
π^+-CERENKØV SPECTRUM
ENERGY-172 MEV
COUNTS PER CHANNEL *10²
0.00
20.00
40.00
60.00
80.00
100.00
100.00
140.00
180.00
220.00
260.00
300.00
340.00
380.00
420.00
CHANNEL NUMBER

FIG. 11-B

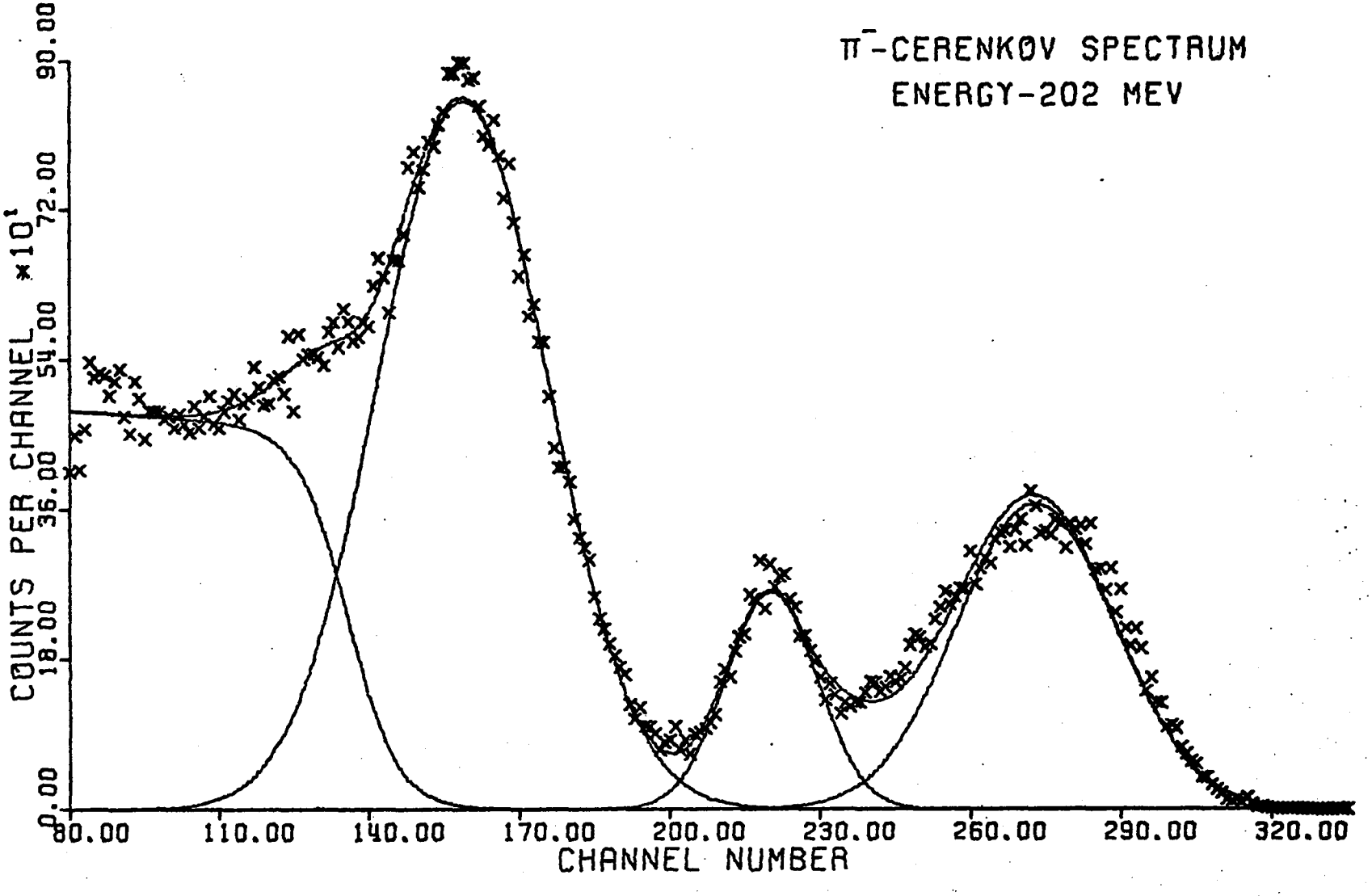
π⁻-CERENKOV SPECTRUM
ENERGY-202 MEV
COUNTS PER CHANNEL *10¹
0.00
18.00
36.00
54.00
72.00
90.00
80.00
110.00
140.00
170.00
200.00
230.00
260.00
290.00
320.00
CHANNEL NUMBER

FIG. 12

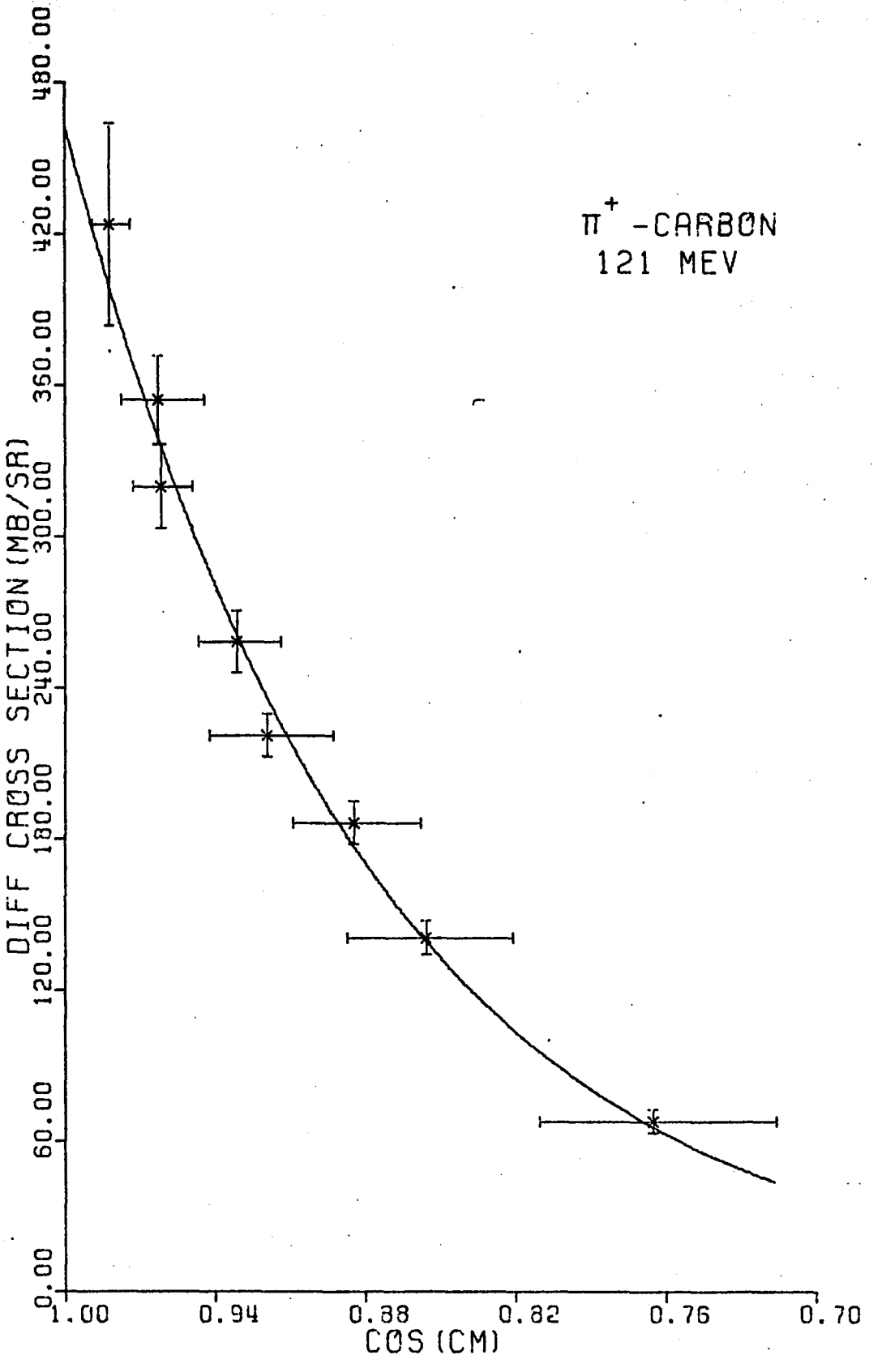
π+ -CARBON
121 MEV
DIFF CROSS SECTION (MB/SR)
480.00
420.00
360.00
300.00
240.00
180.00
120.00
60.00
0.00
1.00
0.94
0.88
0.82
0.76
0.70
COS (CM)

FIG. 13-A

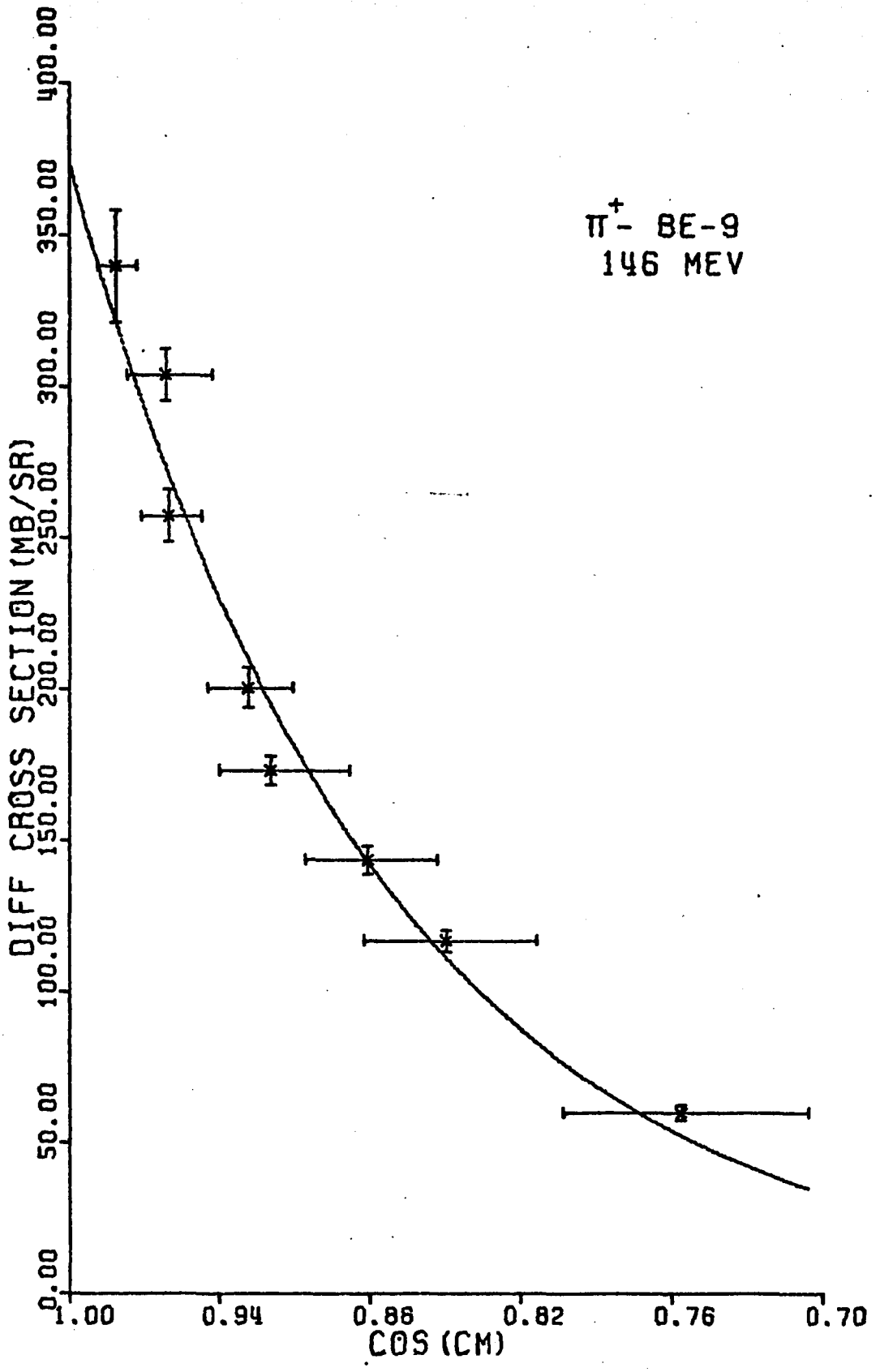
π^+- BE-9
146 MEV
DIFF CROSS SECTION (MB/SR)
0.00
50.00
100.00
150.00
200.00
250.00
300.00
350.00
400.00
1.00
0.94
0.88
0.82
0.76
0.70
COS (CM)

FIG. 13-B

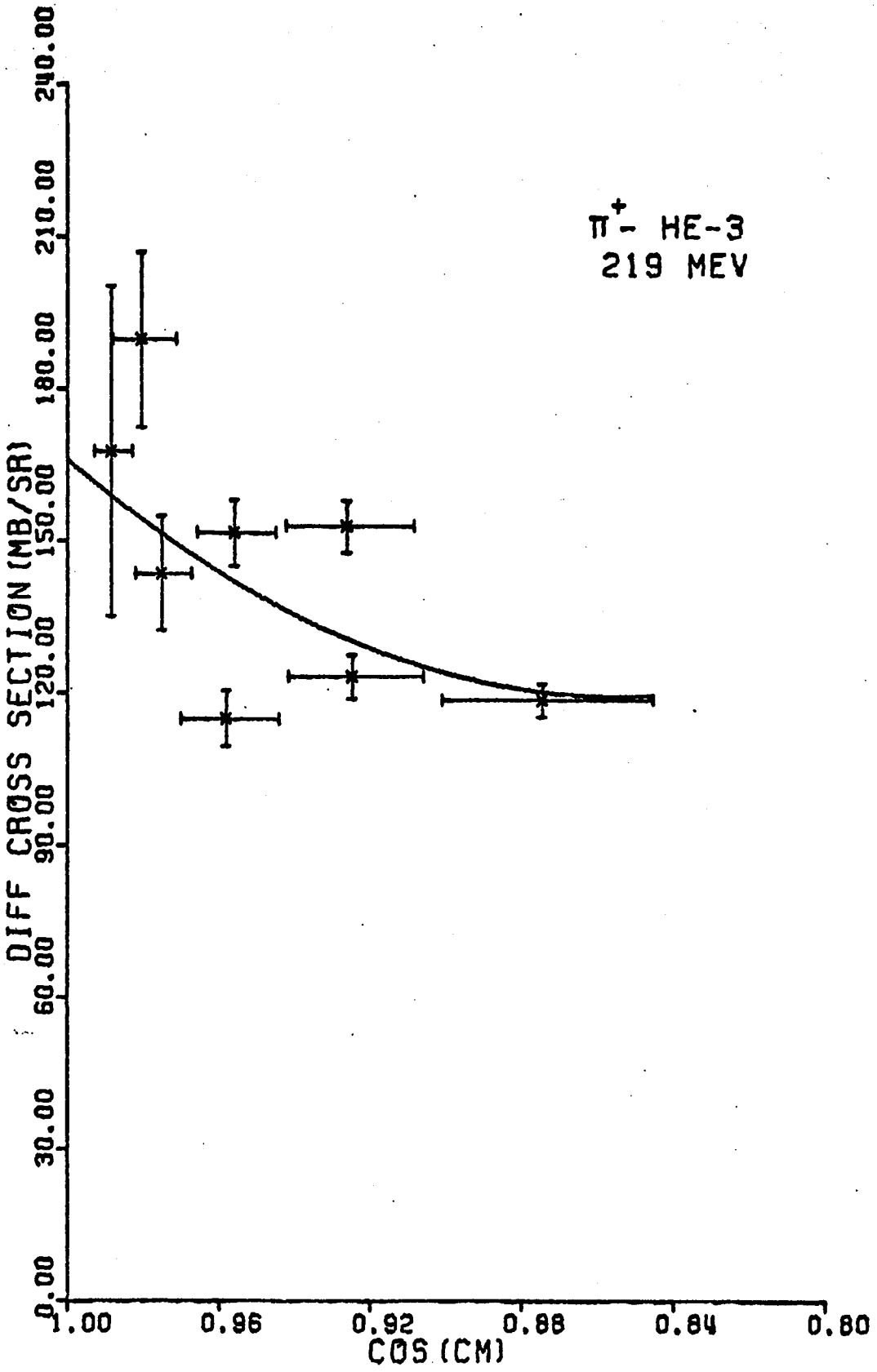
π^+- HE-3
219 MEV
DIFF CROSS SECTION (MB/SR)
240.00
210.00
180.00
150.00
120.00
90.00
60.00
30.00
0.00
1.00
0.96
0.92
0.88
0.84
0.80
COS (CM)

FIG. 13-C

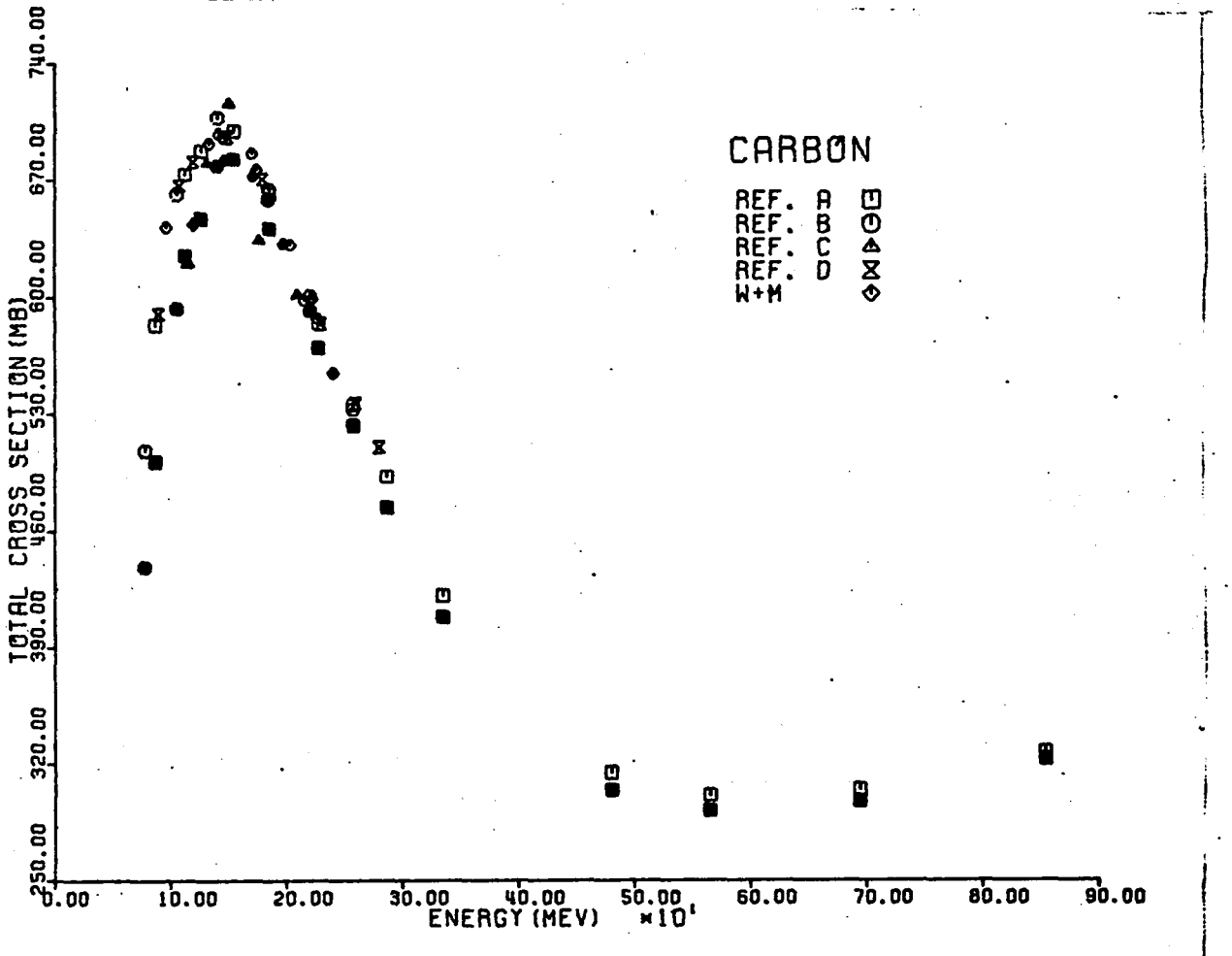
CARBON
REF. A
REF. B
REF. C
REF. D
W+M
TOTAL CROSS SECTION (MB)
250.00
320.00
390.00
460.00
530.00
600.00
670.00
740.00
0.00
10.00
20.00
30.00
40.00
50.00
60.00
70.00
80.00
90.00
ENERGY (MEV) ×10¹

FIG. 14-A

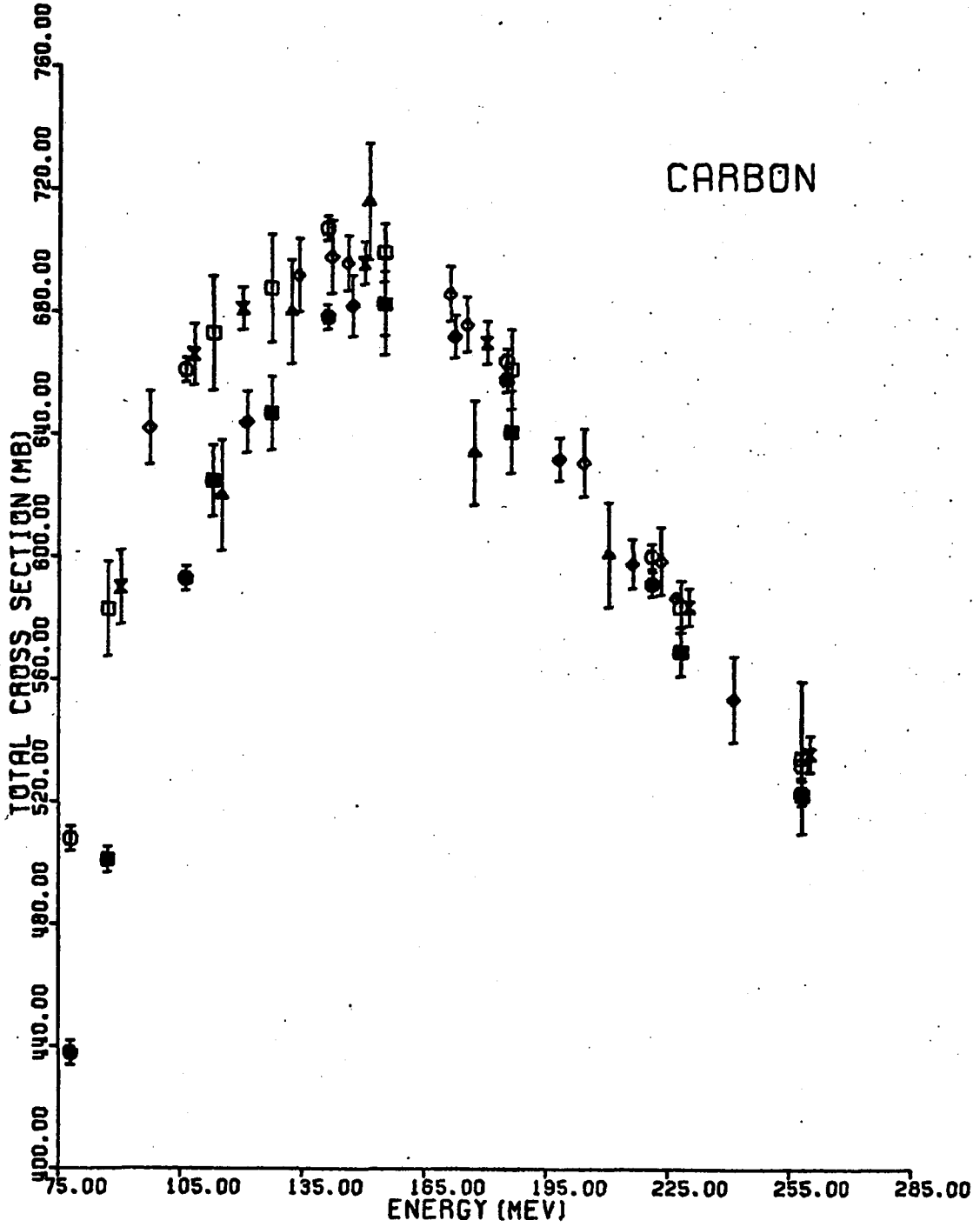
CARBON
TOTAL CROSS SECTION (MB)
400.00
440.00
480.00
520.00
560.00
600.00
640.00
680.00
720.00
760.00
75.00
105.00
135.00
165.00
195.00
225.00
255.00
285.00
ENERGY (MEV)

FIG. 14-B

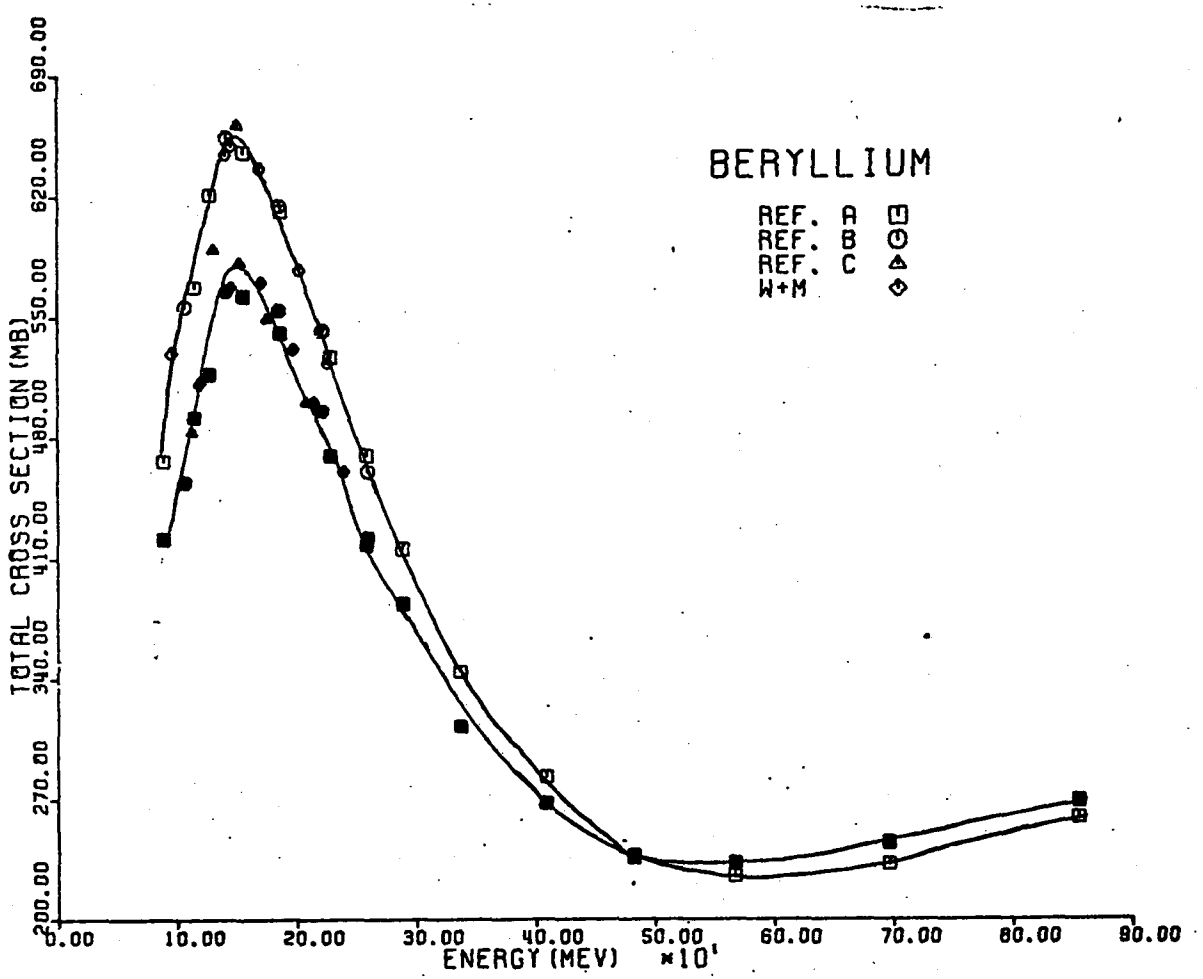
BERYLLIUM
REF. A
REF. B
REF. C
W+M
TOTAL CROSS SECTION (MB)
690.00
620.00
550.00
480.00
410.00
340.00
270.00
200.00
0.00
10.00
20.00
30.00
40.00
50.00
60.00
70.00
80.00
90.00
ENERGY (MEV) ×10¹

FIG. 15-A

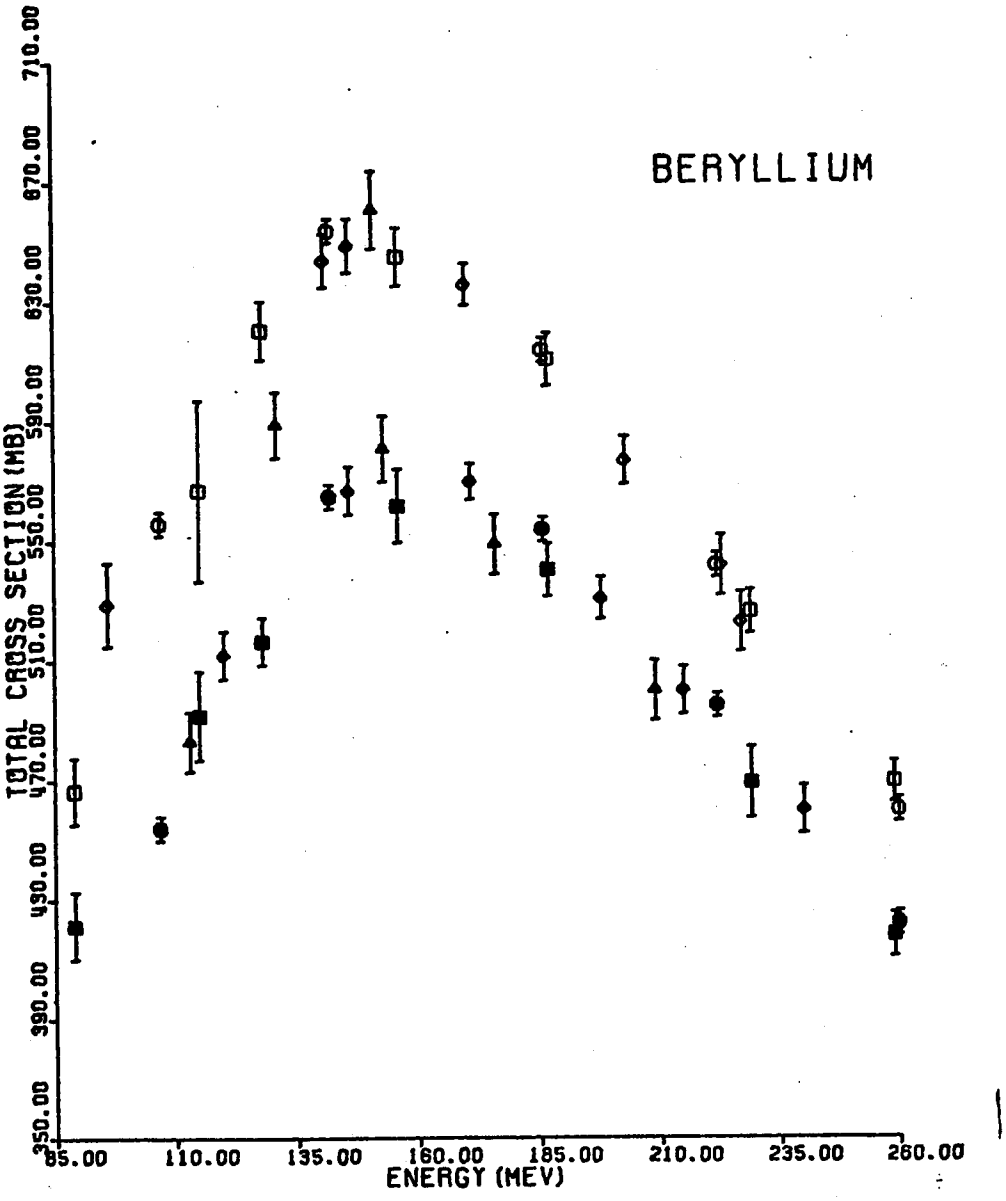
BERYLLIUM
TOTAL CROSS SECTION (MB)
350.00
390.00
430.00
470.00
510.00
550.00
590.00
630.00
670.00
710.00
85.00
110.00
135.00
160.00
185.00
210.00
235.00
260.00
ENERGY (MEV)

FIG. 15-B

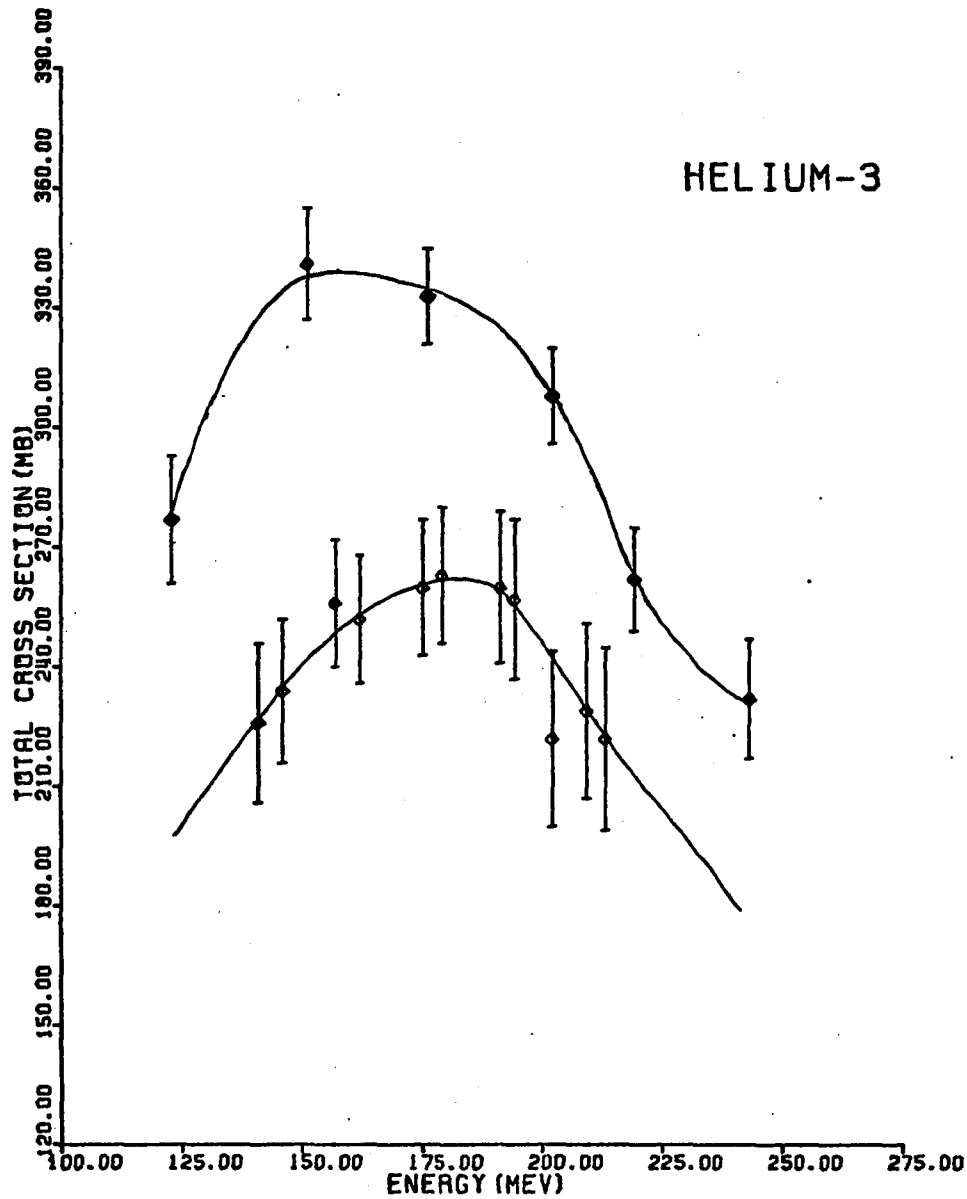
HELIUM-3
TOTAL CROSS SECTION (MB)
120.00
150.00
180.00
210.00
240.00
270.00
300.00
330.00
360.00
390.00
100.00
125.00
150.00
175.00
200.00
225.00
250.00
275.00
ENERGY (MEV)

FIG. 16

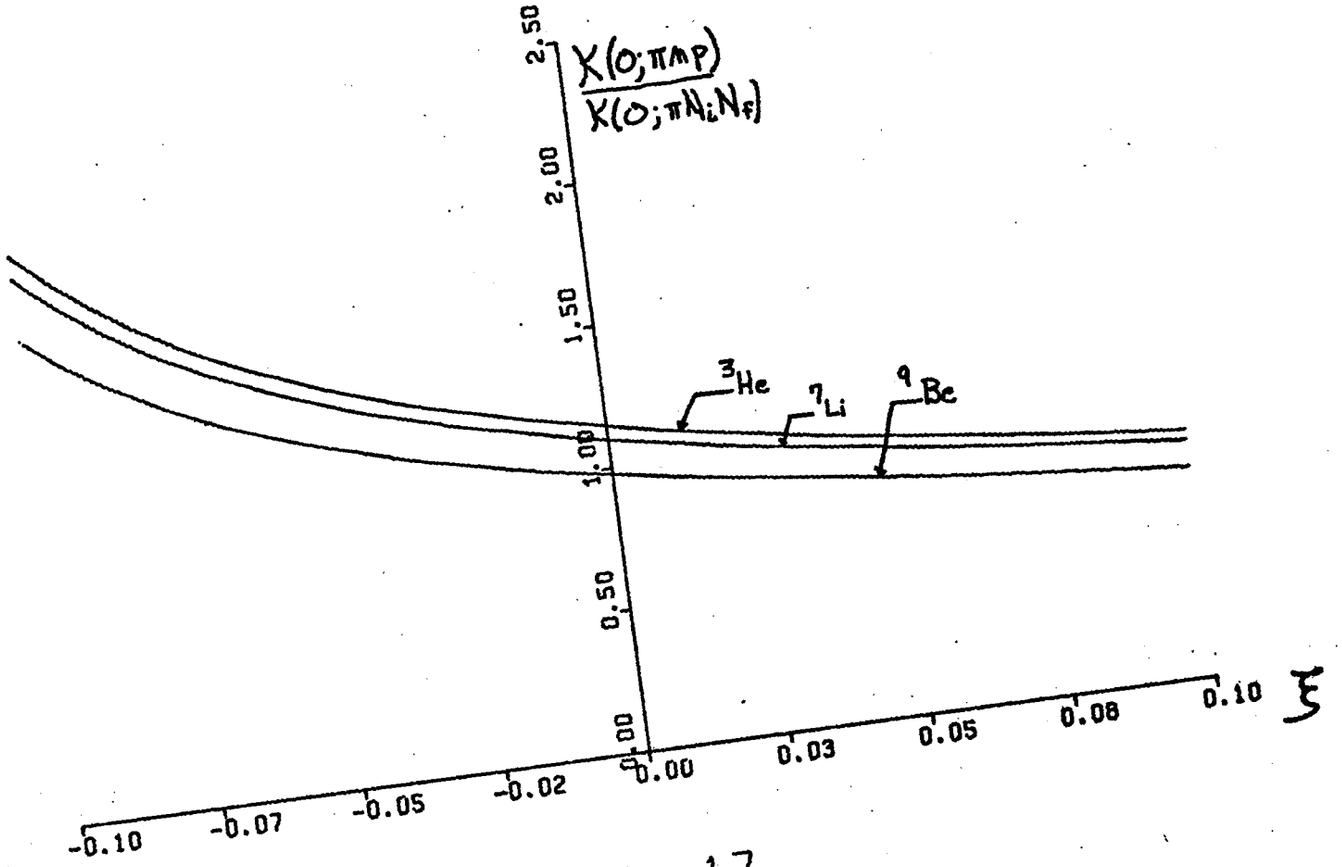
$\frac{K(0;\pi M P)}{K(0;\pi N_i N_f)}$
2.50
2.00
1.50
1.00
0.50
0.00
^{3}He
^{7}Li
^{9}Be
-0.10
-0.07
-0.05
-0.02
0.00
0.03
0.05
0.08
0.10
ξ

FIG. 17